DOCTORAATSPROEFSCHRIFT

2010 | School voor Levenswetenschappen

Applying high resolution MRI to study the rodent CNS under physiological, pathological and experimental conditions

Proefschrift voorgelegd tot het behalen van de graad van
Doctor in de Biomedische Wetenschappen, te verdedigen door:

Evi THEUNISSEN

Promotoren: prof. dr. Peter Adriaensens
prof. dr. Sven Hendrix
Copromotoren: prof. dr. Emile Beuls
prof. dr. Ivo Lambrichts

Maastricht University

universiteit
▶▶hasselt

Table of content

IV

List of figures and tables

List of abbreviations

7-AAD:	7-aminoactinomyocin
AL:	anterior lobe
BBB:	Basso, Beattie, Bresnahan
BOLD:	blood oxygen level dependent
BW:	bandwidth
CNS:	central nervous system
CT:	computer tomography
CZS:	centraal zenuwstelsel
dpi:	days post immunization
dpo:	days post operation
DWI:	diffusion weighted imaging
EAE:	experimental autoimmune encephalomyelitis
eGFP:	enhanced green fluorescence protein
FDA:	food and drug administration
FOV:	field of view
fMRI:	functional magnetic resonance imaging
g:	gram
Gd:	gadolinium
GE:	gradient echo
IC:	intracisternal
IL:	intermediate lobe
IR:	inversion recovery
iv:	intravenous
L:	litre
LFB:	luxol fast blue
Luc:	luciferase
MHC:	major histocompatibility complex
min:	minutes
mm:	millimeter
MRI:	magnetic resonance imaging

MRSI:	magnetic resonance spectroscopic imaging
ms:	millisecond
MSCs:	mesenchymal stem cells
MW:	molecular weight
NA:	number of averages
NMR:	nuclear magnetic resonance
Nf:	number of frequency encoding points
Np:	number of phase encoding points
PBS:	phosphate buffered saline
PD:	proton density
PET:	positron emission tomography
PFA:	paraformaldehyde
PG:	pituitary gland
PI:	propidium iodide
PL:	posterior lobe
PLL:	poly-L-lysine
PT:	pars tuberlaris
RF:	radio frequency
s:	second
SC:	spinal cord
SCI:	spinal cord injury
SE:	spin echo
SPIO:	small particle of iron oxide
SNR:	signal to noise ratio
T:	Tesla
TE:	echo time
TEM:	transmission electron microscopy
TI:	inversion time
TM:	trichrome von Masson
TR:	repetition time
USPIO:	ultrasmall particle of iron oxide

Chapter 1

General introduction

Outline chapter 1

1.1   Introduction

1.2   Scope of the thesis

1.1 Introduction

Magnetic resonance imaging (MRI) is one of the most important inventions in medical imaging from the twentieth century. This imaging technique has evolved from nuclear magnetic resonance spectroscopy (NMR). It was Paul Lauterbur, in the early 1970s, who introduced gradients in the magnetic field which allow to determine the spatial origin of the emitted signals from the nuclei of the studied object. This spatial information makes it possible to produce two- and three-dimensional images (Lauterbur, 1973).

The first commercial MR scanner in Europe was installed in 1983 and ever since MRI has been used in millions of examinations. MRI offers superior resolution and tissue contrast compared to PET and CT-scanners respectively (Acton and Kung, 2003; Colby and Morenko, 2004). The technique is gaining more and more applications in the clinic nowadays because this imaging modality offers the opportunity to look inside the human body without any form of surgery. It is a non-invasive and risk-free method for the visualisation of soft tissues in different anatomical planes. However, MR imaging is not recommended for patients having medical metal devices (surgery clips, stents, pacemakers, permanent make-up ..) because of safety issues and metal susceptibility artefacts in the image. MR image quality can also be disturbed by chemical shift artefacts (due to the different resonance frequency of water and fat) or by air-tissue boundaries (susceptibility artifact) **(Table 1.1)**.

 MRI is often used as a diagnostic or monitoring tool to visualize morphological alterations in organs due to disease, but also changes in signal intensities can be indicative for ongoing pathological conditions as for instance in multiple sclerosis (Hoey et al., 2009; Rovira and Leon, 2008; Serkova et al., 2009; Traboulsee and Li, 2008). This ability to distinguish diseased from healthy tissue is possible because of many imaging sequences which can be used to obtain optimal contrast. The basic contrast methods are T1-, T2- and proton density (PD) weighted MRI. Although these contrast methods provide a good overall contrast, it remains sometimes difficult to distinguish anatomical structures based on endogenous tissue contrast differences. In such cases the use of contrast agents

can offer specific tissue enhancement after administration, resulting in an increased contrast differences between anatomical structures. These substances are known to shorten the relaxation decay times what results in hyper- or hypo-intensity on T1- or T2-weighted images respectively (Lin et al., 2008; Runge, 2008). Gadolinium, iron oxide and manganese containing contrast agents are applied in the clinic to improve the visibility of blood vessels (MR angiography), tumors or lesions of the liver, inflammation of the central nervous system and many more applications.

When looking at disease, MR applications remained not limited to conventional MR images but also new techniques such as functional MR (fMRI), diffusion MRI (DWI) or single voxel spectroscopy (MRSI) were introduced within a short time frame to study the inside human body (Bammer et al., 2005). These advanced MR techniques provide an additional broad spectrum of information about the investigated tissue. fMRI is used to visualize neuronal activity without exogenous contrast agents. As neuronal activity increases, the demand for oxygen also increases which results in increasing the amount of oxygenated hemoglobin relative to deoxygenated hemoglobin. This is called the BOLD (Blood-oxygen-level dependent) effect. Because deoxygenated hemoglobin attenuates the MR signal, the vascular reactions leads to a signal increase that is related to the neural activity. DWI informs about the diffusion of water molecules at a specific location in the tissue. It is known that the more restriction occurs due to biological barriers, the more hyper-intense the signal on the DWI image will be. This technique is often used to detect cellular oedema. MRSI on the other hand is applied to determine the levels of different metabolites in body tissues or fluids. Metabolic disorders or tumor activity can be analyzed from the resulting spectrum (Soares and Law, 2009).

Whereas MRI, in its early days, was primarily used for imaging in routine clinical diagnosis, its role in biomedical research has expanded over the past 15 years (Hu and Norris, 2004). MR images can be obtained from *in vitro* tissue specimens as well as from living animals. The applications of MRI using small animals in studies of human diseases have been increasing since the 1980s

(Hansen et al., 1980). The majority of experiments make use of rodents because they are easy to keep and breed, share basic biology and chemistry with humans, and the broad availability of genetically engineered strains. The use of clinical scanners with small rodents suffers from low signal-to-noise ratio (SNR) what reduces image quality. Most clinical scanners operate at low field strengths between 1.0 and 3 Tesla (T) which makes it difficult to interpret and detect morphological and signal abnormalities in small rodents (Brockmann et al., 2007; Pentney et al., 1993). Therefore it is better to use high field strength, small bore scanners (4.7 – 11.7 T) because they provide high resolution images (up to 20 - 30 µm) with high SNR. However, relatively long scan time (hours) is required to obtain such high resolution MR images **(Table 1.1)**. With regard to this, (*in vivo)* MR image quality is always a compromise between scan time (SNR) and resolution.

High resolution MRI has the capacity to depict the anatomical structures of small rodents in sufficient detail (Benveniste and Blackband, 2002; Pirko et al., 2005). As previously mentioned for clinical applications, biomedical research MRI of animals will primarily focus on detecting morphological deviations and disease related changes in signal intensity compared to normal healthy animals. Commonly known contrast agents, as used in the clinic, are also applicable in small rodent biomedical research. Besides these conventional contrast enhancement techniques, it has become even possible to perform MR imaging at cellular nano-scale (Budde and Frank, 2009). In cellular MR imaging, cells are labeled with contrast particles and can be visualized as they migrate throughout the tissues. It offers the opportunity to unravel cell mediated disease mechanisms as demonstrated for the tempero-spatial kinetics of immune cells in an animal model of multiple sclerosis (Baeten et al., 2008). Although MRI is able to detect clusters of contrast labeled cells, the technique is still not sensitive enough to visualize contrast labeled single cells **(Table 1.1)**. In addition, attention should be paid to the issue of selectivity and specificity of contrast enhanced signals on MR images, i.e. the possibility of uptake of contrast particles by other phagocytic cells after cell death of the contrast labeled cells.

As outlined above, it is clear that clinical and high resolution small animal MRI have become a popular tool to study a wide range of biomedical research questions. MRI shows more than a static picture alone. It provides physiologic and metabolic data as well as information about dynamic processes which all lead to a better understanding of human diseases and should result in the development of new diagnostic and treatment approaches.

Magnetic resonance imaging	
Main advantages	**Main disadvantages**
No harmful radiation	Low sensitivity
High resolution	Attention for artefacts
Good soft tissue contrast	Long scan times
Variety of contrast modalities	No medical (metal) devices

Table 1.1: Overview of general advantages and disadvantages of MRI.

1.2 Scope of this thesis

Since 1990, a strong expertise was built up in the Chemistry division of the Institute of Material Science (IMO) of the UHasselt regarding high field MRI in order to study specific properties of polymer materials. It paved the way to apply and evaluate MRI as a complementary tool in the field of biomedical research and more specific in the study owith focus on CNS related diseases.

At present, there is a growing implementation of MR imaging in experimental small animal studies regarding neurological diseases since MR imaging provides excellent soft tissue contrast for the CNS. Therefore it is desired to have a set of reference MR images of the anatomical CNS structures of interest before screening or analyzing diseased animals. Such a reference frame allows to determine the normal morphometric parameters of anatomical structures, such as distance, height, width, area and even volume, but also to show the expected

signal intensities for different weighting sequences. Starting from a proper reference atlas, one can start applying MRI to detect disease related abnormalities with or without the additional use of contrast agents. Up till now, there are detailed histological atlases of the rodent CNS, but there is a need for high resolution MRI atlases which show high quality MR images of the normal rodent CNS.

This work aimed to meet this need for a reference set of high resolution MR-based images of the rodent CNS. As described in detail in chapter 3, the reference set of images was *ex vivo* obtained from formalin fixed and freshly isolated brain and spinal cord specimens in different slice directions and with several weighting sequences (PD- and T2-weighted). Further on in this thesis, this MR image reference set was applied to analyze MR signal intensities retrieved from pathological and experimental conditions.

In chapter 2, a brief explanation about the basic principles of MRI is given. The MRI pulse sequences which are mainly used in this work are defined as well as the use of contrast particles to label cells. Advantages and disadvantages of using small animal high resolution imaging are also described.

In chapter 4, a detailed MRI reference frame for the pituitary gland of the rat is shown. This small structure is investigated to critically evaluate the boundaries of the high resolution MR imaging technique with respect to the anatomical detail differentiation. The pituitary gland is a complex anatomical structure with small dimensions requiring good contrast differences and SNR to visualize the separate parts of the gland. Susceptibility differences between the bones of the sella turcica and the pituitary gland tissue might cause artefacts that interfere with the high image quality one is aiming for. Determining local relaxation values (T1, T2 and M_0) for the three lobes of the pituitary gland will lead to pulse sequence parameter settings that result in optimal tissue contrast between the lobes. The results of this work were published online in Anatomia Histologia Embryologia (March 2010) DOI: 10.1111/j.1439-0264.2010.00995.x.

The analysis of spinal cord injury (SCI) in rats using high resolution MRI is elucidated in chapter 5. The rat animal model for SCI was established and routinely carried out by the research group of of Prof. Dr. J. Schoenen, in which dr. Felix Scholtes was a PhD researcher, from the University of Liege. The compression model for SCI results in a well-localized lesion with moderate tissue damage and remaining spared tissue. In this collaboration, the research goal was twofold. First it was aimed to define the possible role of high resolution MRI

in order to visualize and distinguish the pathological hallmarks of a compression lesion in the spinal cord in acute and chronic stages. This distinction will be based on signal intensities depicted on MR images. Different contrast weightings will be investigated to determine which weighting shows the typical lesion features in SCI. Secondly, an MRI based quantification method for spared white matter will be evaluated as it is known that the amount of spared white matter plays a key role in locomotor recovery. The MRI images presented in this study were complemented by histology .During this collaboration I was charged with the MRI acquisitions of the excised spinal cord blocks and contributed to the development of the MR based quantification method for spared white matter after SCI. The content of this chapter is published in Journal of Neuroscience Methods 2008;174 (2) : 157-67. A second paper is submitted to Spinal Cord and currently under revision.

In the following chapters 6 and 7, the possibilities of high resolution MRI (and the reference set of MR images) were evaluated with respect to the experimental use and the migrational behaviour of SPIO labeled cells (T-cells, macrophages and mesenchymal stem cells) in an animal model for multiple sclerosis (MS) by means of high resolution MRI. This animal model for MS, experimental auto-immune encephalomyelitis (EAE), represents a neurological disease of the CNS which is characterized by diffusely spread lesion areas in the brain and spinal cord. As MS is an auto-immune mediated disease, it is highly informative to unravel the role of T-cells (subtypes) and monocytes in order to better understand in the sequential development of disease processes in EAE (chapter 6). To detect the presence of specific cell types in the diffusely spread

lesion areas by MRI, they need a MR sensitive contrast label. SPIO labeling of monocytes will occur naturally as they are phagocytic cells. In contrast, T-cells are non-phagocytic cells which will need a transfection agent to internalize SPIO contrast particles. Before analyzing the role of T-cell in the animal model for MS, the optimal labeling conditions for T-cells will be investigated. Once the immune cells of interest are optimally labeled, their infiltration kinetics will be analyzed by T2-weighted MR imaging. The detection of contrast enhancements (hypo-intense signal intensities) originating from SPIO labeled immune cells on MR images will be done by comparing these images to the reference set of images shown in chapter 3. This experimental work was done by dr. Baeten Kurt and resulted in two research articles which were published in Journal of neuroimmunology 2008;195:1-6 and NMR in biomedicine April 2010 DOI: 10.1002/nbm.1501. My contribution to this work was mainly to present a detailed description of the localization of the contrast labeled cells within the CNS by means of the reference set of MR images.

Chapter 7 focuses on the visualization of SPIO labeled mesenchymal stem cells (MSCs) in the EAE animal for MS because these cells are expected to migrate towards injured inflammatory areas. It is suggested that these MSCs have anti-inflammatory capacities and trigger repair mechanisms to reduce the amount of tissue damage which makes them an interesting potential therapeutic tool for MS. Tracking these contrast labeled MSCs can provide information about their migration potential and mechanism. Since MSCs are also non-phagocytic cells the labeling with SPIO particles was first be optimized. After the cell labeling, the optimal administration route has to be determined since MS is a multifocal disease that needs a systemic delivery of MSCs to reach the widespread lesions in the CNS.

Chapter 8 contains the general conclusions of this multi-disciplinary work and present future perspectives for high resolution MRI in both small animal research and the clinical setting.

The Dutch summary is provided in chapter 9.

References

Acton PD, Kung HF. 2003. Small animal imaging with high resolution single photon emission tomography. Nuclear medicine and biology 30(8):889-895.

Baeten K, Hendriks JJ, Hellings N, Theunissen E, Vanderlocht J, Ryck LD, Gelan J, Stinissen P, Adriaensens P. 2008. Visualisation of the kinetics of macrophage infiltration during experimental autoimmune encephalomyelitis by magnetic resonance imaging. Journal of neuroimmunology 195(1-2):1-6.

Bammer R, Skare S, Newbould R, Liu C, Thijs V, Ropele S, Clayton DB, Krueger G, Moseley ME, Glover GH. 2005. Foundations of advanced magnetic resonance imaging. NeuroRx 2(2):167-196.

Benveniste H, Blackband S. 2002. MR microscopy and high resolution small animal MRI: applications in neuroscience research. Progress in neurobiology 67(5):393-420.

Brockmann MA, Kemmling A, Groden C. 2007. Current issues and perspectives in small rodent magnetic resonance imaging using clinical MRI scanners. Methods 43(1):79-87.

Budde MD, Frank JA. 2009. Magnetic tagging of therapeutic cells for MRI. Journal of nuclear medicine 50(2):171-174.

Colby LA, Morenko BJ. 2004. Clinical considerations in rodent bioimaging. Comparative medicine 54(6):623-630.

Hansen G, Crooks LE, Davis P, De Groot J, Herfkens R, Margulis AR, Gooding C, Kaufman L, Hoenninger J, Arakawa M, McRee R, Watts J. 1980. In vivo imaging of the rat anatomy with nuclear magnetic resonance. Radiology 136(3):695-700.

Hoey ET, Gopalan D, Agrawal SK, Screaton NJ. 2009. Chronic left ventricular failure: the role of imaging in diagnosis and planning of conventional and novel therapies. Clinical radiology 64(3):238-249.

Hu X, Norris DG. 2004. Advances in high-field magnetic resonance imaging. Annual review of biomedical engineering 6:157-184.

Lauterbur PC. 1973. Image Formation by Induced Local Interactions: Examples Employing Nuclear Magnetic Resonance. Nature 242(5394):190-191.

Lin MM, Kim do K, El Haj AJ, Dobson J. 2008. Development of superparamagnetic iron oxide nanoparticles (SPIONS) for translation to clinical applications. IEEE transactions on nanobioscience 7(4):298-305.

Pentney RJ, Alletto JJ, Acara MA, Dlugos CA, Fiel RJ. 1993. Small animal magnetic resonance imaging: a means of studying the development of structural pathologies in the rat brain. Alcoholism, clinical and experimental research 17(6):1301-1308.

Pirko I, Fricke ST, Johnson AJ, Rodriguez M, Macura SI. 2005. Magnetic resonance imaging, microscopy, and spectroscopy of the central nervous system in experimental animals. NeuroRx 2(2):250-264.

Rovira A, Leon A. 2008. MR in the diagnosis and monitoring of multiple sclerosis: an overview. European journal of radiology 67(3):409-414.

Runge VM. 2008. Advances in magnetic resonance (2008). Investigative radiology 43(12):893-898.

Serkova NJ, Garg K, Bradshaw-Pierce EL. 2009. Oncologic imaging end-points for the assessment of therapy response. Recent patents on anti-cancer drug discovery 4(1):36-53.

Soares DP, Law M. 2009. Magnetic resonance spectroscopy of the brain: review of metabolites and clinical applications. Clinical radiology 64(1):12-21.

Traboulsee A, Li DK. 2008. Conventional MR imaging. Neuroimaging clinics of North America 18(4):651-673.

Chapter 2

MRI principles

Outline chapter 2

2.1 Basic MRI principles

2.2 Spin echo imaging pulse sequence

2.3 Contrast modalities

2.4 Physical considerations when acquiring high quality MR images

2.5 Contrast agents

2.1 Basic MRI principles

Magnetic resonance imaging is based on the physical phenomenon called nuclear magnetic resonance (NMR). This method makes use of the charge and angular moment belonging to nuclei of certain atoms (Prince J, 2006). It is about nuclei with either an odd atomic number or an odd mass number. The nuclei of ^1H, ^{31}P are relevant in biomedical NMR because they have a high prevalence in biological systems what provides well detectable NMR signals above the background noise. In MRI, the hydrogen nucleus of water is primarily concerned due to the high water content in biological tissues, but hydrogen atoms of mobile molecules, such as lipids, are imaged as well. The hydrogen proton exhibits charge, mass and spin which results in combination with an applied magnetic field in a precession motion of the nuclear spin (Puddephat, 2005). This precession frequency is known as the Lamor frequency **(Eq. 2.1)** which is in turn proportional to the strength of the applied magnetic field (B_0) and the gyromagnetic ratio (γ) of the ^1H nucleus which has a value of 26.75 x 10^7 (rad / s T).

$$\omega = \gamma\, B_0 \qquad \textbf{Equation 2.1: Lamor frequency}$$

The precessing hydrogen nuclear spin produces a small magnetic field, a magnetic dipole which is usually represented as a vector μ **(Fig. 2.1A)**. In general, these magnetic dipoles are randomly orientated in tissues resulting in a zero net magnetization. When tissues are placed in an external magnetic field B_0, such as the MR spectrometer magnet, a slightly greater number of μ vectors align parallel (low energy state) compared to the vectors which align anti-parallel (high energy state) towards this external magnetic field **(Fig. 2.1B)**. The population difference between spins in the high and low energy state is proportional to the strength of the externally applied magnetic field B_0. The higher B_0, the larger the population difference. The magnetic moments of the low energy state spins, in excess of the high energy state spins, create a net magnetization (M_0) meaning that the tissue placed in the magnetic field becomes magnetized. This M_0-vector, also called the equilibrium magnetization, is orientated in the same direction as the applied external magnetic field along the z-axis.
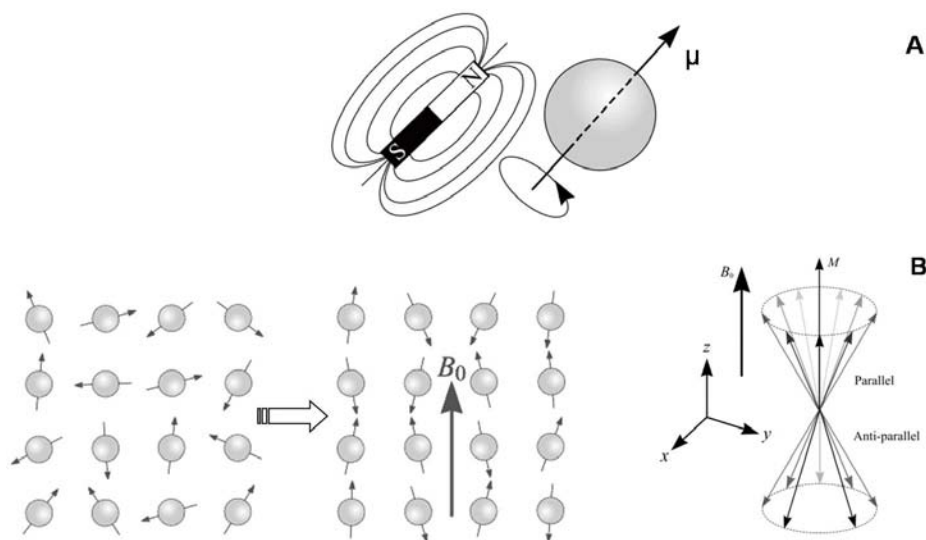
Figure 2.1: A) A charged, spinning hydrogen nucleus creates a small magnetic dipole moment which is represented as a vector μ. B) In the absence of an external magnetic field (B_0), the magnetic dipoles are randomly oriented. When an external magnetic field is applied, it causes the nuclear spins to align themselves parallel or anti-parallel towards B_0.
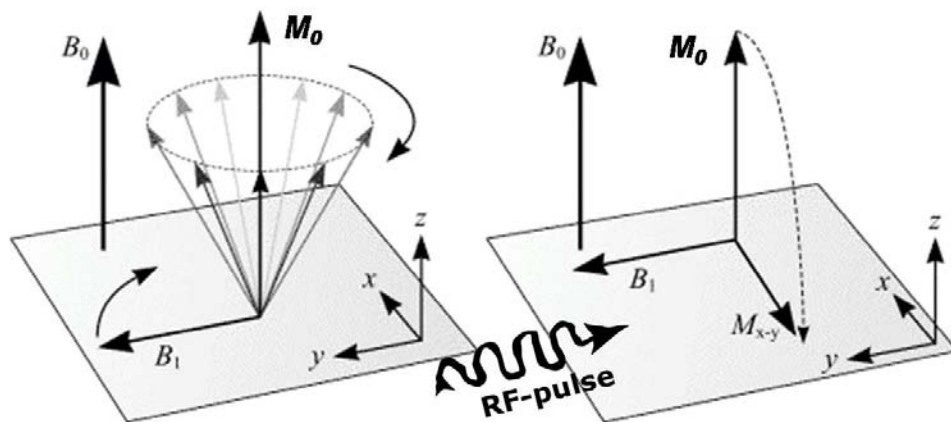
Figure 2.2: Effect of a 90° RF pulse on the net magnetization M_0. The M_0 vector is tipped from the longitudinal z-axis towards the transverse xy-plane, thereby creating the magnetisation vector Mxy.

In a next step, this equilibrium magnetization is exposed to radio frequency (RF) pulses which tip the magnetization away from the z-axis towards the transverse xy-plane **(Fig. 2.2)**. A radio wave is an oscillating electromagnetic field. Therefore the RF field is also known to as the B_1 field. It is oriented perpendicular to the main magnetic field B_0. To produce a 90-degree flip of the net magnetization, the energy dose of the applied RF pulse is precisely determined to achieve an equal distribution of parallel and anti-parallel spins within the tissue. When turning off the RF pulse, only transverse magnetisation Mxy remains (Mz = 0, Mxy = M_0). The instable system will return to a state of equilibrium by dispersing the absorbed energy. During these relaxation processes, the absorbed energy is transferred from the spins to the lattice, called longitudinal or T1-relaxation, or redistributed within the spin system referred to as transverse or T2-relaxation. In the longitudinal relaxation process, the component Mz increases over time until it reaches its maximum starting point M_0 **(Fig. 2.4)**. This exponential regrowth of the magnetization along the Z-axis is completed when the spins have returned to the Boltzmann equilibrium state where low energy state spins are in excess over high energy state spins. The xy-plane magnetization Mxy, decays exponentially in time with a decay time T2 **(Fig. 2.5)**. The signal fades as the individual spins loose their phase coherence, making the vector sum in the xy-plane equal to zero.

2.2 Spin echo imaging pulse sequence

The spin echo (SE) sequence is one of the most applied sequences for MR-imaging. A spin echo time diagram is shown in **figure 2.3**. The sequence starts with a slice selective 90° RF pulse which tips over the tissue magnetization in the slice towards the transverse plane. Then, the spins diphase in the transverse plane. After a time point, called TE/2, a refocusing 180° pulse is applied to the system, resulting in a rephasation of the spins. When the spins have completely regained their coherence, a spin echo is generated at time point TE. The echo time TE is described as the time between the initial 90° pulse and the detection of the spin echo signal. This 90° - 180° echo pulse concept is

repeated several times to obtain the desired SNR. The time between two 90° pulses is called the repetition time TR. SE sequences are used to obtain T1-, T2- and proton density weighted images. The signal intensity and contrast depends on the TR and TE parameter settings and the T1, T2 and M_0 values of the tissue structures.
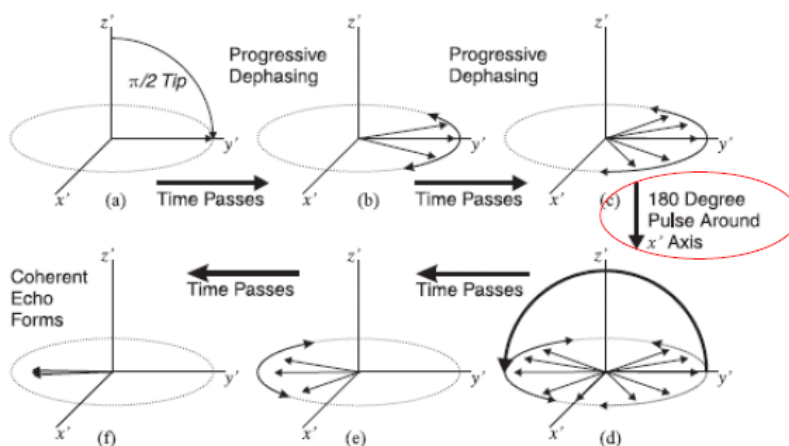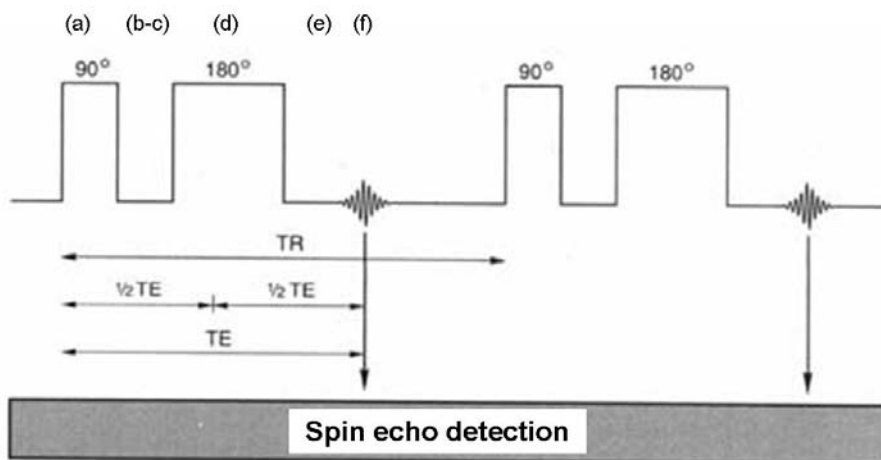
Figure 2.3: Spin echo sequence. The upper image shows the time diagram of the applied RF-pulses in a SE sequence. It starts with a 90° pulse (a), the Mxy magnetization dephases (b-c) until a 180° refocusing pulse is applied at ½ TE (d). The magnetization vector refocuses and will be detected at time point TE (f).The resulting effects on the magnetization vector are illustrated below.

2.3 Contrast modalities

There are many sources of contrast in an MR image. The simplest is proton density (PD) which refers to the concentration of mobile protons in tissue. It shows tissues with high water content as hyper-intense regions whereas proton-poor tissues are depicted as hypo-intense zones in the images. This also means that the contrast in all images, even in T1- or T2-weighted images, is always (somewhat) influenced by the proton concentration. PD-weighted images should have a short TE (e.g. 20-30 ms) to minimize the T2 signal decay and a long TR (p.e. 2-5 s) to decrease T1 signal loss (Nitz and Reimer, 1999).

Tissue contrast can also be achieved by weighting the image sequence to display differences in proton relaxation rates (1/T1 or 1/T2). They are called T1- or T2-weighted images respectively. Each body tissue has its own T1- and T2-value which provides information about tissue organisation and, based on difference in T1 or T2 values between tissues, it becomes possible to create contrast between them on an MR image. To achieve T1-weighted images, both TE and TR parameters must be chosen short. During the T1-relaxation process high energy state protons will discard their energy towards the lattice, finally returning to the equilibrium magnetisation state which means that all the excited spins are completely returned to their ground state. The recovery of the longitudinal magnetization M_Z depends on the T1-relaxation rate of the tissue **(Fig. 2.4)** and is described by the following equation **(Eq. 2.2)**. Water protons of mobile tissues, such as cerebrospinal fluid, have a slower T1-relaxation rate which results in hypo-intense signals while water protons of organised tissues relax faster and show hyper-intense signals on T1-weighted MR images.

$$M_Z = M_0 \left[1 - e^{(-t/T1)}\right]$$ **Equation 2.2: Spin lattice or T1-relaxation**
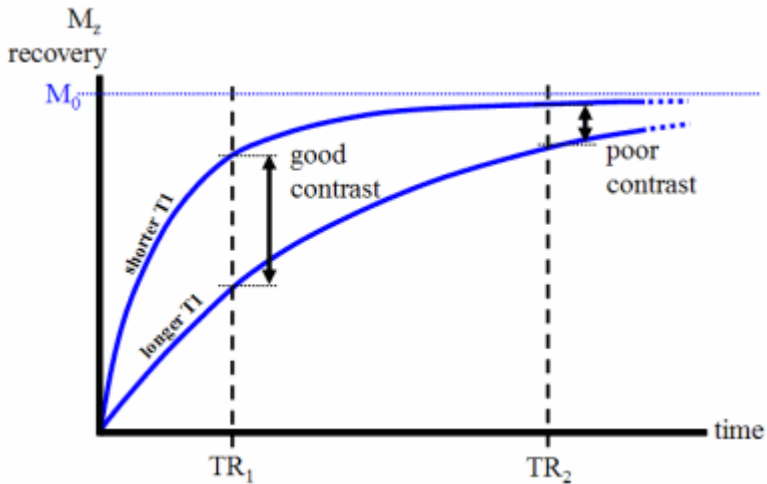
Figure 2.4: **T1-relaxation curve** shows that the longitudinal magnetization becomes re-established in an exponential manner characterized by a time constant, called T1.

T2-weighted image contrast is obtained by imaging with a long TR and TE. This imaging technique relies upon the loss of phase coherence of spins after a 90° pulse. When spins come into close proximity with each other, they experience a slight disturbance of the B_0 field which results in local fluctuations in the Lamor frequency meaning that some spins precess slightly slower or slightly faster. Consequently the net component of the magnetization in the transverse plane dephases **(Fig. 2.5)** and the detectable signal exponentially decays as described by **equation 2.3**. Strongly organised tissues have a shorter T2-relaxation time than weakly organised tissues.

$$M_{XY} = M_0 \left[e^{-t/T2}\right] \qquad \textbf{Equation 2.3: Spin spin relaxation or T2-relaxation}$$
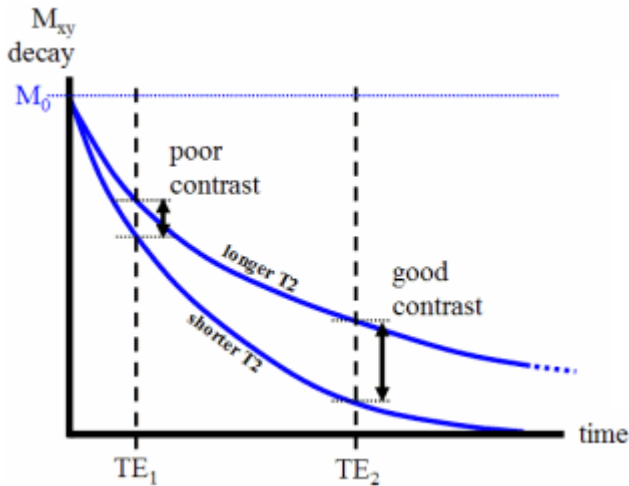
Figure 2.5: T2-relaxation curve showing the transverse magnetization. The signal decay decreases exponentially by a time constant, called T2. Strong organized tissues have a short T2, while mobile structures display a long T2.

2.4 Physical considerations when acquiring high quality MR images

With regard to small animal MR imaging, it would be desired to obtain images with excellent resolution and high SNR in a time period as short as possible. But all of these components are related to each other (Benveniste and Blackband, 2002).

The SNR is described as the ratio of the average signal for the tissue to the standard deviation of the noise in the background of the image (Weber, 2001). Both instrumental and acquisition related factors have an influence on the SNR **(Fig. 2.6)** (Takahashi et al., 2003). Field strength influences the SNR. It increases almost as the square of the field strength (SNR ~ $B0^{7/4}$). But usually, the user has only access to specific a scanner and thus the field strength will be

fixed. User adjustable settings which have an effect on SNR are voxel volume and acquisition time. Averaging the signal by repeated acquisitions increases the SNR by the square root of the number of averages (NA). This latter is the easiest way to increase SNR, but it enlarges the acquisition time. Although this can be compromised by lowering the image resolution. A lower resolution indicates a larger voxel size, thus also increased SNR. The SNR increases in proportion to voxel volume (1/resolution) and the square root of the number of phase encodings steps. SNR decreases with the field of view squared (FOV^2). Halving inplane resolution, especially the number of phase encoding points (Np), of a 2D image will increase the SNR by a factor 4 and decreases acquisition time. Acquisition time is determined by the product of TR, NA and Np.

As indicated above, one has to take into account that SNR, resolution and acquisition time are interdependent. A good SNR image is compromised by low resolution and/or longer acquisition time.
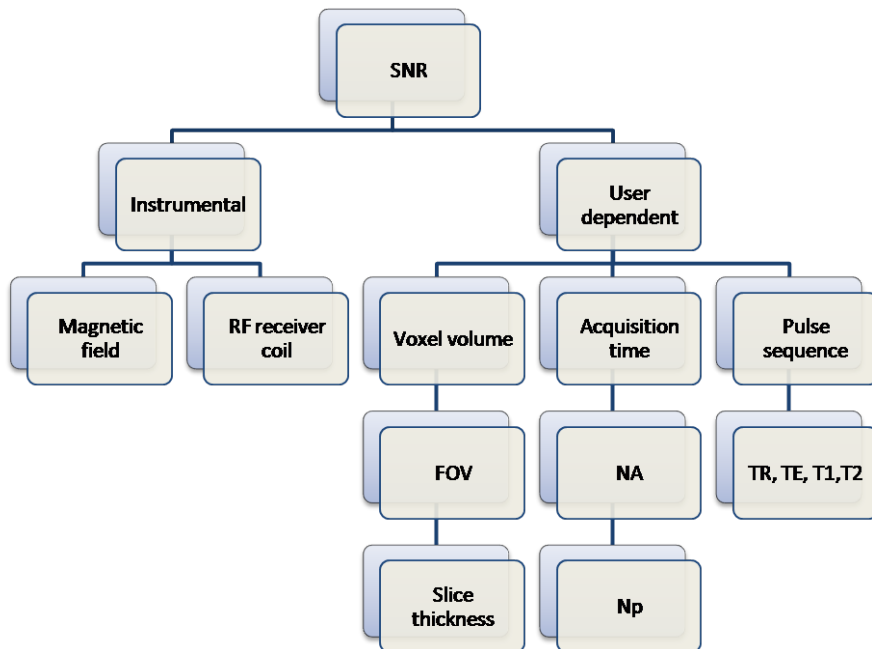
$$SNR \sim \left\{ \frac{FOVx}{Nf} * \frac{FOVy}{Np} * SL \right\} * \sqrt{\frac{NA * Nf * Np}{BW}}$$

$$SNR \sim \{voxelvolume\} * \sqrt{totalacquisitiontime}$$

Figure 2.6: Instrumental and user defined settings to control SNR. SNR is influenced by parameters which have an effect on voxel volume and the total acquisition time. Voxel volume is changed by the field of view (FOV) and the slice thickness (SL). The acquisition time is determined by the number of averages (NA), number of frequency encoding points (Nf), number of phase encoding points (Np) and bandwidth (BW).

2.5 Contrast agents

The MR image is depicting the hydrogen atoms in biological tissues. There are many sources of contrast in an MR image such as hydrogen concentration or differences in proton relaxation as described above. But also exogenous materials can alter the intensity of MR signals. These materials are known as contrast agents and influence the relaxation rate of protons in their proximity (Caravan, 2007). All contrast agents shorten the T1- and T2-relaxation rate. It results in positive or negative contrast on a T1- or T2-weighted imaging sequence, respectively.

Recently, a growing interest has risen to extend conventional anatomical and physiological MR imaging of the clinic to the cellular and molecular level (Arbab et al., 2006; Modo, 2007). Therefore contrast agents can be used to visualize cells or even molecules (Modo et al., 2005). It makes them interesting for performing migrational studies. In the context of this work, only T2 contrast agents are further discussed.

T2 contrast can be obtained by using small iron oxide particles which have superparamagnetic properties (Corot, 2007). These small particles of iron oxide (SPIOs) consist of a magnetite (Fe_3O_4) core enclosed in a coating. Based on the diameter of the particles, they are divided in several groups such as ultrasmall particles (USPIOs), small particles (SPIOs) and micrometer sized SPIO's, called MPIOs. Dextran-coated nanoparticles are biodegradable and therefore do not show long-term toxicity. Intracellular dextranase cleaves the dextran coating and the iron oxide is solubilized into iron which is incorporated in the hemoglobin pool. In the clinic, some of these contrast particles are used to examen the gasto-intestinal tract, liver or inflammatory lesions. The human body contains phagocytic cells, such as macrophages and Kupffer cells, which are known to take up these iron particles spontaneously. Moreover, non-phagocytic cells can also be forced to internalize the contrast particles (Bulte, 2006). Transfection agents such as poly-L-lysine or protamine sulfphate are used to facilitate the uptake of iron particles by these cells **(Fig. 2.7).** Therefore cell labeling with magnetic nanoparticles has become an appealing method for in vivo cell imaging.
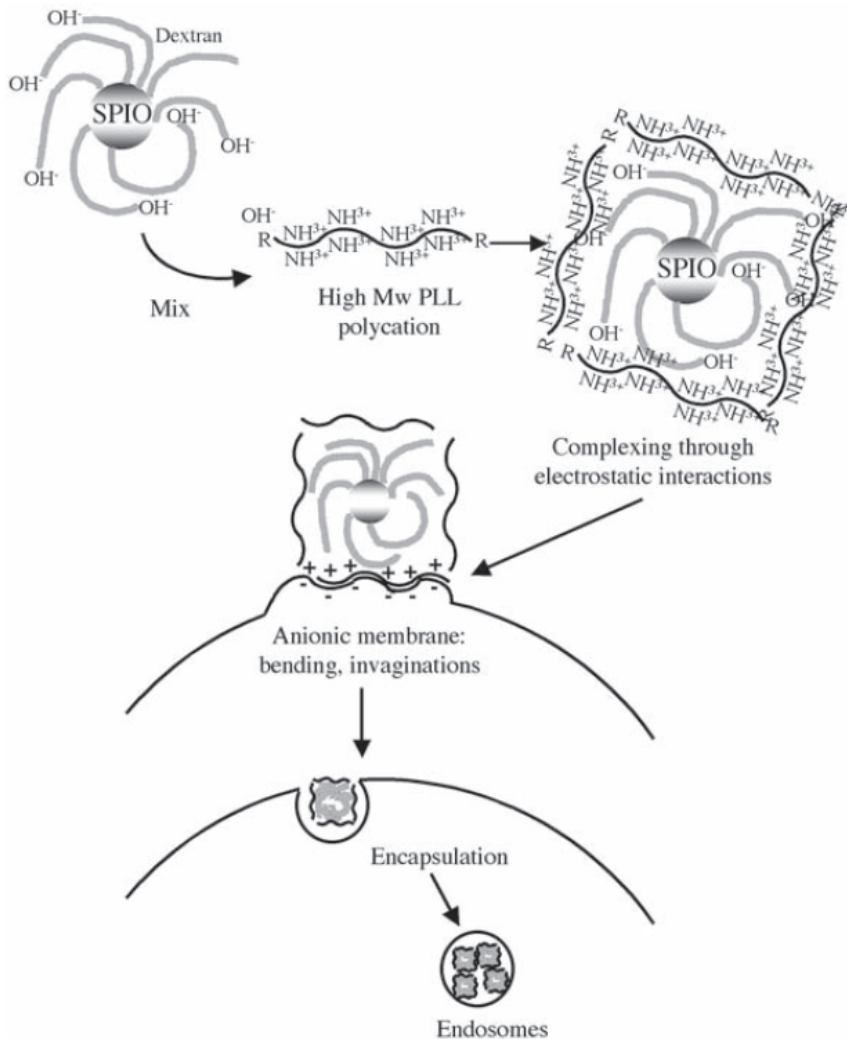
Figure 2.7: Intracellular labeling mechanism for non-phagocytic cells. (Bulte 2006). The negative surface charge of the dextran coating binds to the positive transfection agent poly-L-lysine (PLL) and forms SPIO-PLL complexes. When added to a cell culture, the positive charge of the PLL will interact with the negative surface of the cells in culture. Then the membrane forms invaginations and encapsulates the particles resulting in endosomes containing the particles.

References

Arbab AS, Liu W, Frank JA. 2006. Cellular magnetic resonance imaging: current status and future prospects. Expert review of medical devices 3(4):427-439.

Benveniste H, Blackband S. 2002. MR microscopy and high resolution small animal MRI: applications in neuroscience research. Progress in neurobiology 67(5):393-420.

Bulte JW. 2006. Intracellular endosomal magnetic labeling of cells. Methods in molecular medicine 124:419-439.

Caravan P. 2007. Molecular and cellular MR imaging. Chapter 2 Physicochemical principles of MR contrast agents. New York: CRC Press. p 13-36.

Corot C, Port, M., Guilbert, I., Robert, P. 2007. In: Modo M, Bulte, J., editor. Molecular and cellular MR imaging. Chapter 4 Superparamagnetic contrast agents. New York: CRC Press. p 60-83.

Modo M, Bulte J. 2007. Molecular and cellular MR imaging. Chapter 1 What is molecular and cellular imaging? New York: CRC Press. p 1-9.

Modo M, Hoehn M, Bulte JW. 2005. Cellular MR imaging. Molecular imaging 4(3):143-164.

Nitz WR, Reimer P. 1999. Contrast mechanisms in MR imaging. European radiology 9(6):1032-1046.

Prince J LJM. 2006. Medical imaging signals and systems. Part 5 Magnetic resonance imaging. New Jersey: Pearson Education. p 379-464.

Puddephat M. 2005. Principles of Magnetic Resonance Imaging http://www.easymeasure.co.uk/principlesmri.aspx.

Takahashi M, Uematsu H, Hatabu H. 2003. MR imaging at high magnetic fields. European journal of radiology 46(1):45-52.

Weber D. 2001. MRI quality. http://dnl.ucsf.edu/users/dweber/.

Chapter 3

Rat brain and spinal cord architecture studied by means of high resolution MRI

Outline chapter 3

3.1 General introduction

> **3.1.1 The role of MRI in experimental animal studies concerning the CNS**

> **3.1.2 The central nervous system of the rat**

3.2 Materials and methods

3.3 Results and discussion

> **3.3.1 Selection of MRI acquisition parameters TR and TE**

> **3.3.2 Reference frame of the rat's central nervous system**
> > **RAT BRAIN TISSUE**
> > > **Influence of tissue fixation on image quality**
> > > **PD- versus T2-weighted imaging sequences**
> > > **Matching histologic sections and annotation**

> > **SPINAL CORD TISSUE**

3.4 Conclusions

3.1 General introduction

3.1.1 The role of MRI in experimental animal studies concerning the CNS

The application of MRI using small-animal models is strongly implemented in experimental studies concerning human neurological diseases. MRI is probably one of the best imaging methods that has developed into a very interesting tool allowing the interpretation of the complex spatial rodent brain architecture (Benveniste and Blackband, 2006; Walczak and Bulte, 2007). Its ability to capture anatomical information in a non-invasive manner and with a high spatial resolution makes it an appealing technique to study soft tissues as the CNS. The degree of resolution is situated between macroscopic anatomy, which visualizes objects by the naked eye, and the cellular histology (Johnson et al., 1997). Moreover, the technique allows to acquire images of a single specimen in the three orthogonal (or other) directions without repositioning the sample or physical slicing the tissue. Advances in magnetic resonance *in vivo* neuro-imaging offer serial follow-up methods for tracking the course of neurological disorders in small-animal models. The ability to resolve rat brain anatomy by MRI is essential for the detection of macroscopic abnormalities, such as atrophy, demyelination, tumor formation, stroke, or inflammation (Brockmann et al., 2007). A well established reference set of images can also be used to phenotype genetic modified rats. It is well known that MR images acquired *in vivo* have a lower spatial resolution than those obtained *ex vivo.* This discrepancy can be mainly ascribed to scan time restriction and motional artefacts, which decrease the overall contrast-to-noise ratio and the signal-to-noise ratio, resulting in some decrease in quality of the image (Takahashi et al., 2003).

To date, several groups have made conventional histological atlases of the rat brain which consist of histological sections accompanied with their annotation figures (Paxinos and Watson, 2007; Pellegrino et al., 1979; Swanson, 2003). Attempts to visualize the rat brain using *in vivo* MRI were performed by Pfefferbaum et all. on a 3T clinical human scanner. They created images with an in-plane resolution of 200 x 200 µm, which is far above the criteria for MR

microscopy. The group of Koretsky (Aoki et al., 2004) performed manganese-enhanced *in vivo* MRI at 11.7 T with the use of a surface coil to determine the fine structure of the rat brain. They showed signal enhancements in the olfactory bulbs, hippocampus, basal forebrain, cerebellum and pituitary gland.

The present chapter focuses on the *ex vivo* acquisition of high resolution (9.4T) MR images without the use of contrast agents to visualize the detailed anatomy of the central nervous system of the naïve rat. This reference frame can be used to trace structural and contrast changes in images of pathologic or contrast treated animals (*ex vivo* as well as *in vivo*). In this work, the high resolution reference frame of the spinal cord is used in spinal cord injury studies to trace abnormal signal intensities originating from specific lesion characteristics such as oedema or bleeding (chapter 5). Further on, the reference set of images is applied to visualize the infiltration of labelled immune cells in an animal model of multiple sclerosis which was in co-operation with the doctoral work of Dr. Kurt Baeten (chapter 6). In a last application, the reference frame is used to visualize the fate of contrast labeled stem cells (chapter 7).

To construct this reference frame, consecutive high resolution MR images were acquired in three orthogonal slice directions on a 9.4 T vertical bore magnet to depict the complete architecture of the rats CNS *ex vivo* without using contrast agents or surface coils. A combination of conventional imaging sequences such as proton density and T2-weighted sequences, were applied to visualize the brain and spinal cord. Internal brain structures seen on MR images were identified using the stereotactic rat brain atlas from Paxinos (2006). The MRI reference frame was completed with matching histologic sections. Note that in this chapter only a representative selection of the acquired MRI images is shown.

3.1.2 The central nervous system of the rat

All mammalian nervous systems contain two major anatomical divisions, i.e. the central nervous system and the peripheral nervous system. The central nervous

system covers all the tissues of the brain and spinal cord. These structures are encased in bone. The brain lies within the skull and the spinal cord tissue is surrounded by the vertebras. All nervous tissue, other than the brain and spinal cord belong to the peripheral nervous system.

Anatomical planes applied to the CNS of rodents

When visualizing the inside brain structures of the rat by means of MRI, images are usually acquired in slice directions which are parallel to one of the three anatomical planes **(Fig. 3.1)**. The anatomical planes for rodents differ from these for humans and more specific for the spinal cord. The midsagittal plane cleaves the CNS into symmetrical right and lefts halves. Sections taken parallel

to this midsagittal plane are sagittal. The two remaining anatomical planes are orthogonal to the sagittal plane and to one other. The horizontal or transverse plane is parallel to the ground thereby splitting the brain and spinal cord into a dorsal and ventral part. The coronal (axial) plane is perpendicular to both the horizontal and sagittal plane. A section in this plane divides the brain and spinal cord into anterior (rostral) and posterior (caudal) divisions.
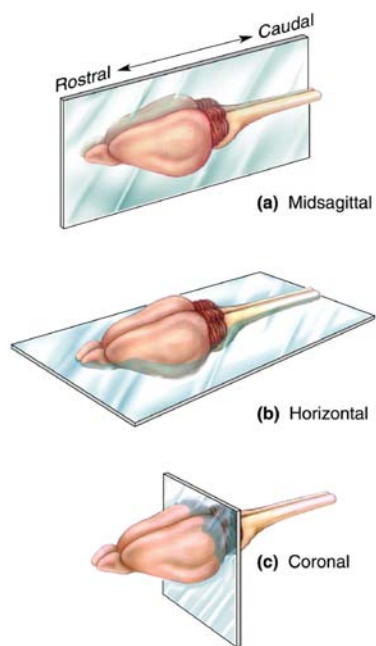
Figure 3.1: Anatomical planes, i.e. mid-sagittal, horizontal/tranverse and coronal plane, as projected on the rodent brain. (Bear et al., 2007)

Gross anatomy of the CNS

As indicated in **figure 3.2**, the brain is subdivided in the cerebrum, the cerebellum and the brainstem. The largest part of the brain, the cerebrum, contains two cerebral hemispheres, which are separated by a deep sagittal

fissure. Together they form the telencephalic region of the brain. In rats, the surface of these hemispheres does not show as many convolutions (gyri) as seen on a human cerebral surface. Another difference is the size of the olfactory bulb of rodents. In relation to the size of the brain, rats have a larger olfactory bulb as compared to humans. The diencephalon also belongs to the cerebrum and is completely covered by the telencephalic hemispheres. Caudal to the cerebrum lies the brainstem which is connected to the spinal cord. The brainstem consists of the mesencephalon, the pons and medulla. The cerebellum, positioned on the dorsal side of the brainstem, shows a limited foliated surface.

(d)
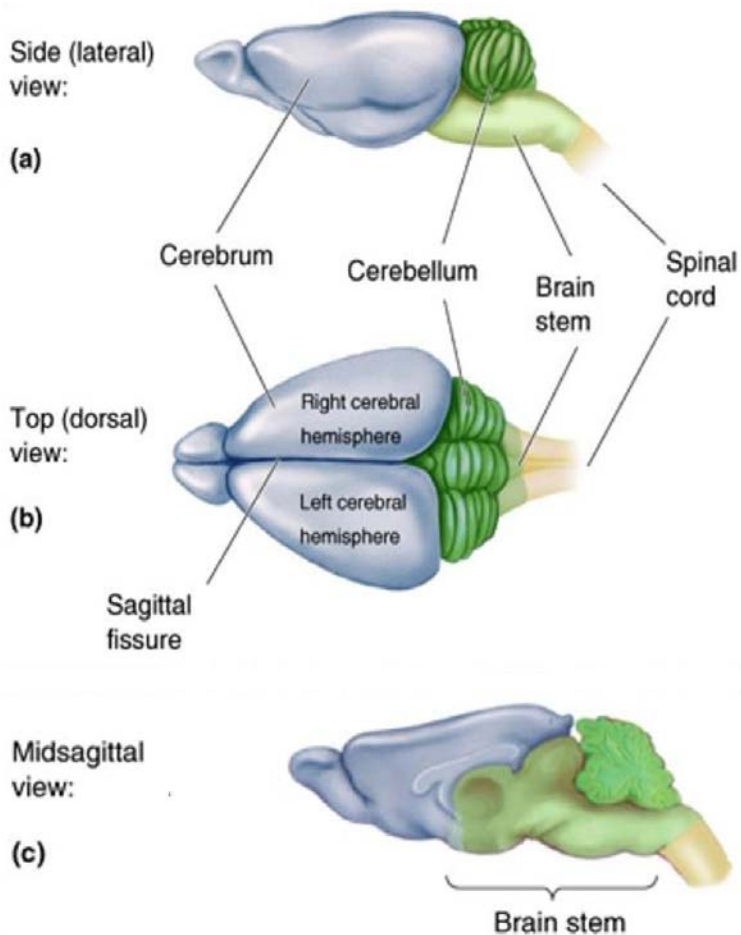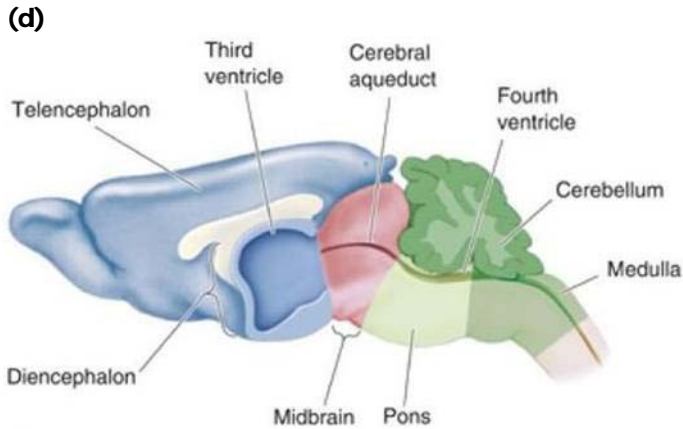
Figure 3.2: CNS of the rat depicted from a lateral (a), dorsal (b) and mid-sagittal (c) view. Major brain regions are annotated on a mid-sagittal view (d). Parts belonging to the cerebrum are indicated by a blue color. The cerebellum is positioned at the dorsal side of the brainstem. The brainstem itself contains the midbrain, pons and medulla. Caudal to the medulla starts the spinal cord. (Bear et al., 2007)
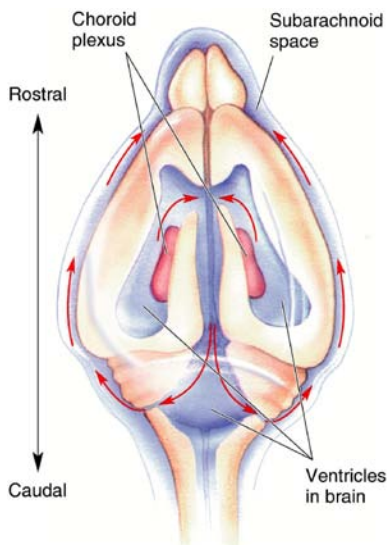
Each division of the brain contains a part of the ventricular system **(Fig. 3.3)**. The two lateral ventricles are situated in the telecephalic hemispheres. The diencephalon houses the third ventricle which is connected by the cerebral aqueduct of the mesenchephalon to the fourth ventricle. The latter cavity is situated between the cerebellum and the caudal part of the brainstem. Cerebrospinal fluid, continuously secreted by the choroid plexus, flows through the ventricle system towards the subarachnoid space.

Figure 3.3: Ventricular system projected upon the rat brain, showing the flow direction of the cerebrospinal fluid. (Bear et al., 2007)

The spinal cord, situated inside the vertebral column, forms a runway for exchanging information from the body to the brain and the other way around. Over its total length, the spinal cord is divided in four anatomical regions i.e. cervical, thoracic, lumbar and sacral. As seen in humans, the rat's spinal cord also shows an enlargement at cervical and lumbar level, indicative for innervation of the fore and hind limbs respectively.

3.2 Materials and methods

Animals
Female Lewis rats (n=15) were ordered from Harlan CPB (Zeist, The Netherlands). Animals were housed in cages with food and water *ad libitum* until they reached the age of 8 weeks (average weight of 150 - 200 gram). *Ex vivo* MR imaging was performed on dissected fixed (n=5) and non-fixed (n=10) brain and spinal cord specimens surrounded by their bone structures. Unfixed tissue was dissected after decapitation. For fixed CNS tissue, animals were anesthetised by intraperitoneal Nembutal[®] (Natriumpentobarbital 60 mg/ml - 75 µl/100 g body weight). Subsequently, animals were intracardially perfused using 1 ml heparin (1000 I.U./ml) and chilled NaCl 0.9 % to wash out the blood. Next, a 4% paraformaldehyde (PFA) solution (pH 7.4) (4% PFA in 0.01M PBS) was perfused. After dissection, the fixed CNS tissue was stored for MRI in 4% PFA for at least 1 week at 13°C. All experimental procedures were approved by the Ethical Committee for Animal Experiments of the Hasselt University, Diepenbeek, Belgium.

Magnetic resonance imaging

MRI was performed on brain and spinal cord of healthy 8 weeks old Lewis rats. Imaging acquisitions were done in a 25 mm birdcage coil on a 9.4T vertical bore magnet (Varian Inova 400 spectrometer, Varian, Nuclear Magnetic Resonance Instruments, Palo Alto, California, USA) at 4°C in three orthogonal planes. High resolution MR reference images were obtained using a proton density (PD) weighted spin echo sequence [TR = 2500ms / TE = 18ms (TR = repetition time / TE = echo time)] and a T2-weighted [TR = 2500ms / TE = 55 or 35ms for unfixed or fixed tissue respectively] spin echo sequence. These TE value were selected from a series of TE values based on criteria for image quality **(Fig. 3.4)**.

Consecutive 1-mm-thick slices covering the complete rat brain were acquired in all three orthogonal directions using the following parameters: field of view (FOV) of 25 x 25 mm and data matrix of 650 x 650 in the axial slice direction and FOV 25 x 30 mm and data matrix of 650 x 780 for the horizontal and sagittal planes, an in-plane pixel resolution of 40×40 µm and number of averages (NA) of 32 for the PD-images and 64 for T2-weighted images. The acquisition time for PD- and T2-weighted imaging was 14 hours and 28 hours, respectively. Imaging of the spinal cord was performed with a FOV of 10 x 10 mm in the axial slice direction and 30 x 10 mm in the horizontal and sagittal directions, an in-plane resolution of 45 x 45 µm and a NA of 50 for the PD-weighted images. The SC was devided in separate parts with a length of 30 mm. PD-imaging of each part was done in about 8.5 hours.

The anatomical landmark, bregma, on the skull cap was localized by the tip of a water filled capillary of 1 mm inner diameter. Hereto, a sagittal incision on the top of the head was performed, and the skin and soft tissue covering the bone were retracted laterally and removed so that the bone sutures (coronal, sagittal and lambdoid) were exposed and clearly visible.

Morphometric analysis of the spinal cord

MR images (n = 8 images per level), representing the cervical, thoracic, lumbar or sacral level of the spinal cord, were analysed using the software program Image J of the National Institute of Health (Rasband, 1997-2008). For each image the total coronal surface area of the spinal cord was determined as well as the areas of the gray and white matter tissue.

Light microscopy

Rat brain specimens were fixed using perfusion fixation as described above. The intracranial tissue was removed and post-fixed in 4% PFA for 1 week. Then the brain was cut in 5-mm-thick coronal, sagittal or horizontal tissue blocks and routinely embedded in paraffin wax (Leica TP 1020 tissue processor). 5-µm-thick sections were mounted on poly-L-lysine coated microscopical slides. Sections were stained with Klüver-Barrera (KB), which stains white matter blue and cell nuclei purple. Protocol KB-staining steps were adapted from Histotechniek/Cyto-Visie 2001 volume 3: deparaffinize and hydrate the sections (1); 3 x 2 minutes (min) xylol, 3 x 2 min ethanol 100%, 2 min ethanol 75%. Leave the tissue in luxol fast blue solution (LFB) (Gurr, VWR International, Belgium, cat.nr 340443P) (0.1% LFB in ethanol 96% and 5 ml acetic acid 10%) for 1 hour at 56°C (2), rinse excess of stain in alcohol 96% (3) and rinse in distilled water (4). Differentiate the slides in lithium carbonate solution (0.05%) for 5 to 10 seconds (5) and continue the differentiation in alcohol 70% until the gray matter is clear and white matter sharply defined (6). Rinse again with distilled water (7). Check microscopically. Repeat the differentiation if necessary starting at step 5. When all slides have been collected in distilled water, they are counterstained with cresyl violet solution (Gurr, VWR International, Belgium, cat. Nr.340245L) (0.3% cresyl violet in H_2O, add 5 drops 10 % acetic acid to every 30 ml before use) for 1 minute (8), rinse short in alcohol 96% (9) and continue the dehydration through two changes of absolute ethyl alcohol and xylene, two changes each, for 2 minutes (10). Mount the sections in DPX (Gurr, VWR International, Belgium, Cat. Nr. 361252B). Histological slides were digitalized using a Mirax Desk Slide Scanner and analyzed by the Mirax Viewer software (release 1.9 Zeiss MicroImaging GmbH, Germany).

3.3 Results and discussion

The optimal acquisition parameters are determined in order to create a reference frame with images of high quality of the rat's CNS.

3.3.1 Selection of MRI acquisition parameters TR and TE

PD-, T1- and T2-weighting are commonly used contrast modalities in MRI. Tissue contrast in the image has contributions from each of the various intrinsic contrast mechanisms, but is weighted more toward one than the others. This weighting is accomplished by the selection of the timing parameters of the pulse sequence. For spin echo sequences as used in this work, these parameters are the TR and the TE. With regard to a proper reference frame of the CNS, it is important to choose parameters which lead to images with optimal contrast between the structures, but also with a high SNR. Since there is only a 'best TR/TE combination' for a specific anatomical structure, the term optimal parameters refers to the TR/TE combination that results in the best overall image quality. The TR/TE combinations mentioned in this chapter therefore have to be seen as starting values for further fine-tuning for a well-defined anatomical structure. For PD acquisitions, TR must be long (usually ≥ 2000 ms or longer) to reduce T1-weighting while TE has to be short (≤25ms or as short as possible) to diminish the T2-weighting. The PD- images shown here were acquired with a TE of 18 ms combined with a TR of 2500 ms. The same long TR value was also used to acquire T2-weighted images. To select the optimal TE for T2-weighted imaging, imaging acquisitions were performed with variable TE values, i.e. 18, 25, 35, 45, 55, or 70 ms for both unfixed and fixed rat brain tissue. **(Fig. 3.4)**. **Figures 3.4 A and B** show that the overall signal intensities diminish with increasing TE value. Signal intensity also fades away faster when the tissue was formalin fixed. Therefore, a shorter TE value was selected to perform T2-weighted imaging on fixed tissue. Taken the criteria which determine image quality into account i.e. contrast, in-plane resolution, slice thickness and SNR, TE values of 55 ms and 35 ms were selected as optimal for unfixed or fixed nervous tissue respectively **(Fig. 3.4 C-D)**. **Figures 3.4 C and D** are shown with optimized contrast and brightness settings and do correspond with the images (55 en 35 ms respectively) shown in the TE series (A and B).
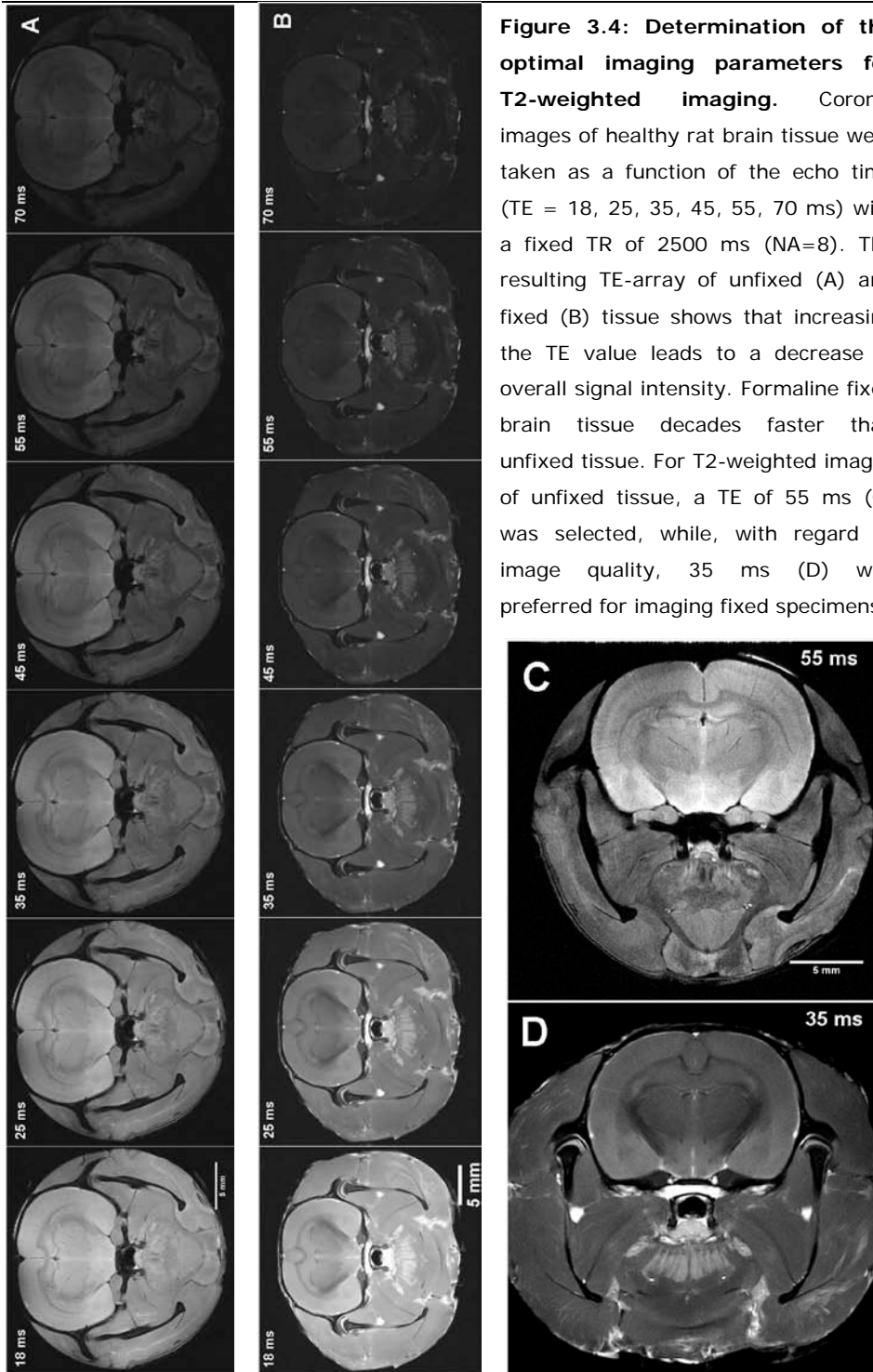
Figure 3.4: Determination of the optimal imaging parameters for T2-weighted imaging. Coronal images of healthy rat brain tissue were taken as a function of the echo time (TE = 18, 25, 35, 45, 55, 70 ms) with a fixed TR of 2500 ms (NA=8). The resulting TE-array of unfixed (A) and fixed (B) tissue shows that increasing the TE value leads to a decrease in overall signal intensity. Formaline fixed brain tissue decades faster than unfixed tissue. For T2-weighted images of unfixed tissue, a TE of 55 ms (C) was selected, while, with regard to image quality, 35 ms (D) was preferred for imaging fixed specimens.
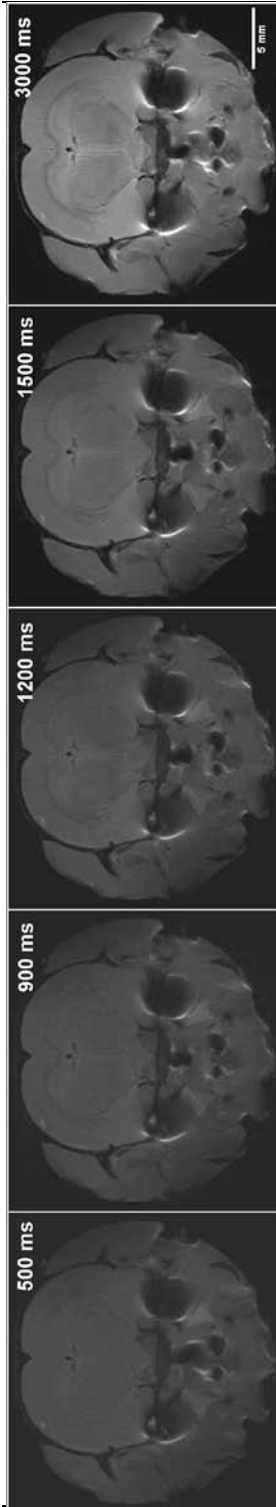
Figure 3.5: Determination of the optimal imaging parameters for T1-weighted imaging. Coronal images of healthy rat brain tissue were taken as a function of the repetition time (TR = 500, 900, 1200, 1500 and 3000 ms) with a fixed TE of 18 ms (NA=8). T1-weighting clearly decreases the contrast between the anatomical structures of the brain of unfixed specimens. Therefore T1-weighted images are not presented in this thesis unless otherwise stated.

To select the optimal TR setting for T1-weighted weighted images, a short TE of 18 ms was used in combination with variable TR values, i.e. 500, 700, 900, 1200, 1500 and 3000 ms **(Fig. 3.5).** As demonstrated in **figure 3.5**, T1-weighted images did not show gray-white matter boundaries as well as T2-weighted images. There was in general less contrast between the anatomical structures of the brain. This indicated that the T1-decay times of the different anatomical structures do not differ enough to deliver contrast in T1-weighted images. Therefore high resolution T1-weighted images were not included in this thesis unless otherwise stated.

3.3.2 Reference frame of the rat's central nervous system

Based on the selected imaging parameters for optimal image quality, a high resolution reference frame of the rat's central nervous system was created for both unfixed and fixed tissue specimens. MR images of brain and spinal cord encased in the skull or vertebral column are acquired *ex vivo* for 8 weeks old rats and provide good visualization of the gross anatomy as well as the overall tissue structure. Moreover, exquisite anatomical details can be demonstrated non-destructively for the three slice directions. At a spatial resolution of 40 µm by 40 µm following anatomical structures can be clearly identified: the hippocampal area, the corpus callosum, the thalamus, the caudate/putamen nucleus. But also the spinal cord images **(Fig. 3.16)** show clearly the butterfly-shaped gray matter surrounded by the white matter and secondly, allow the detection of the different anatomical regions, i.e. cervical, thoracic, lumbar and sacral, based on the characteristic shape of the gray matter or the relative amount of white matter. Brain or spinal cord locations which are of main importance for following chapters are bordered in red or green. They are annotated and used in this chapter to describe the influence of tissue fixation (red bordered) and imaging contrast parameters (green bordered). The accomplished MR images are compared with matching Klüver-Barrera stained brain sections **(Fig. 3.13 and 3.14).**

RAT BRAIN TISSUE

Brain tissue was imaged within its skull to avoid the weak tissue from being harmed during isolation. The skull also has a supportive function towards the tissue, meaning that tissue deformation is avoided. Imaging of the brain inside the skull preserves regional relationship with the surrounding bony and meningeal structures. In this study, the position of the anatomical landmark bregma, was indicated by a water filled capillary **(Fig. 3.6 k)** which is seen as a hyper-intense circular spot above the skull.

Coronal imaging plane

The rat brain is rostro-caudally depicted in **figure 3.6** as consecutive 1-mm thick sections. Images of high quality were acquired *post-mortem* of unfixed (A) and fixed (B) brain tissue with a PD imaging sequence. The most frontal located structure is the olfactory bulb and is seen in images a-e. Then the telencephalon is displayed (f-j) consisting of the cortex, nucleus caudatus – putamen, corpus callosum and the lateral ventricles. Starting from image k till m, the diencephalon is shown. The diencephalic structures are surrounded by the telencephalon. The brainstem is visible over image n till w and can be subdivided into mesencephalon (n-p) characterised by the cerebral aquaductus, pons (q-t) with on the dorsal side the cerebellum and finally the medulla oblongata (u-w).

DORSAL

anterior

RIGHT

LEFT

VENTRAL

posterior
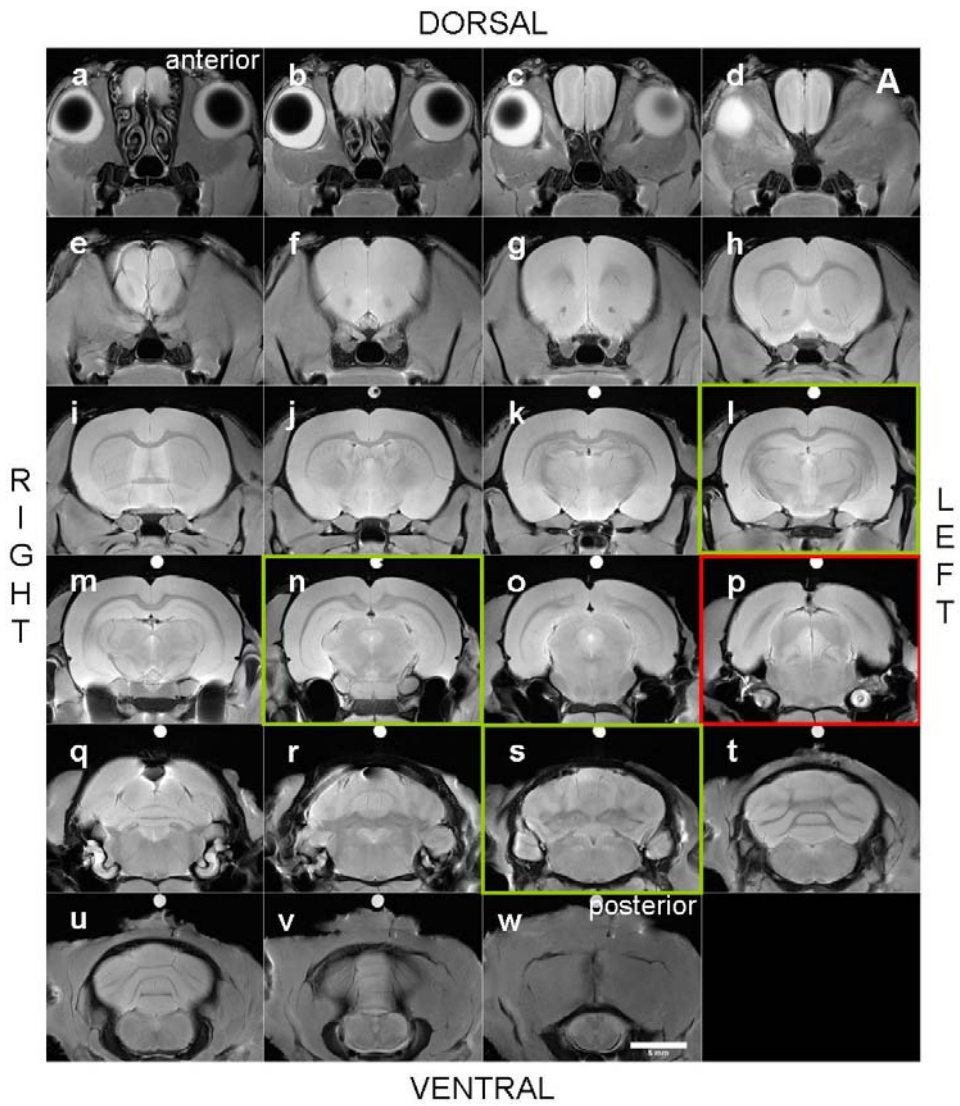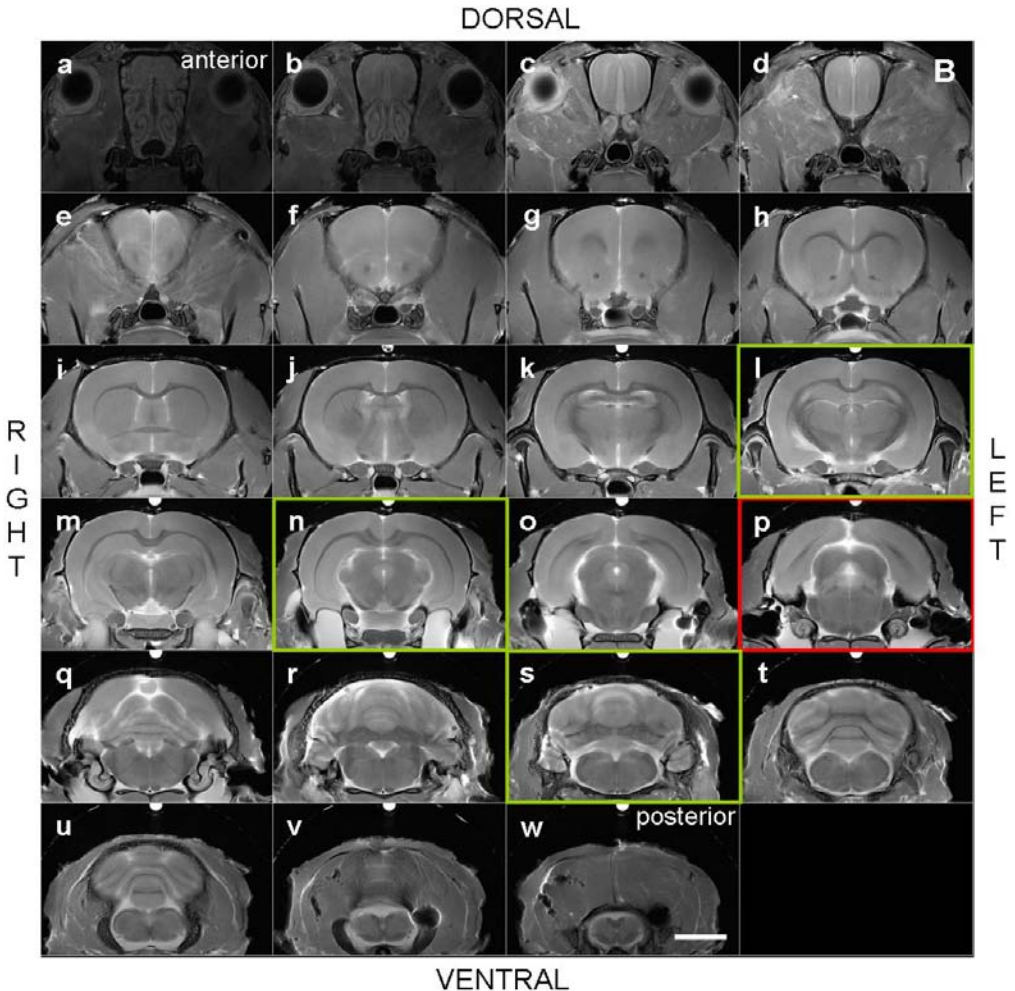
Figure 3.6: Coronal images of unfixed (A) and fixed (B) brain tissue acquired with a PD imaging sequence. The rat brain is shown as 1-mm thick consecutive slices in rostro-caudal direction. Image a till e depict the most frontral region where the olfactory bulbs are located between the eyes. From image e, the telecephalic cortex starts and finally covers the diecephalic and mesencephalic area. The diecephalic region extends from image j-m. The brain stem can be subdivided into mesencephalon (n-p), pons (q-t) and medulla (u-w). The cerebellum is positioned at the dorsal side of the brainstem as displayed in image r untill u. The tip of a water filled capillary, seen as a circular white spot above the brain, indicates the position of the bregma (k). Later in this chapter, the green bordered images are used to demonstrate the influence of tissue fixation while red bordered images are used to compare contrast modalities. Scale bar indicates 5 mm.

Horizontal imaging plane

PD imaging of the rat brain in dorso-ventral slice directions is shown on **figure 3.7** for unfixed (A) and fixed (B) tissue. The overview starts at the dorsal side with the telencephalic cortex and the olfactory bulbs (a-c). More downward, gray matter nuclei of the telecenphalon and diencephalon are depicted (d-g). The cerebellum is also visualized in these images. The brainstem area is depicted on image h to i. Image k shows the presence of three molars in the upper jaw (arrows).
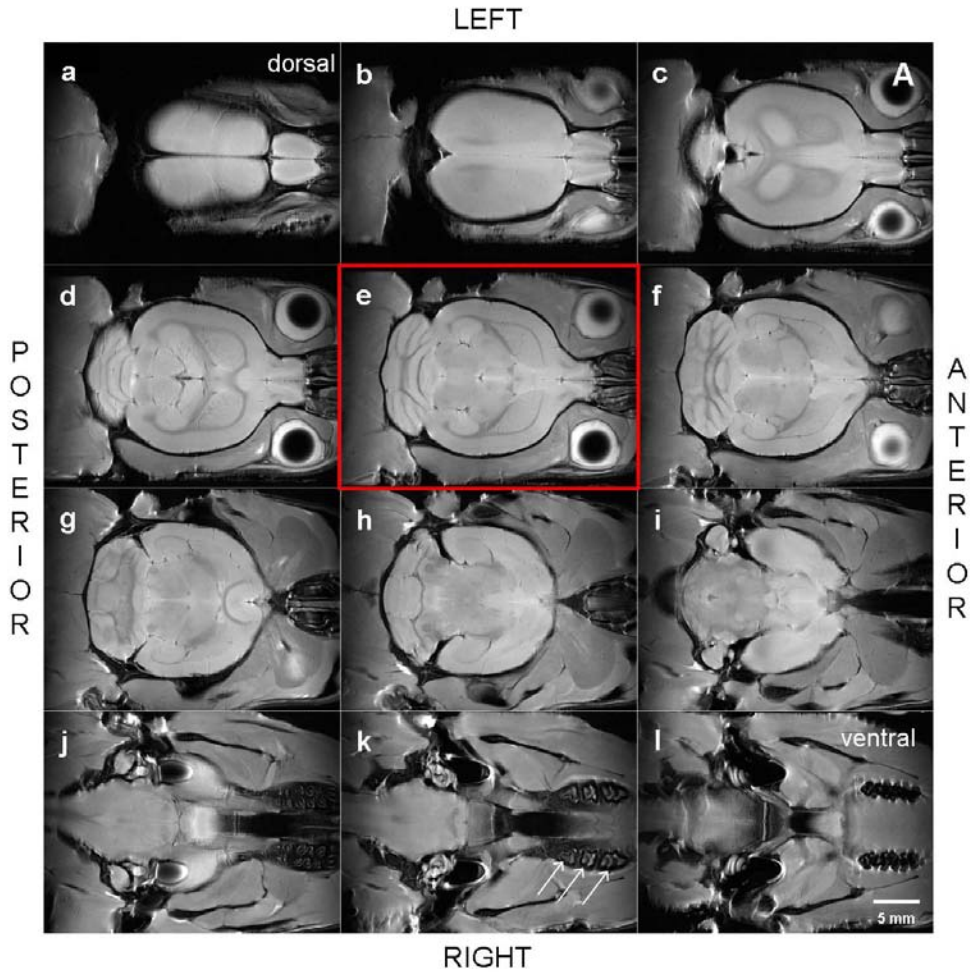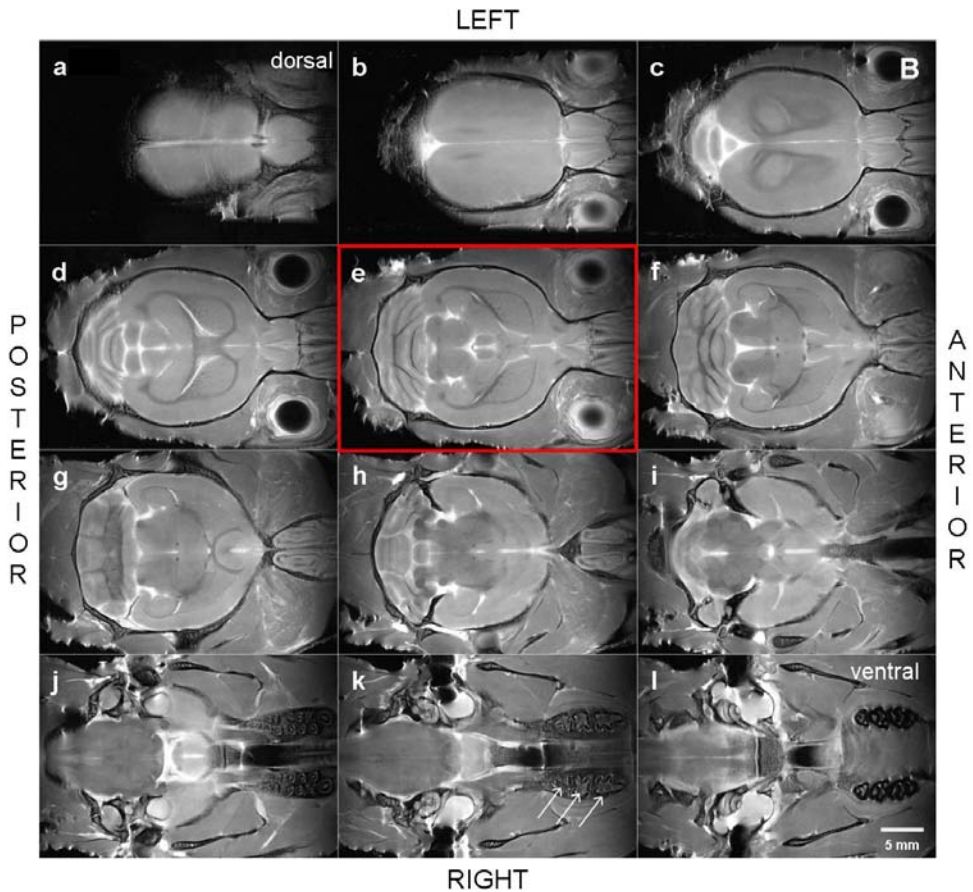
Figure 3.7: Overview of the horizontal imaging plane for unfixed (A) and fixed (B) brain tissue acquired with a PD imaging sequence. The rat brain is shown as 1-mm thick consecutive slices in dorso-ventral direction. Image a till b displays the telencephalic cortex and the olfactory bulbs. From image d until g, several gray matter structures of the telencephalon and diencephalon are seen as well as the cerebellum. The brainstem area is depicted on image h to i. Notice in image K the presence of three molars in the upper jaw (arrow). Red bordered images are used to compare contrast modalities further on in this chapter. Scale bar indicates 5 mm.

Sagittal imaging plane

In the overview of the sagittal imaging plane, the brain is depicted in a latero-medial sequence. Only one half of the brain is shown here. The 1-mm thick images are acquired with a PD imaging sequence for both the unfixed **(Fig. 3.7A)** and fixed **(Fig. 3.7 B)** brain tissue. At the mid-sagittal section (h) all the different brain parts are displayed. The following structures can be identified when looking in antero-posterior direction: the olfactory bulb, the telencephalic area, the diencephalic area and the brainstem with on dorsal side the cerebellum.
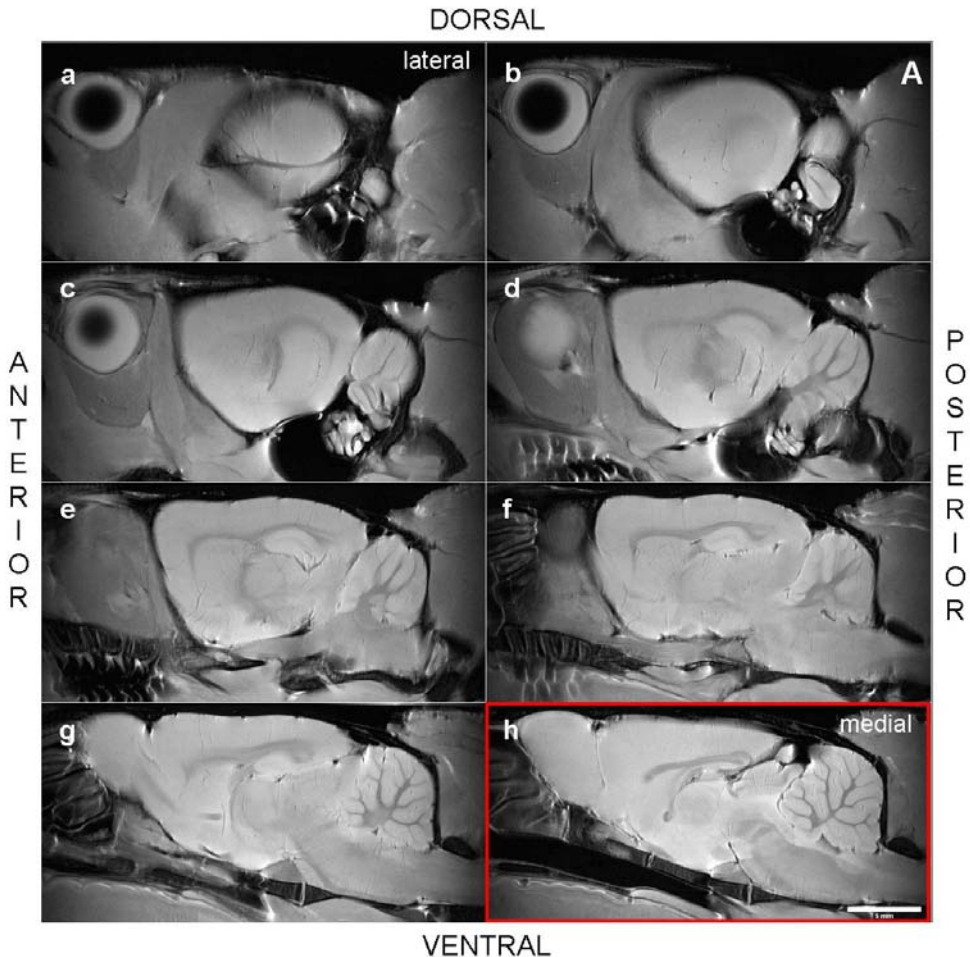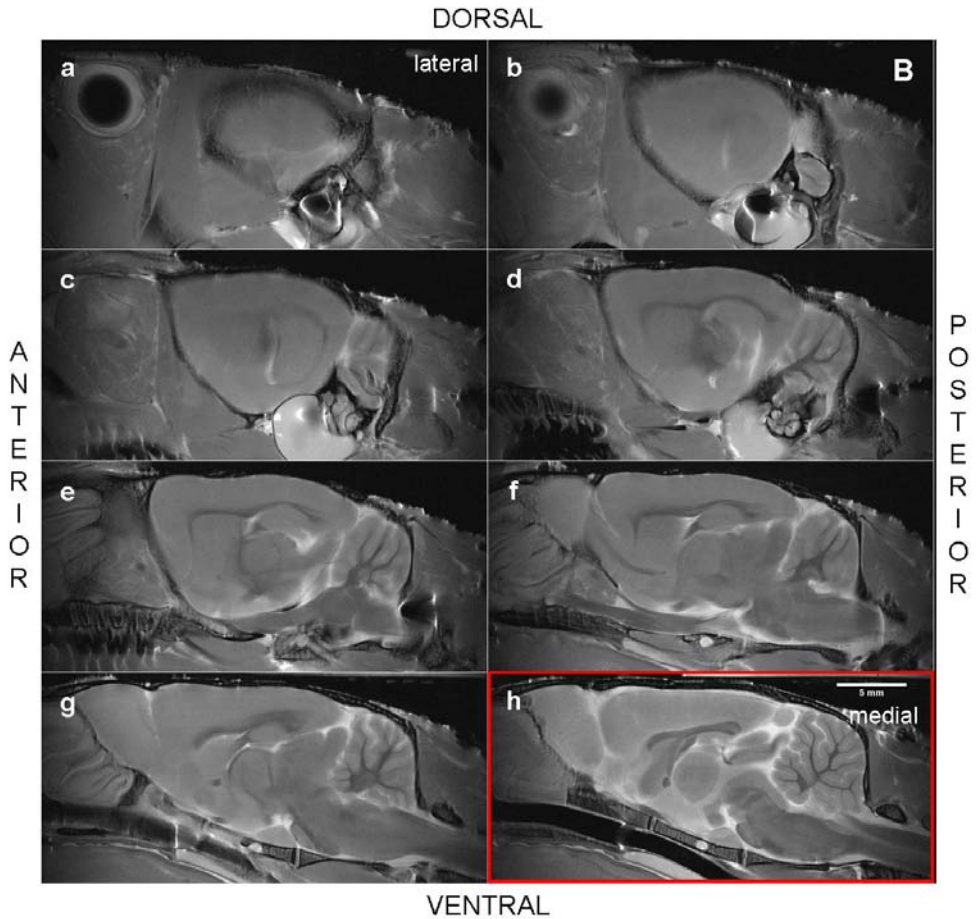
Figure 3.8: Overview of the sagittal imaging plane for unfixed (A) and fixed (B) brain tissue acquired with a PD imaging sequence. The rat brain is shown as 1-mm thick consecutive slices in latero-medial direction. Image h is taken at mid-sagittal level and depicts from left to right the following regions; the olfactory bulbs, telencephalic cortex, diecephalon and brainstem with on top of it the cerebellum. Red bordered images are used to compare contrast modalities further on in this chapter. Scale bar indicates 5 mm.

Influence of tissue fixation on image quality

Clearly, the main advantage of *in vivo* MRI is the possibility to follow up animals in time. Although some *in vivo* images will be shown in this thesis, the main focus lies on *ex vivo* imaging due to several advantages of the latter from a point of view of visualizing anatomical details (Benveniste and Blackband, 2002). First, longer scan times, up to 48 hours for unfixed cooled specimens, can be used while *in vivo* acquisitions are limited to 2 or 3 hours. This longer scan time results in a much better SNR. Secondly, *ex vivo* imaging does not suffer from motional artefacts resulting from pulsatile physical activity (breathing or cardiac activity). This lack of motion results in improved image quality. However, autolysis of unfixed tissue limits the scanning time to 48 hours even with additional cooling of the specimens at 4°C. Therefore the tissue can be fixed with a fixation fluid. It does not only offer the opportunity to increase even more the scan time, but the fixed specimen can also be preserved for years and scanned again at a later time point. Moreover, fixation of the tissue is advantageous when matching histology is required after the MRI. However, formaldehyde fixation prior the MRI, chemically changes the dynamic characteristics of tissues (i.e. shorter T2 due to a slower molecular mobility of mobile molecules in fixed specimens because of cross-links between Lys-residues of the proteins) thereby altering the contrast in the MR images compared to images of non-fixed tissue **(Fig. 3.9)**.
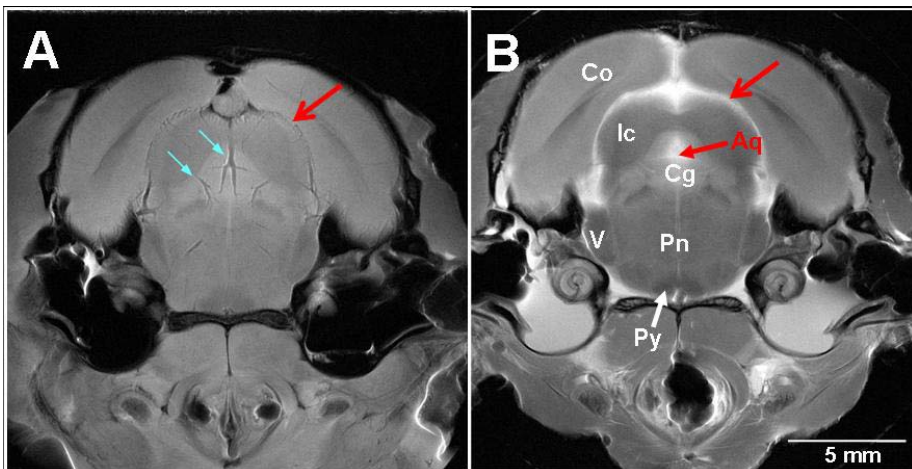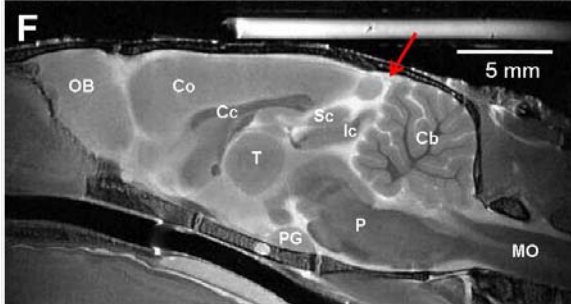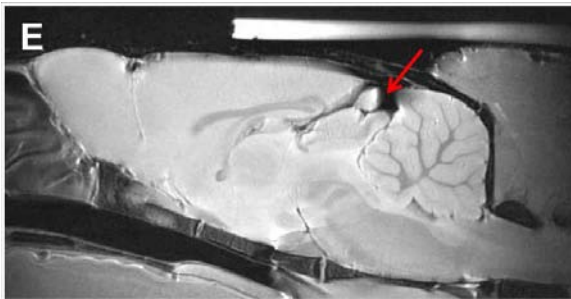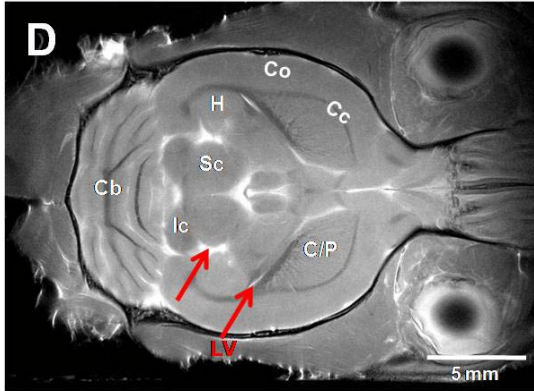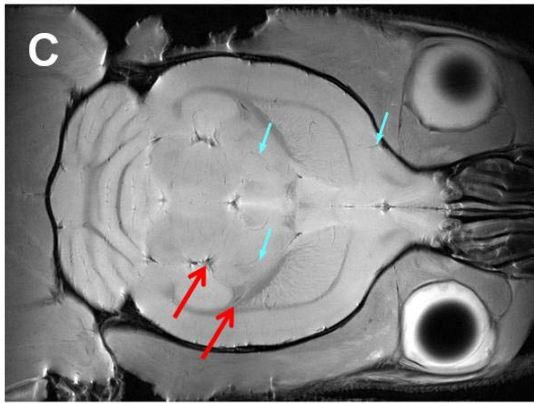
Figure 3.9: Tissue fixation alters image contrast. A coronal (A-B), horizontal (C-D) and sagittal (E-F) pair of images show contrast differences between non-fixed (A, C and E) and fixed (B, D and F) brain tissue on proton density images. (images correspond to the red bordered images of the overviews) The images of fixed tissue have in general a lower signal intensity (B, D and F) compared to unfixed images (A, C and E). A broad spectrum of gray intensities is displayed among gray matter structures simplifying their delineation; e.g. thalamus (T) and its surrounding gray matter tissue or regions within the pons (P). Subarachnoid spaces and ventricular cavities are filled with fixation fluid (red arrows) in fixed tissue and is seen as hyper-intense signals.

In non-fixed tissue images, blood vessels (blue arrows) can be detected. **Legend:** Aq cerebral aqueduct, Cb cerebellum, Cc corpus callosum, Cg central gray, Co cortex, C/P nucleus caudatus / putamen, H hippocampus, Ic inferior colliculus, LV lateral ventricle, MO medulla oblongata, OB olfactory bulb, P pons, Pn pontine nuclei, PG pituitary gland, Py pyramis, Sc superior colliculus, T thalamus, V trigeminal nerve root.

After tissue fixation, the overall signal intensity for both gray and white matter structures is lower **(Fig. 3.9 B, D and F)**. Nevertheless, gray matter structures are displayed with a broad range of gray shades making it easier to detect borders of gray matter structures in fixed specimens, e.g. thalamic nucleus or pons regions **(Fig. 3.9 F)**. Subarachnoidal spaces and ventricular cavities have a hyper-intense signal intensity on fixed images because they are filled with fixation fluids (red arrows). In non-fixed tissue, it is possible to detect blood vessels due to blood clothing. The iron of the blood causes susceptibility artefacts which results in hypo-intense signals. Thus, tissue fixation results in an improved contrast between brain structures thereby increasing the understanding of the complex architecture of the small rat brain.

PD- versus T2-weighted imaging sequences

Another way to improve structure delineation in the rat brain, can be achieved by combining MR-images obtained with different imaging sequences, i.e proton density and T2-weighting. Each sequence elicits a different kind of contrast resulting from tissue specific characteristics, i.e. amount of detectable mobile protons and relaxation time values.

On PD-images **(Fig. 3.10 A, C and E)** which reflect the local proton density in the tissue, white matter structure such as the corpus callosum or the inner white matter of the cerebellum show darker appearance as compared to gray matter structures such as the cortex. The gray matter of the brain has a normo-intense gray shade, but subtle differences in this gray shade can be detected. As seen in **figure 3.10 A**, the thalamic nuclei have a more hypo-intense gray shade than the hippocampal area. T2-weighted images **(Fig. 3.10 B, D and F)** provide information about the molecular mobility of the mobile molecules in the tissue. In tissues with a dense organisation, molecules will have a lower mobility and therefore their MR-signal will decay faster than in less dense organised tissue. White matter or regions containing fiber tracts, such as the pyramis, capsula interna or cerebral peduncle, are classified as densly organised tissue and have a lower proton concentration. Therefore they are depicted as darker signals on T2-weighted images compared to PD weighted images. Also here, the gray matter tissue has a normo-intense signal intensity with subtle deviating gray shades corresponding to different anatomical structures i.e. hippocampal area and thalamic nuclei. Therefore, heavily T2-weighted images may offer a better contrast between gray and white matter structures, but require more scanning time to maintain a similar SNR as PD images.

PD-weighted **T2-weighted**
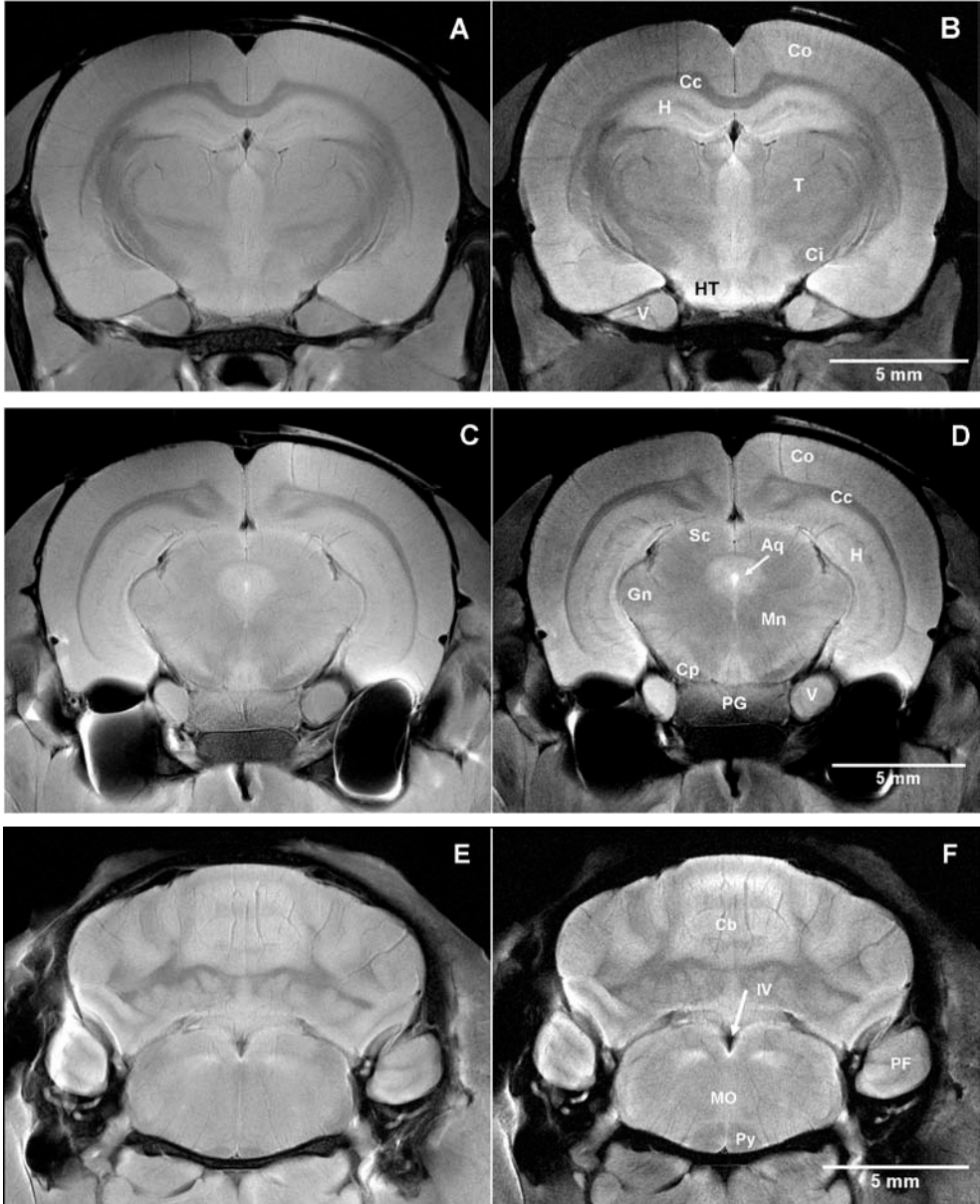
Figure 3.10: T2-weighting improves contrast between gray and white matter structures. Coronal 1-mm thick images of unfixed brain tissue, acquired with a PD (A, C and E) or T2-weighted (B, D and F) imaging sequence, are obtained with similar SNR and resolutions. T2-weighted images visualize white matter structures (corpus callosum, pyramis, cerebral peduncle) as strong hypo-intense signals, which enhances the contrast difference with gray matter structures (thalamic nuclei, hippocampal area, medulla ablongata). Legend: Aq cerebral aqueduct, Cc corpus callosum, Ci capsula interna, Cp cerebral peduncle, Co cortex, Gn geniculate nuclei, H hippocampal area, HT hypothalamus, Mn mesencephalic nuclei, MO medulla oblongata, PF paraflocculus, PG pituitary gland, Py pyramis, Sc colliculus superior, T thalamus, V trigeminal nerve root, IV fourth ventricle.

Brain structures such as the hippocampal area and the pituitary gland show more morphological details when visualized on T2-weighted images. The rodent hippocampal formation is extensively studied and its anatomical organization is well known from histological stained sections (Benveniste et al., 2000). It is generally accepted that the entire hippocampal formation includes the hippocampus proper, the dentate gyrus, the subicular complex and the entorhinal cortex. The hippocampus proper and the dentate gyrus can be defined on PD and T2-weighted images **(Fig. 3.11)**. T2-weighted images of the hippocampus proper seem to have a slightly better contrast compared to proton density images. Within the hippocampal area on T2-weighted images, it is possible to identify the hippocampal fissure as a dark band. A small hyper-intense V-shaped line is seen, which probably can be ascribed to the granular layer of the dentate gyrus. Other subregions of the hippocampus proper could not be defined even at this high spatial resolution and good SNR.

Morphological analysis of the pituitary gland also benefits from T2-weighting. The improved visualization of the pituitary gland lobes using a T2-weighted imaging sequence is discussed in detail **in chapter 4**. In short, the three separate lobes of the pituitary gland can be visualized on coronal and mid-sagittal MR images based on T2-value related contrast differences **(Fig. 3.12)**. T2-imaging shows the posterior and anterior lobe as dark hypo-intense areas and are clearly separated by a very hyper-intense intermediate lobe. On PD images, it is also possible to distinguish the different lobes, but the contrast differences are much weaker.
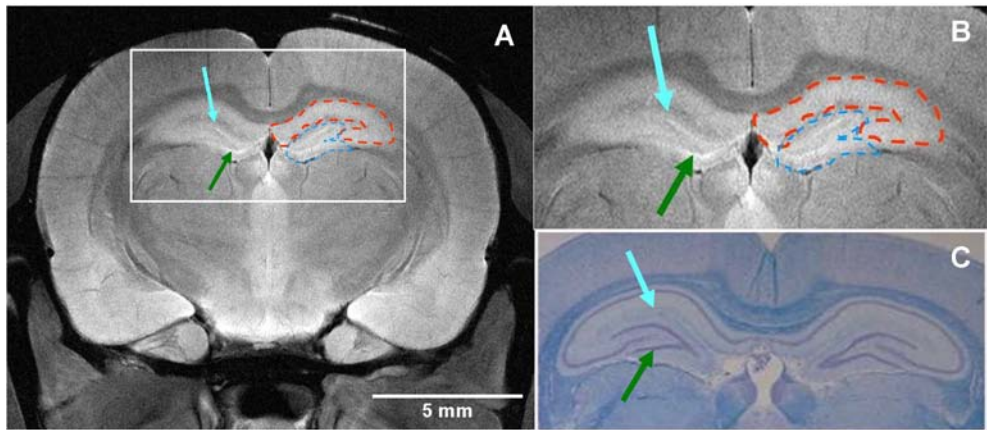
Figure 3.11: T2-weighted imaging shows subregions of the hippocampal area (unfixed tissue). The hippocampal proper (red dotted line) and the dendate gyrus (blue dotted line) can be distinguished on the high resolution MR image (A-B). The hippocampal fissure (blue arrow) is shown as a hypo-intense line. Within the dentate gyrus, a hyper-intense V-shaped line can be seen which probably correlates to the granular cell layer (see magnified image B). A matching histologic section (KB staining) shows the granular cell layer of the dentate gyrus (green arrow) and the hippocampal fissure (blue arrow).
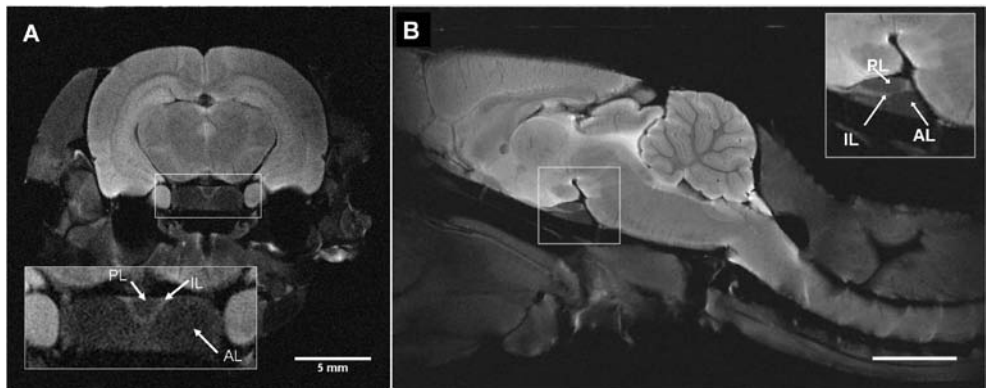
Figure 3.12: T2-weighted imaging shows detailed pituitary gland morphology (unfixed tissue). Both in coronal and sagittal slice direction, the three separate lobes of the pituitary gland can be visualized. The posterior (PL) and anterior lobe (AL) have a dark hypo-intense signal intensity and are separated from each other by the hyper-intense intermediate lobe (IL). Scale bar indicates 5 mm.

Matching histologic sections and annotation figures

The complete set of reference frame images is matched with histological sections to demonstrate the micro-anatomical level which can be obtained with the high resolution imaging MRI technique **(Fig. 3.13 - 3.14)**. The MR images in different imaging planes correspond very well with histology. The histologic sections are stained with Klüver-Barrera because it is well suited to determine white and gray matter structures in nervous tissue. It stains myelinated structures, known as white matter, intensive blue while cell nuclei, classified as gray matter, have a purple colour. To provide even more information, the reference frame can be supplemented with annotation figures. Contrast borders between anatomical structures in the rat brain, shown on the MR images and histology, can be drawn and annotated **(Fig. 3.13 – 3.14 C)**.
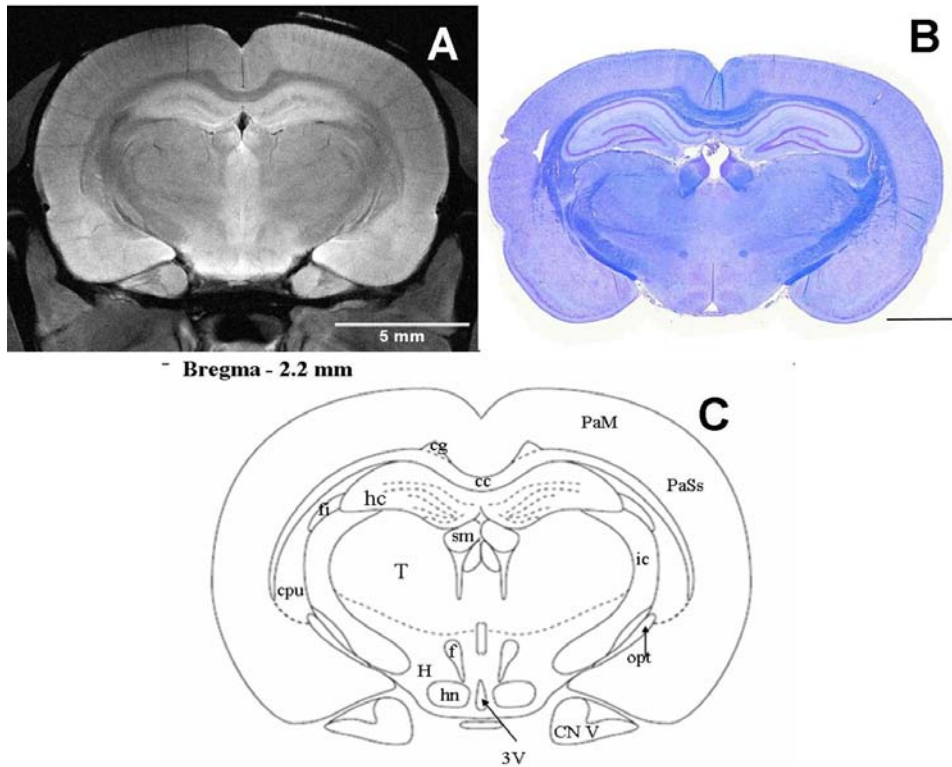
Figure 3.13: Matching histologic section and annotation figure of a coronal T2 weighted image (A) of unfixed brain tissue taken 2.2 mm behind the bregma. This image is matched with a Klüver-Barrera histological section (B). Annotation image C: cc corpus callosum, cg cingulum, cpu caudatus putamen, CN V trigeminal nerve, fi fimbriae hippocampi, f fornix, H hypothalamus, hc hippocampus, hn hypothalamic nucleus, ic internal capsule, PaM parietal cortex moteor area, PaSs parietal cortex somatosensory area, sm stria medullaris thalamus, T thalamus and 3 V third ventricle.
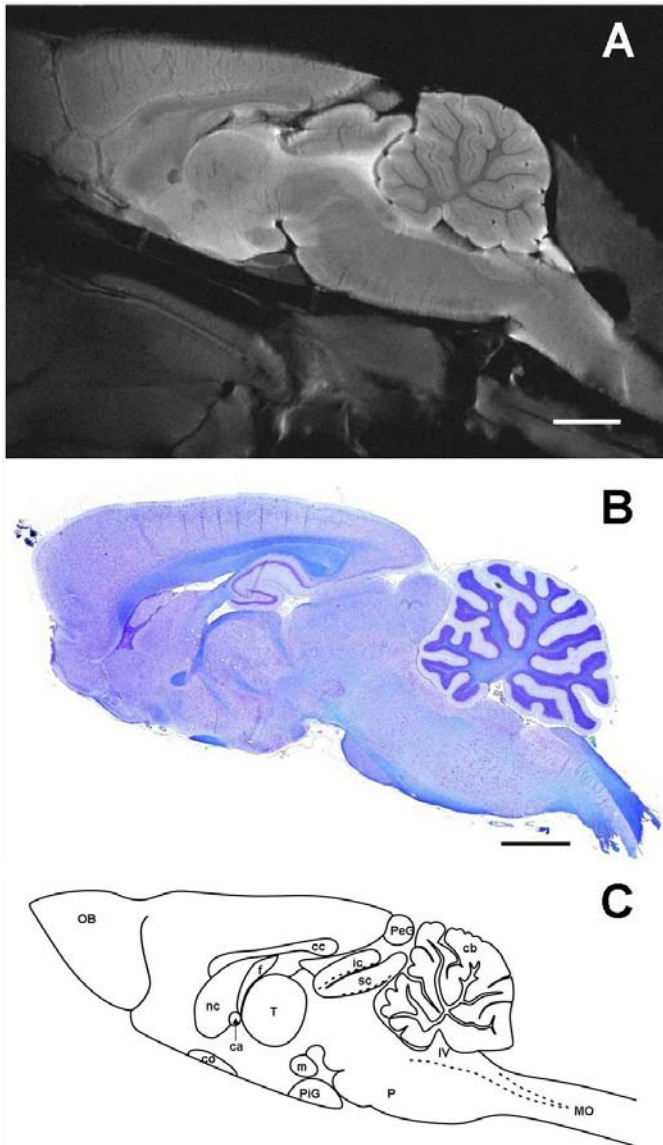
Figure 3.14: T2-weighted MR image (A) taken at mid-sagittal position of an unfixed rat brain showing the white matter as dark signal intensties and gray matter as more heterogenous gray shades. A histologic matching section stained with Klüwer-Barrera (B) shows white matter structures as dark blue. Annotation image (C): ca anterior commissure, cc corpus callosum, cb cerebellum, co chiasma opticum, f fornix, ic inferior colliculus, nc nucleus caudatus, m corpus mammilare, MO medulla oblongata, P pons, PeG pineal gland, Pig pituitary gland, sc superior colliculus, T thalamus, IV fourth ventricle and OB olfactory bulb.

SPINAL CORD TISSUE

The spinal cord was imaged within the vertebral column to overcome accidental damaging during tissue isolation. The vertebras further provide a supportive matrix to decrease the risk of tissue deformation and offer information about the vertebral and segmental spinal cord level. Obtaining consecutive 1-mm-thick MR slices allows the visualization of consecutive vertebras separated by their intervertebral disc. **Figure 3.15** shows consecutive images of vertebra L1 (c-h) and the superior and inferior located parts of vertebra T13 (a-b) and L2 (i), respectively. The intervertebral discs are interposed between the consecutive vertebras (b and g). The detailed morphology of the vertebra is clearly visible on these high resolution MR images, i.e. vertebral body, spinous process, transverse process and the lamina. It is even possible to localise the intervertebral foramen where the spinal nerves exit the spinal canal (b and g).

As in humans, there is a differential growth between the spinal cord tissue and the vertebral column. The segments of the spinal cord lie higher than the corresponding vertebrae as a result of this disproportional growth. This must be taken in account when inducing spinal cord lesions, because a lesion induced at vertebral level T13, will cause damage in lumbar spinal segments. In rat, the spinal cord terminates at the level of the intervertebral disc between L3 and L4 (Gelderd and Chopin, 1977). From that level on, only ventral and dorsal nerve roots descend within the spinal canal until they exit towards the periphery, i.e. cauda equina. A list of the vertebral levels and their corresponding spinal segments is shown in **table 3.1** (Addapted from Gelderd and Chopin, 1977). The spinal cord tissue itself is located within the spinal canal. It consists of an inner core of gray matter **(Fig. 3.15)**, which is surrounded by white matter fibers Notice also the presence of spinal nerve roots at this L1 vertebral level.
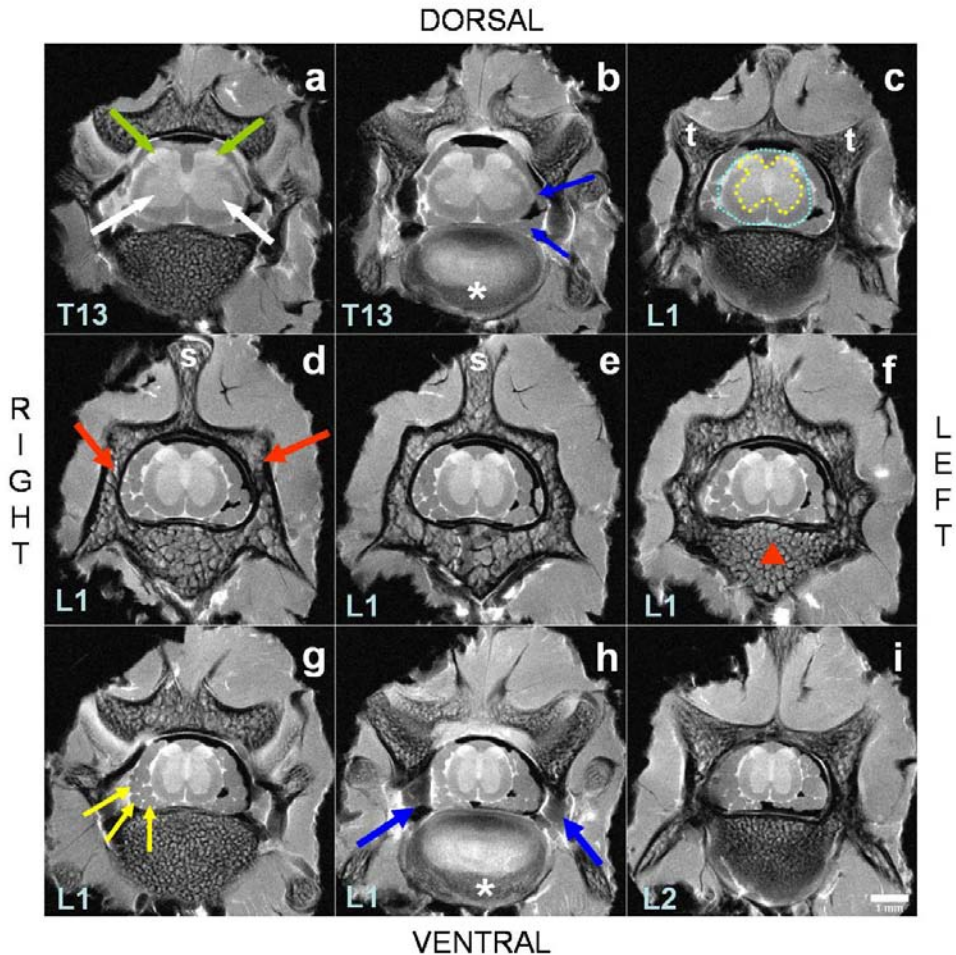
Figure 3.15: High resolution PD MRI shows detailed morphology of the fixed spinal cord and vertebras as 1-mm-thick consecutive coronal sections. The parts of the vertebra; spinous process (s), transverse process (t), vertebral body (red ▲), lamina (red arrow). Vertebral discs (*) are interposed between consecutive vertebras. The intervertebral foramen (blue arrow) shows spinal nerves which exit the spinal canal. The spinal cord tissue in the vertebral canal consists of a butterfly shaped gray matter (yellow dotted line) and surrounding white matter (blue dotted line). The gray matter can be subdivided into a dorsal and ventral horn (green and white arrow respectively). At the lower vertebral levels (d-i) dorsal and ventral roots (yellow arrow) can be seen. Scale bar indicates 1 mm.

Vertebral number	Spinal segment	Vertebral number	Spinal segment
C1	C1	T5	T6
C2	C2-C3	T6	T7
C3	C3-C4	T7	T8
C4	C5	T8	T9
C5	C6	T9	T10
C6	C7-C8	T10	T11
C7	C8-T1	T11	T12-T13
T1	T1-T2	T12	T13-L1-L2
T2	T3	T13	L3
T3	T4	L1	L4-L5-L6-S1
T4	T5	L2	S1-S2-S3-S4

Table 3.1: Spinal cord segments lie more rostral than the vertebral level where they exit the spinal canal. This difference is due to a disproportional growth between spinal cord and the vertebral column. This has to be taken into account when lesions need to be induced at a specific cord segment.

Coronal imaging plane

An overview of coronal (axial) sections of the spinal cord is shown in **figure 3.16 A and B**. Fixed spinal cord tissue is imaged in rostro-caudal direction as 1-mm consecutive slices with a PD-weighted sequence. In the overview, the complete spinal cord is depicted with an inter-slice gap of 2 to 3 mm. Coronal images show the oval shaped cross-section of the spinal cord enclosed in its vertebra. Within this tissue, gray and white matter could be distinguished based on signal intensities. The butterfly-shaped gray matter has a hyper-intense signal intensity compared to the surrounding white matter tracts.

Figure 3.16: Coronal overview of the fixed rat spinal cord, imaged with a PD-weighted sequence. 3.16 A shows vertebral level C1 until T11 and 3.16 B shows level T11-S4. The complete spinal cord is depicted with an inter-slice gap of 2 to 3 mm. In the left bottom corner of each image, the vertebral number is displayed. Gray matter of the spinal cord is seen as a hyper-intense butterfly-shaped structure, while the surrounding white matter fibers are hypo-intense. The shape of the gray matter varies throughout the total spinal cord length because the amount of neurons differ between different spinal cord segments. Legend: C cervical, T thoracic, L lumbar and S sacral. Scale bar indicates 1 mm.

DORSAL

VENTRAL
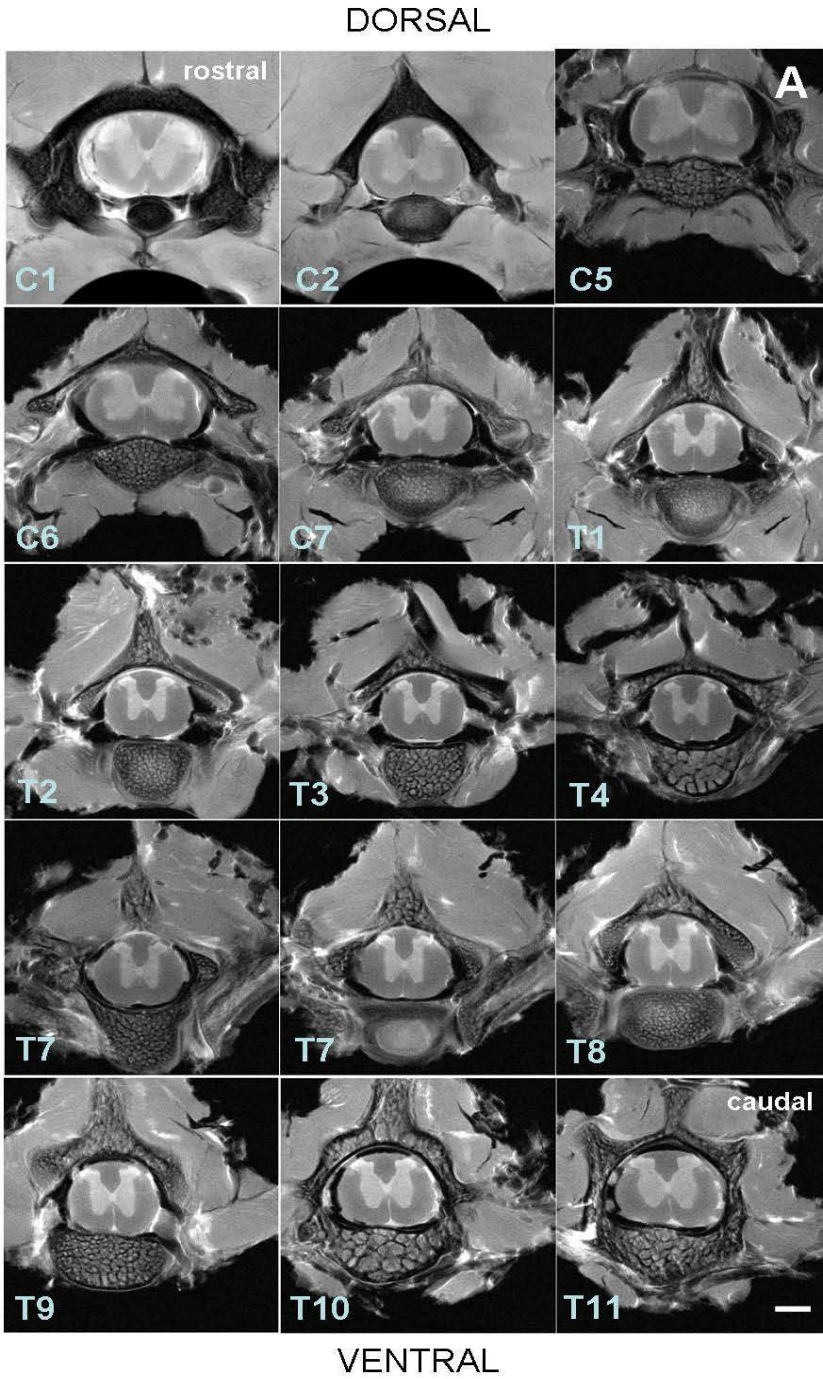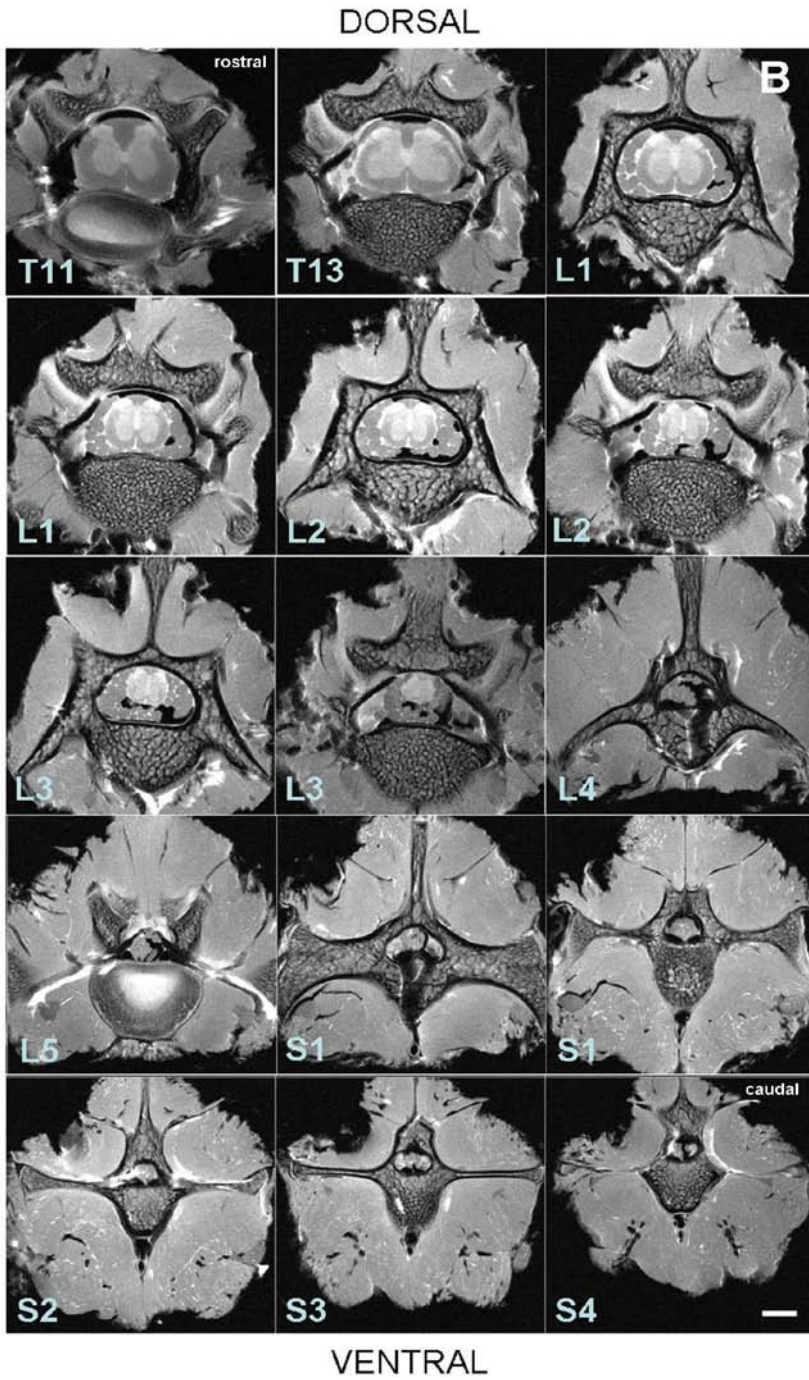
Based on the characteristic shape of the gray matter, but also on the relative amount of white matter, anatomical regions of the spinal cord could be determined i.e. cervical, thoracic, lumbar and sacral segmental levels which are represented by **figures 3.16 C6, T7, T13 and L3**, respectively. Morphometric analysis **(Fig. 3.17)** of these different segmental regions shows that the total surface area of the spinal cord varies throughout its length because of the variations in the number of neurons and white matter axons. There are two enlargements over the total spinal cord length as indicated by the total area. There is one enlargement at cervical and another at lumbar level, which are caused by the number of neurons that give rise to the brachial and lumbosacral plexus, respectively. The amount of white matter decreases in rostro-caudal direction because descending motor fibers leave the tract at successive lower levels, while ascending fibers join the sensory tracts at each higher level.

	cervical	thoracic	lumbar	sacral
total area	7,16	4,61	6,48	3,12
white matter	3,95	3,24	3,19	1,47
gray matter	2,93	1,23	2,90	1,64
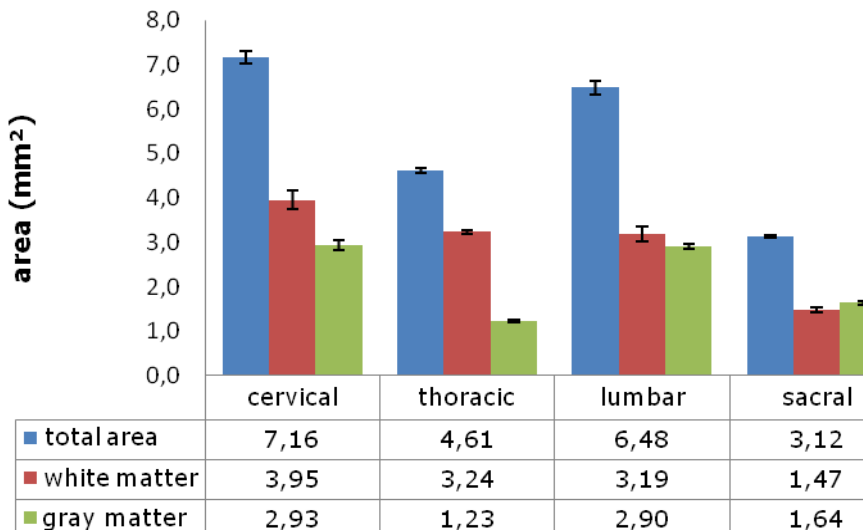
Figure 3.17: Morphometric analysis of axial spinal cord sections at different segmental levels. The total coronal area as well as the amount of white and gray matter are determined in mm² for cervical, thoracic, lumbar and sacral spinal segments (as determined by table 3.1). The total axial surface area varies throughout the length of the spinal cord resulting from the amount of gray and white matter tissue at each level. The white matter compartment decreases in caudal direction, while the gray matter area also shows fluctuations. Cervical and lumbar segments contain a higher amount of gray matter compared to thoracic and sacral levels.

Horizontal imaging plane

An overview of horizontal MR images of the fixed spinal cord is shown in **figure 3.18**. High resolution PD-weighted images are acquired in ventro-dorsal direction. The overview starts with images at the ventral side of the vertebral column. It shows the vertebral body and the intervertebral discs. Image c shows the ventral white matter of the spinal cord. The next slice is taken at the level of the ventral gray matter horns. It is pictured as an alternating pattern of white and gray matter bands. Image e depicts the level at the central canal. In the following images f-g, the dorsal horn of the gray matter is visible. With regard to the anatomical curves of the backbone, it is difficult to interpret horizontal images, if they are not shown as consecutive images.

Figure 3.18: High resolution PD-weighted horizontal images of fixed spinal cord tissue, taken at the cervical level. The images are obtained in a ventro-dorsal slice direction. Legend: vertebral body (*, intervertebral disc (yellow arrow), white matter (blue arrow) and gray matter (green arrow), the spinous process (white arrow). A coronal section of the cervical spinal cord indicating the levels corresponding to the horizontal sections is shown at the right bottom of the page.

CERVICAL

RIHGT

LEFT

THORACIC
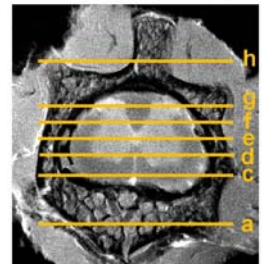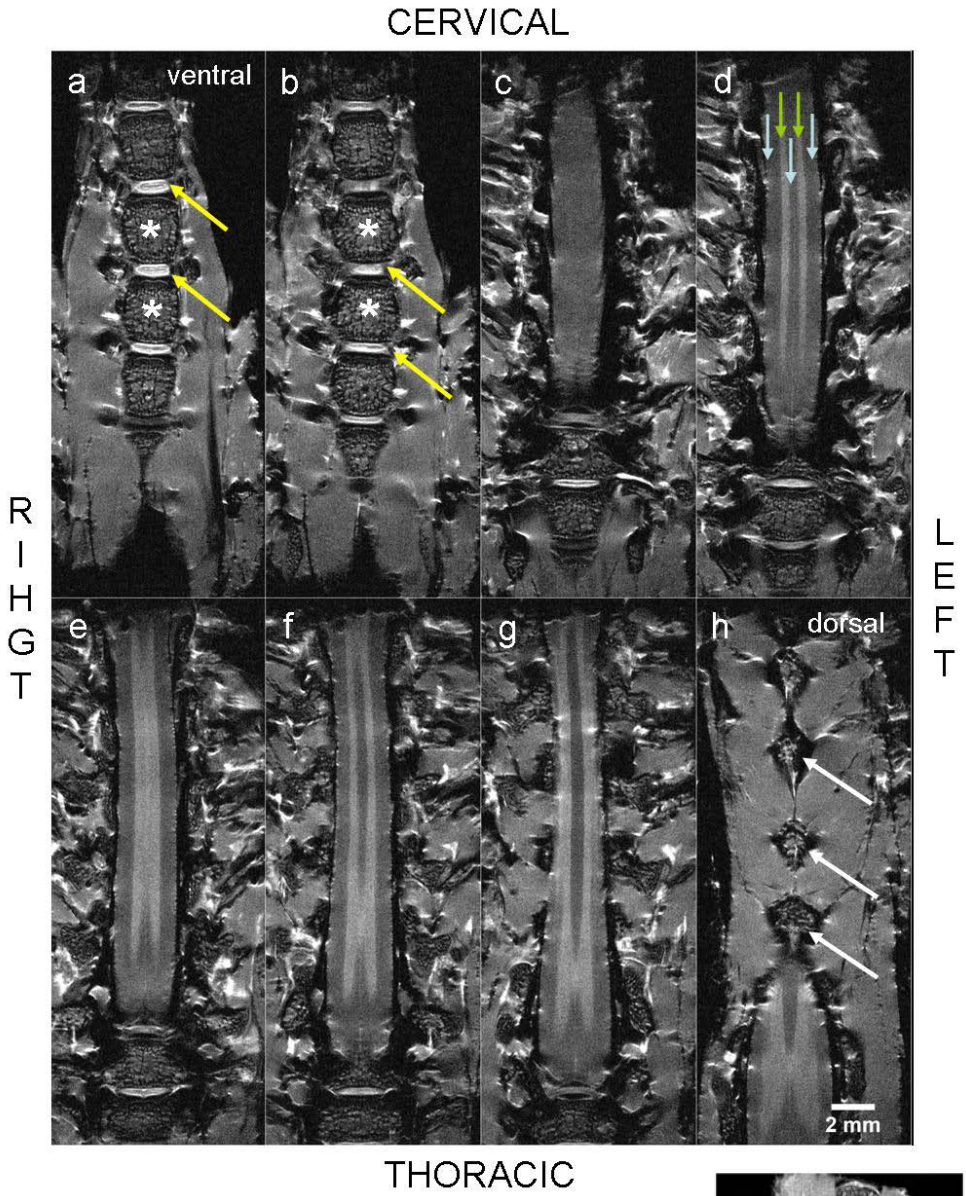
Sagittal imaging plane

The sagittal sections of the fixed spinal cord **(Fig. 3.19)** are acquired with a PD-weighted sequence and are characterized by the presence of the vertebral bodies separated by the intervertebral discs at the ventral side. Latero-lateral slices of the spinal cord tissue (from left side to right side or *vice versa)*, show first a broad band of hypo-intense white matter tissue (c). Image d contains a small ventral strip of hypo-intense white matter and a broad band of hyper-intense gray matter tissue. This broad band of gray matter corresponds to a section through the dorsal and ventral horn. At the mid-sagittal section (e), there is a very small band of gray matter surrounded by white mater. Spinal nerves, which exit the spinal canal are visualized in image a and h (red arrows). Due to curvatures of the vertebral column, it is difficult to image the complete spinal cord over a long distance in a longitudinal (sagittal or horizontal) plane. Therefore it is necessary to combine consecutive sagittal or horizontal images to interpret the morphology of the spinal cord.

Figure 3.19: Overview of PD-weighted sagittal sections of fixed spinal cord tissue within its anatomical matrix. The overview is created with an interslice gap of 1 mm. Legend: vertebral body (*), intervertebral discs (yellow arrows), spinous process (red circle), the lamina (white arrow), white matter (w), gray matter (green arrows) and spinal nerves (red arrows). A coronal section of the cervical spinal cord indicating the levels corresponding to the sagittal sections is shown at the right bottom of the page.
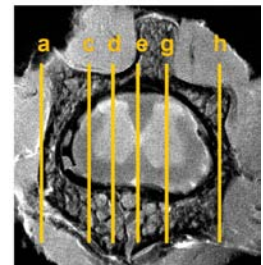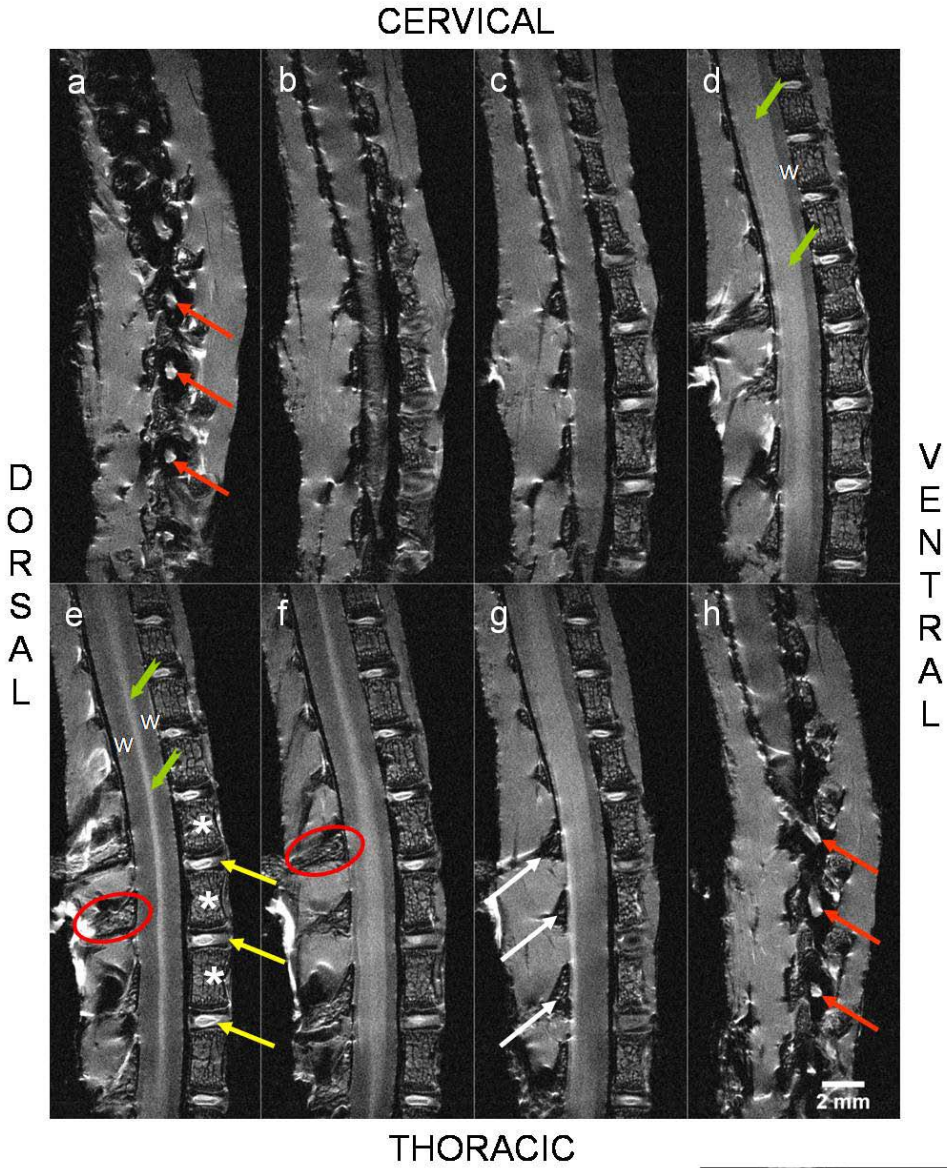
Influence of tissue fixation

Imaging of the spinal cord of fixed specimens results in an improved contrast difference between white and gray matter structures compared to non-fixed tissue **(Fig. 3.20)**. Using a PD-weighted imaging sequence, signal intensities for gray and white matter of fixed tissue are similar to these of the rat brain, i.e. white matter structures are hypo-intense while the gray matter is hyper-intense.
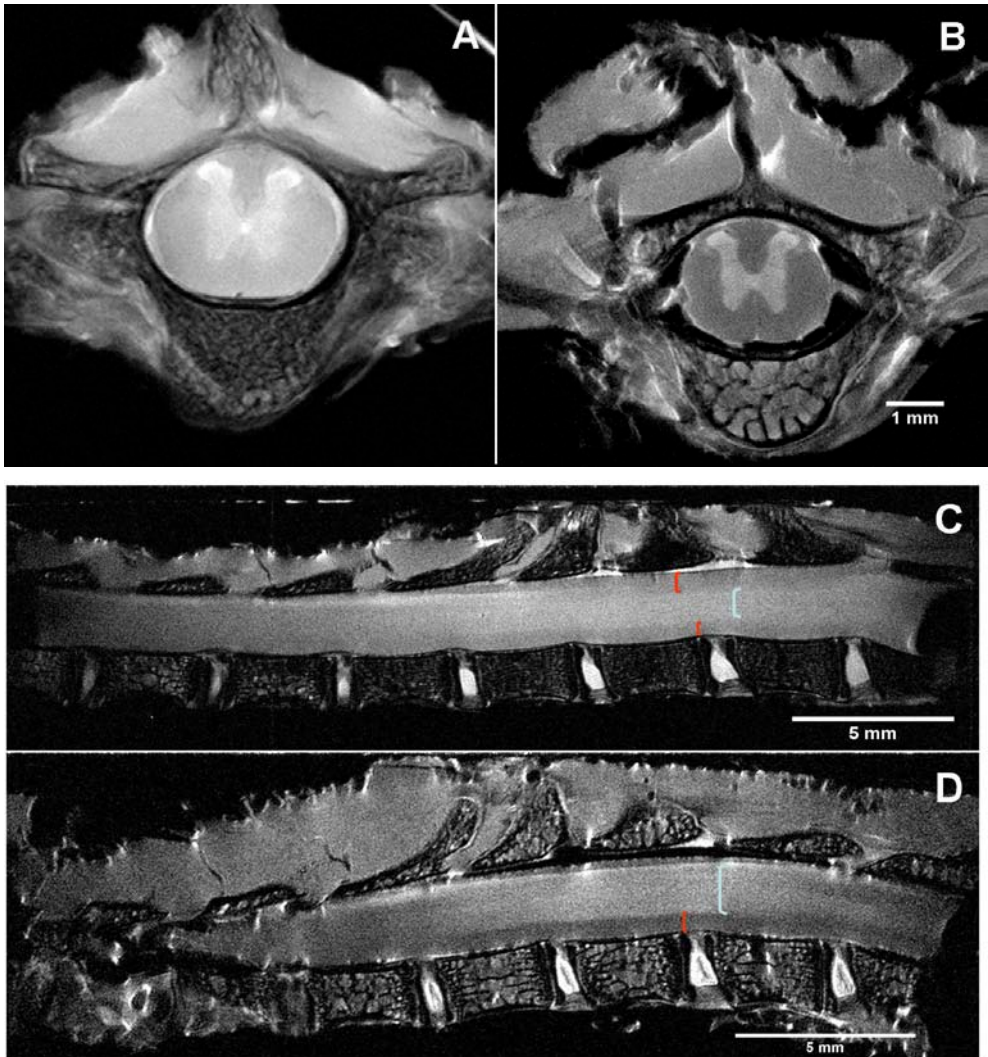
Figure 3.20: Fixation of the spinal cord alters contrast between gray and white matter. A coronal (A-B) and sagittal (C-D) pair of images show contrast differences between non-fixed (A and C) and fixed (B and D) spinal cord tissue on PD weighted images. On coronal images, the characteristic gray matter shape is hyper-intense compared to the surrounding white matter for both unfixed and fixed tissue, although after fixation the contrast difference between gray and white matter seems to be improved (B). This enhanced contrast difference is also shown on the sagittal image (D), where ventral white matter (red bracket) is hypo-intense compared to the gray matter (blue bracket).

3.4 Conclusions

This reference set of images of the rat's CNS shows that *ex vivo* high resolution MRI offers the opportunity to yield detailed morphological information of small specimens such as the rat brain and spinal cord. Major brain regions, such as the hippocampal area, cerebellum or brain stem, can be easily characterised, although detailed analysis of some very minute subregions require resolution beyond this high in-plane resolution of 40 x 40 μm. Although the spinal cord has extremely small dimensions, many anatomical details could be seen on the high resolution images. Also the different segmental cord levels can be easily distinguished. These detailed images further offer the possibility to perform morphometric measurements. MR imaging of the brain and spinal cord in the three orthogonal slice directions contributes to the spatial understanding of the central nervous system of the rat.

Nowadays, *ex vivo* MR-images still have a better quality than *in vivo* images because of the longer scan times and the absence of motion-artefacts (Franconi et al., 2000). However, *post-mortem* tissue will suffer from autolysis which limits the scan time to 24 - 48 hours, even at 4°C. Therefore it might be interesting to fix the tissue before imaging. Fixation rules out the limitations of *post-mortem* imaging as previously mentioned but it also induces chemical changes in the tissue characteristics which may lead to tissue shrinkage and altered T2-values. Tissue fixation results in improved contrast between gray and white matter structures, but the degree of contrast between the neuro-antomical

structures also depends on the acquisition parameters that are applied. T2-weighted images of fixed and unfixed specimens also show increased contrast difference between gray and white structures compared to PD-weighted images. The combination of MR images, acquired with different imaging sequences, thus further completes the morphological information.

Dependent on the anatomical structures one wants to highlight in the image, an optimal set of acquisition parameters for TR and TE must be selected. The TR-value of 2500 ms and the TE values of 18 and 55 ms used in this chapter for PD- and T2-imaging of unfixed CNS tissue respectively resulted in qualitative images with maximal overall (anatomical) structure delineation. Therefore, these values provide a good guideline, but needs to be further optimized when focussing on a specific anatomical structure as will be shown in chapter 4 and 6. The same holds for the TE-value of 35 ms used to obtain T2-weighted images of fixed CNS. Also this TE-value has to be seen as the optimal value for 'good overall contrast' but fine-tuning for a specific detail might be worthwhile.

The parameters selected for imaging of non-fixed tissue in this chapter are suited starting values for performing *in vivo* imaging of rodents. Although *in vivo* imaging is restricted in acquisition time, it provides the advantage to follow-up the same animal in time. This serial follow-up is highly important to evaluate new therapeutic interventions or to analyse the sequential steps of a process. The time limitation for *in vivo* imaging also implies less resolution and diminished SNR compared to *ex vivo* imaging. However *in vivo* image quality will for sure strongly improve by synchronizing the acquisition sequence to the heart-lung movements to eliminate motion artefacts and upon going to higher magnetic field strengths. An illustration of the excellent image quality of high field (9.4T) *in vivo* MRI will be presented in chapter 4.

Thus in conclusion, this MRI-based reference frame offers a well established data set which can be used to detect structural abnormalities or changes in signal intensities related to pathological conditions.

References

Aoki I, Wu YJ, Silva AC, Lynch RM, Koretsky AP. 2004. In vivo detection of neuroarchitecture in the rodent brain using manganese-enhanced MRI. NeuroImage 22(3):1046-1059.

Bear M, Conners B, Paradiso M. 2007. Neuroscience: exploring the brain.3rd edition. Philadephia: Lippencott Williams and Wilkins.

Benveniste H, Blackband S. 2002. MR microscopy and high resolution small animal MRI: applications in neuroscience research. Progress in neurobiology 67(5):393-420.

Benveniste H, Blackband SJ. 2006. Translational neuroscience and magnetic-resonance microscopy. Lancet neurology 5(6):536-544.

Benveniste H, Kim K, Zhang L, Johnson GA. 2000. Magnetic resonance microscopy of the C57BL mouse brain. NeuroImage 11(6 Pt 1):601-611.

Brockmann MA, Kemmling A, Groden C. 2007. Current issues and perspectives in small rodent magnetic resonance imaging using clinical MRI scanners. Methods 43(1):79-87.

Franconi F, Lemaire L, Marescaux L, Jallet P, Le Jeune JJ. 2000. In vivo quantitative microimaging of rat spinal cord at 7T. Magnetic resonance in medicin 44(6):893-898.

Gelderd JB, Chopin SF. 1977. Vertebral level of origin of spinal nerves in rat. Anatomical record 188(1):45-47.

Johnson GA, Benveniste H, Engelhardt RT, Qiu H, Hedlund LW. 1997. Magnetic resonance microscopy in basic studies of brain structure and function. Annals of the New York Academy of Sciences 820:139-147.

Paxinos G, Watson C. 2007. The rat brain in stereotaxic coordinates.6th edition. San Diego, California: Academic Press.

Pellegrino L, Pellegrino A, Cushman A. 1979. A stereotaxic atlas of the rat brain. New York: Plenum.

Rasband W. 1997-2008. Image J, U.S. National Institutes of Health. .Bethesda, Maryland, USA, http://rsb.info.nih.gov/ij/.

Swanson L. 2003. Brain maps: structure of the rat brain.3th edition. New York: Elsevier.

Takahashi M, Uematsu H, Hatabu H. 2003. MR imaging at high magnetic fields. European journal of radiology 46(1):45-52.

Walczak P, Bulte JW. 2007. The role of noninvasive cellular imaging in developing cell-based therapies for neurodegenerative disorders. Neurodegenerative diseases 4(4):306-313.

Chapter 4

Detailed visualization of the functional regions of the rat pituitary gland by high resolution T2-weighted MRI

Outline Chapter 4

4.1 Introduction

4.2 Materials and methods

4.3 Results

4.3.1 Post-mortem magnetic resonance imaging

4.3.2 *In vivo* magnetic resonance imaging

4.3.3 Histology

4.4 Discussion

4.5 Conclusions

4.1 Introduction

The pituitary gland (PG) is an endocrine organ secreting many different hormones, which in turn activate even more peripheral target (endocrine) cells (Davidovici et al., 2008; Hiller-Sturmhofel and Bartke, 1998). It plays a major role in endocrine aspects of homeostasis. The release or production of hormones from the pituitary gland is regulated by the hypothalamus. The PG of the rat is attached to the base of the brain at the level of the mesodiencephalic junction. It consists of two distinct parts: neural part or neurohypophysis and a glandular component, called adenohypophysis. The neurohypophysis derives from embryologic diencephalic tissue and can be subdivided into the posterior lobe (pars nervosa), the pituitary stalk and the median eminence (di Iorgi et al., 2009). The latter part stores neurohormones (vasopressin and oxytocin) that are synthesized and forwarded by hypothalamic neurons. These hormones are released on demand in response to nerve impulses from the hypothalamus. The anterior and intermediate lobe together with the pars tuberalis form the adenohypophysis (Armstrong, 2004). Hormone secreting cells which regulate the activity of peripheral endocrine glands are located within the anterior lobe. They release trophic hormones such as thyroid stimulating hormone (TSH), adrenocorticotrophin (ACTH), luteinising hormone (LH) and follicle stimulating hormone (FSH). TSH stimulates the thyroid to produce the thyroid hormones T3 and T4. ACTH induces the release of cortisol by the adrenal glands. LH and FSH exert effects on the gonads. Further, the adenohypophysis produces also growth hormone and prolactin (Adams, 2006). The intermediate lobe cells synthesize peptides of the pro-opiomelanocortin family (Armstrong, 2004).

Dysfunction or disease of the pituitary gland can lead to a wide variety of clinical syndromes. Trauma, neoplasia, congenital defects, inflammation and idiopathic conditions can affect the pituitary gland, resulting in hypo- or hypersecretion of hormones what leads to homeostatic imbalance (Anderson et al., 1999). Pituitary gland disorders are studied by numerous animal models in rat (Castro et al., 2003; Cross et al., 2007; Serizawa, 1993). Beside functional endocrine blood tests, complementary information can be achieved by imaging the

pituitary gland *in situ*, thereby showing the morphology and spatial position of the gland in relation to the complete rat brain architecture.

To date, the morphology and fine structure of the rat pituitary gland have been mainly studied by histology. The lack of detailed anatomical images of the gland in situ urges for additional imaging methods (Seo et al., 2002; Yamada et al., 1997). Therefore the use of a non-invasive imaging technique would be of great value to overcome this shortcoming. With regard to these expectations, high field MRI is suggested as an interesting tool for visualizing the central nervous tissue in different imaging planes with a high degree of detail.

This study focuses on highly detailed anatomical MR images of the rat's pituitary gland using a 9.4 Tesla (T) vertical bore scanner. In order to visualize the three lobes of the PG, proton density (PD) and T2-weighted contrast methods are evaluated in addition to conventionally used T1-contrast. The signal intensities in the images are explained from a molecular point of view, i.e. by means of the local water concentration and the T1- and T2-relaxation decay times. The latter are dependent on the molecular mobility of the water molecules (see chapter 2), which in turn is defined by the tissue composition and organization. An understanding at the molecular level is of utmost value for scientists studying changes of the PG at the functional level, since it correlates functional changes with structural tissue changes. The feasibility of using these contrast methods for *in vivo* studies is also assessed.

4.2 Materials and methods

Animals

Adult Lewis rats (Harlan CPB, Zeist, The Netherlands) of 8 weeks (150 g) old were housed in cages with free access to food and water. *Ex vivo* MR imaging was performed on non-fixed brain tissue. Animals (n=3) received a lethal injection of Nembutal (Natriumpentobarbital 60 mg/ml - 150 µl/100 g body weight) and were immediately subjected to MRI.

For *in vivo* MRI (n=3), anaesthesia was induced by inhalation of 2.5% isoflurane and maintained with 1.5% isoflurane in carbogen (95% oxygen and 5% carbon dioxide). Body temperature was maintained at 37°C by heated air that was delivered into the sample holder at the level of the rat.

Animals (n=6; 3 for coronal and 3 for sagittal sectioning) used for histological matching, were sedated with an intraperitoneal injection of Nembutal® (Natriumpentobarbital 60 mg/ml - 75 µl/100 g body weight). Then, animals were transcardially perfused using 1 ml heparin (1000 I.U./ml) and chilled NaCl 0.9 % to wash out the blood. Next 4% paraformaldehyde (PFA) in PBS (pH 7.4) was perfused to fix the brain tissue.

All experimental procedures were approved by the Ethical Committee for Animal Experiments of the Hasselt University, Diepenbeek, Belgium. All efforts were made to minimize the number of animals used, as well as their suffering.

Magnetic resonance imaging

Ex vivo imaging was done in a 25 mm birdcage coil on a 9.4 Tesla (T) vertical bore magnet (Varian Inova 400 spectrometer, Varian, Nuclear Magnetic Resonance Instruments, Paolo Alto, California, USA) in three orthogonal slice directions at 4°C. High resolution MR images of the rat brain were obtained by means of a multi-slice spin-echo sequence. Highly PD-weighted images [TR = 2500ms/TE = 18ms (TR=repetition time/TE=echo time)] as well as T1- and T2-

weighted images [650ms/22ms and 2500ms/55ms respectively) were acquired. PD, T1-and T2-weighted images were obtained using 20, 32 and 36 number of averages (NA), respectively. All images were acquired as consecutive 1-mm-thick slices with an in-plane resolution of 40 x 40 µm. The field of view (FOV) was 25 x 25 mm and 35 × 25 mm for the axial and sagittal imaging plane, respectively. Axial images were additionally acquired as consecutive 0.5-mm-thick slices.

The determination of the local T2-relaxation decay times was carried out with a TR of 2500ms and the following echo time array: 16, 25, 30, 35, 40, 45, 50, 55, 65 and 75 ms. Images were acquired with NA=4. A non-linear least square fit (Levenberg-Marquardt algorithm) was used to extract the local T2-decay times and spin densities of the regions of interest. Local T1-values were determined as described above, using a TE of 22 ms and a repetition time array of 400, 500, 700, 900, 1200, 1500, 2000, 2500, 3000 and 4000 ms.

In vivo imaging was performed with a Varian 40 mm Millipede probe on a vertical bore magnet (9.4T). Sagittal *in vivo* imaging of consecutive 1 mm thick slices, was carried out with a FOV of 40 x 35 mm. T1-weighted imaging [650ms/22ms] was performed with an in-plane resolution of 80 x 70 µm and NA = 4. T1-weighted images were obtained in about 20 minutes. T2-weighted images [2000ms/40ms] were obtained with an in-plane resolution of 100 x 70 µm. Acquisition time was 30 minutes (NA = 1).

Light microscopy
The fixed PG was embedded in paraffin. Then, 5 µm thick axial or sagittal sections were mounted on glass slides and stained using Trichrome von Masson (TM). The specimens were examined using a Nikon Eclips 80i light microscope.

4.3 Results

4.3.1 Post-mortem magnetic resonance imaging

MRI parameters were obtained by varying the TE for the T2-weighted images around the selected value (55 ms) for unfixed tissue. A TE value of 40 ms resulted in high resolution post-mortem MR-images that clearly show not only the gross anatomy of the rat brain architecture **(Fig. 4.1)**, but also allow the visualization of small structures like the pituitary gland with high precision. T2-weighted as well as PD-weighted mid-sagittal images show three distinct parts of the PG **(Fig. 4.1),** i.e. the posterior lobe, the anterior lobe and the intermediate lobe.

The images demonstrate that the PG has an irregular shape and is located on the ventral side of the rat brain at the mesodiencenphalic junction. Its position is 4 to 7 mm posterior and 9.5 to 11 mm inferior to the bregma (Paxinos and Watson, 1998). Based on our mid-sagittal images of three rats, the maximal anterior-posterior axis is 3 mm and the dorso-ventral distance is 1.5 mm. On coronal images, the latero-lateral diameter of the gland has a maximal size of 4.7 mm. The connection of the pituitary gland with brain tissue is clearly observed at the mid-sagittal section where a slender pituitary stalk continues into three parts **(Fig. 4.1)**.

Since proton density (M_0 =water concentration) is rather similar all over the PG **(Table 4.1)**, contrast in the images mainly has to arise from differences in local relaxation. This information also explains why the delineation of the micro-anatomy is less clear in the PD-weighted image **(Fig. 4.1A)** which is only slightly T2-weighted. The intermediate lobe is seen as a small hyper-intense zone separating the other two lobes. Normo-intense signal intensity is shown for both the posterior and anterior lobe.
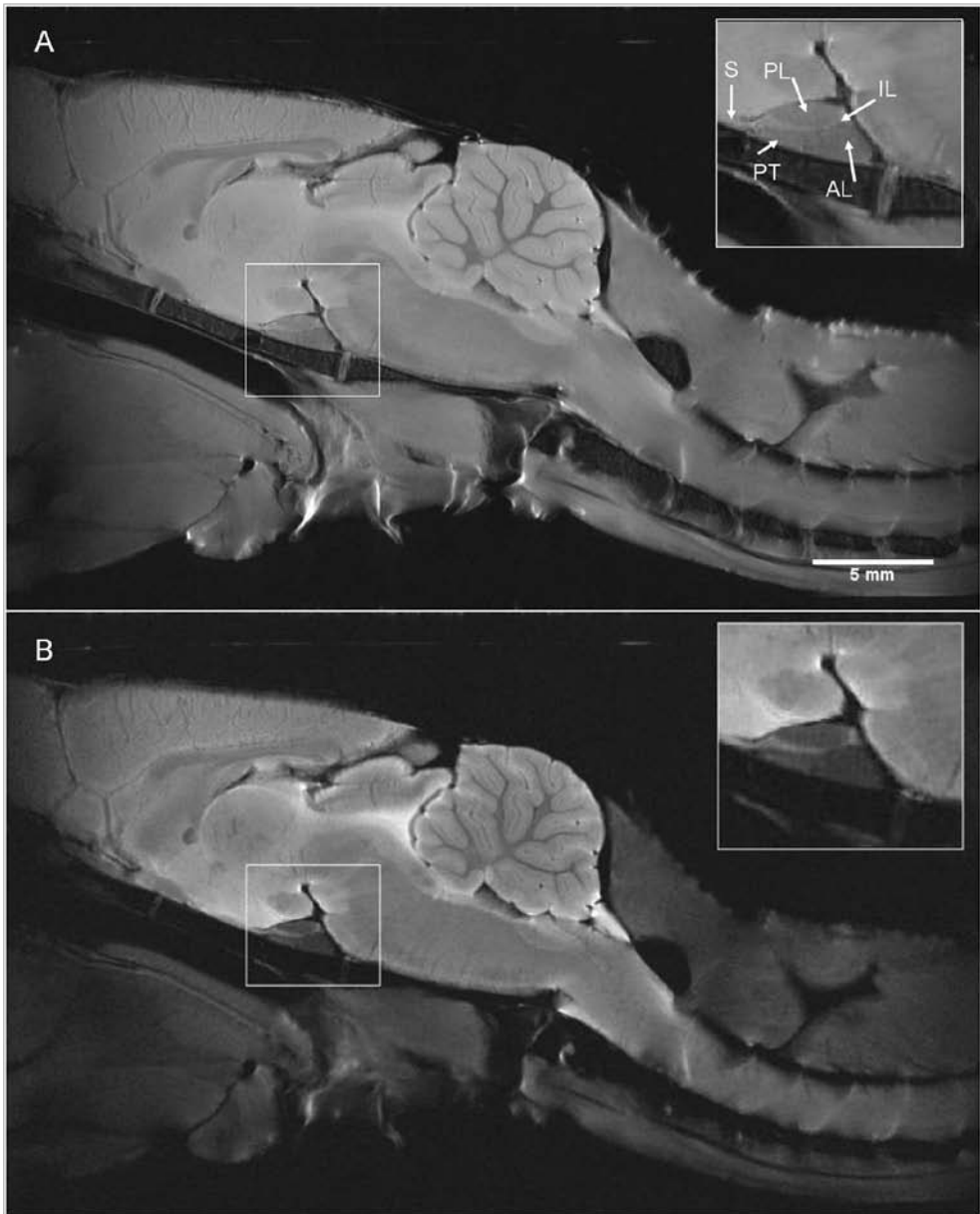
Figure 4.1: A mid-sagittal view of the pituitary gland (unfixed tissue). Both PD (A) and T2-weighted (B) MR images show the PG. Insert depicts an enlargement of the PG with its lobes, i.e. S pituitary stalk, PL posterior lobe, IL intermediate lobe, AL anterior lobe and its most anterior region the pars tuberalis (PT).

Figure 4.2: Post-mortem T1-weighted image of the rat's pituitary gland (unfixed tissue), showing the hyper-intense posterior lobe and the hypo-intense anterior lobe. Pituitary gland regions are shown on the magnification. AL anterior lobe, IL intermediate lobe and PL posterior lobe.

Pituitary gland region	T1 value (ms) ± SD	T1 value Normalized	T2 value (ms) ± SD	T2 value Normalized	M_0 value Normalized
Anterior lobe: pars distalis	1960 ± 60	142 %	25.6 ± 1.9	74 %	96 ± 1.7%
Anterior lobe: pars tuberalis	1920 ± 60	139%	28.1 ± 3.0	81%	110 ± 9.6%
Intermediate lobe	1375 ± 40	100 %	34.8 ± 2.3	100 %	100 ± 6.7 %
Posterior lobe	1490 ± 90	108 %	30.2 ± 1.2	87 %	106 ± 4.2 %

Table 4.1: T1 and T2 relaxation decay times and M_0 values of the lobes of the rat's pituitary gland, normalized towards the intermediate lobe. The values were determined on non-fixed rat specimens, immediately after sacrificing.

The local relaxation decay times of the posterior, intermediate and anterior lobe of the rat's pituitary gland are shown in **table 4.1**. As indicated by the normalized values, there is only a slight difference in the T1-value of the posterior and intermediate lobe which makes it difficult to distinguish them on T1-weighted images. The anterior lobe has a high T1-value resulting in a good delineation from the intermediate and posterior lobes. **Figure 4.2** shows a mid-sagittal T1-weighted image of the pituitary gland with the hyper-intense posterior and intermediate lobe and the hypo-intense anterior lobe. The intermediate lobe can not be distinguished on T1-weighted images.

Table 4.1 further shows different T2-decay times for the different PG regions. The intermediate lobe has a T2-value which is about 13% and 26% longer than this of the posterior and anterior lobe, respectively. These differences in T2-relaxation explain the difference in signal brightness and the superior tissue delineation as seen on the T2-weighted image **(Fig. 4.1B)**: the hypo-intense posterior lobe, the hyper-intense intermediate lobe and the most hypo-intense zone of the anterior lobe. The pars tuberalis lying at the rostral part of the anterior lobe has a subtle brighter intensity than the pars distalis of the anterior lobe due to a slightly longer T2-value and higher M_0-value (higher water content.

Three lobes of the PG are also delineated on thin T2-weighted axial MR images of 0.5 mm thickness **(Fig. 4.3)**. Such images show the PG as an oval shaped region where the hyper-intense signal of the intermediate lobe separates the hypo-intense posterior lobe from the hypo-intense anterior lobe. The large anterior lobe almost completely surrounds the intermediate and posterior lobes.

Figure 4.3: Axial T2-weighted image of the pituitary gland having a slice thickness of 0.5 mm (unfixed tissue). Axial sections show the three compartments of the PG: AL anterior lobe, IL intermediate lobe and PL posterior lobe as shown on the magnification.
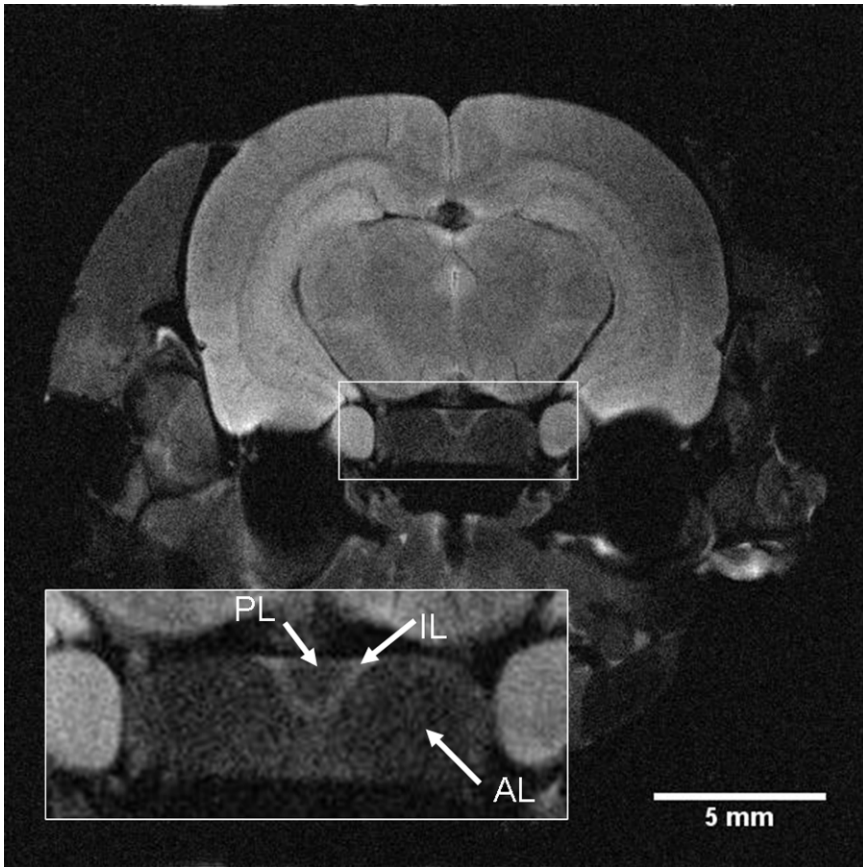
4.3.2 In vivo magnetic resonance imaging

In vivo acquisition of T1- or T2-weighted sagittal images also shows the gross anatomy of the rat brain **(Fig. 4.4)**. The triangular shape of the PG can be clearly seen on the MR images with a similar morphological delineation as for the post-mortem images. T1-weighted *in vivo* images show a hyper-intense posterior lobe and a hypo-intense anterior lobe. On T2-weighted images both the posterior and anterior lobe can be observed as hypo-intense, clearly separated by the intermediate lobe, which is hyper-intense.
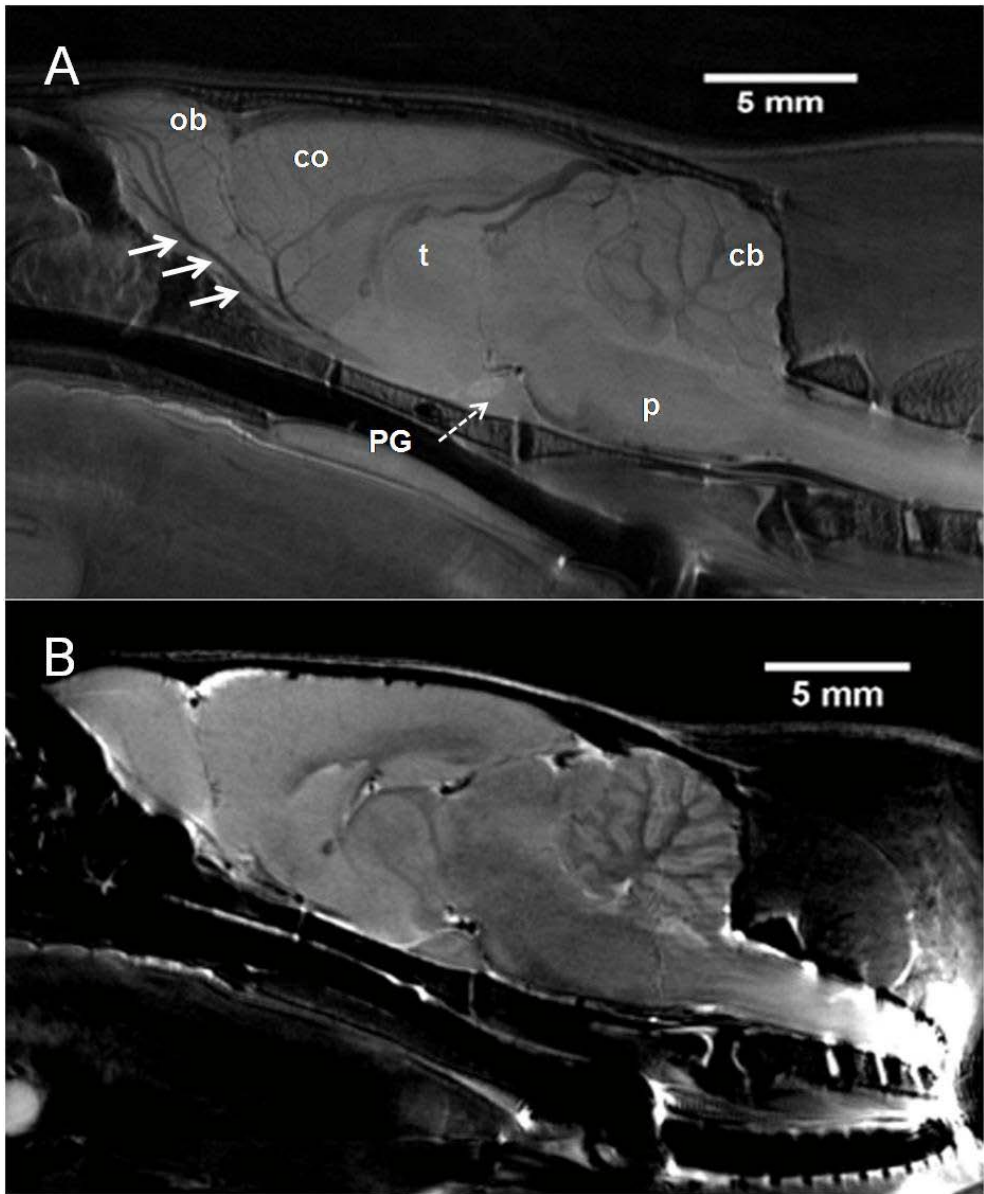
Figure 4.4: In vivo T1- and T2-weighted images of a mid-sagittal section of the rat brain showing the different compartments of the pituitary gland. (A: T1-weighted, B: T2-weighted). Remark the visualization of blood vessels (white arrows). Cb: cerebellum, co, telencephalic cortex, p: pons, PG: pituitary gland, t: thalamus, ob: olfactory bulb.

4.3.3 Histology

Matching histological sections are provided and conventional staining with Trichrome von Masson (TM) shows the three distinct regions of the pituitary gland **(Fig. 4.5)**. The region of the adenohypophysis stains intensely red. The upper region has a light pink color and is known as the neurohypophysis. A small pale purple stroke can be seen between these two parts, i.e. the intermediate lobe. The bulk of the neurohypophysis, composed of nerve endings and unmyelinated axons from hypothalamic neurosecretory neurons, also contains supporting cells known as pituicytes. The posterior lobe houses abundant capillaries, particularly in that portion where most hormone release occurs. The group of Seyama et all demonstrated that many of these capillaries are fenestrated, facilitating the delivery of hormones into the blood (Seyama et al., 1980). Three distinct cell types are recognized in the pars distalis of the adenohypophysis based upon cytoplasmatic staining characteristics. Acidophils have a eosinophilic cytoplasm and produce hormones such as prolactin and growth hormone. Cells with a bluish coloured cytoplasma secrete TSH, FSH, LH and ACTH. Chromophobe cells are depleted of hormonal content.
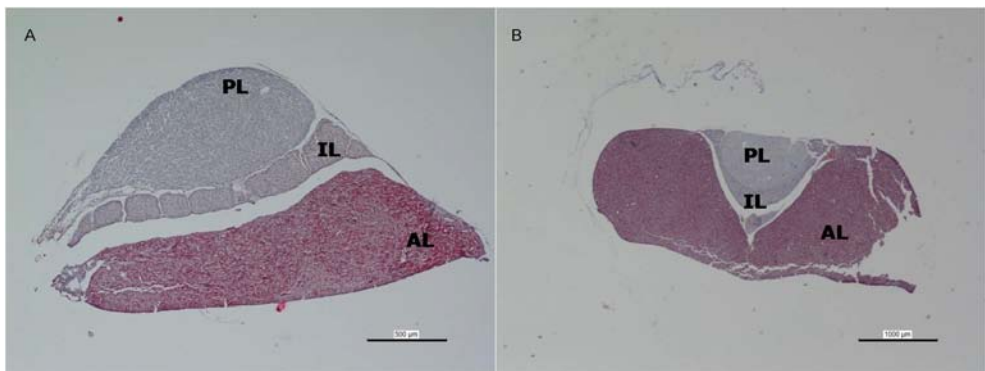
Figure 4.5: Corresponding histological sections of the rat pituitary gland. A mid-sagittal (A) and coronal (B) histologic section of the PG are stained by a Trichrome von Masson protocol. PL: posterior lobe, IL: intermediate lobe, AL: anterior lobe.

4.4 Discussion

This study shows that high resolution MRI offers highly detailed anatomical and structural information, allowing the interpretation of the spatial intracranial organization of the PG and its anatomical relation with the complete rat brain and this without physical slicing up of the brain tissue. The detailed anatomy of the PG on the MR images is confirmed by matching histological sections. Post-mortem mid-sagittal T2-weighted MR images visualize a sharp delineation of the separate lobes of the pituitary gland. To date, the rat's PG was never imaged better in terms of resolution and image quality (Chuang and Koretsky, 2009; Cross et al., 2007; Finkelstein et al., 2008; Seo et al., 2002; van Nesselrooij et al., 1992; Yamada et al., 1997).

Clinical imaging uses low field (1 to 3 T) MR scanners to image the human PG with T1-weighted sequences in a short period of time (Anderson et al., 1999). On these T1-weighted images, a typical strong hyper-intense zone represents the posterior lobe while the anterior lobe shows a weaker signal intensity (Castillo, 2005; Saleem et al., 2007). Despite a good delineation between the posterior and anterior lobe, the intermediate lobe, being regressed in humans, is not observed on clinical T1-weighted MR scans (Takeuchi, 2001).

In this chapter, it is demonstrated that the intermediate lobe of rodents, being well developed, cannot be discriminated on T1-weighted high field MR images either. The T1-weighted images of the PG also show a hyper-intense posterior lobe and a rather hypo-intense anterior lobe. Analysis of the T1-relaxation curves demonstrated only a weak difference between the T1-values of the posterior and intermediate lobe explaining why they can not be delineated from each other. They can only be distinguished from the anterior lobe. The anterior lobe has the longest T1-decay time, which is reflected in its hypo-intense signal intensity. For T1-weighted images of the PG, it can be concluded that only the posterior and anterior lobe can be delineated.

Additionally to T1-weighted contrast, PD and T2-weighting, two other relaxation-based contrast modalities were evaluated in order to visualize the small intermediate lobe. Since proton density (M_0) is rather similar all over the PG, contrast in the images mainly has to arise from differences in local relaxation. Determination of the local T2-values of the three lobes showed that there is only a small difference in T2-relaxation between the posterior and anterior lobe. However, the T2-value of the intermediate lobe is sufficiently higher and results in a bright signal intensity. Based on this hyper-intense signal of the intermediate lobe, it is possible to delineate the three separate lobes of the rat's PG. The pars tuberalis, being the most anterior part of the anterior lobe can be differentiated from the posterior part based on its longer T2-decay time and slightly higher water content. These results indicate that other ways of contrast such as T2 contrast or contrast agents might be worthwhile to be explored in the clinic to visualize the three lobes of the pituitary gland.

Literature about the biochemical or functional background of signal intensities seen on MR images of the PG is very limited and mostly restricted to knowledge of human MRI (Bonneville et al., 2006; Caruso et al., 2001). The hypo-intense signal of the posterior lobe on T2-weighted images can be explained by the storage of vasopressin, a hormone synthesized by the hypothalamus and stored in the posterior pituitary gland (Bonneville et al., 2006). For its transport to the pituitary gland, vasopressin is bound to a macroproteic molecule, known as the vasopressin-neurophysin II-copeptin complex, which shortens the T2-relaxation of the measured water molecules due to strong motional restrictions.

Many different hormones are produced and released in the dense vascular network of the adenohypophysial part of the gland. Besides the presence of large hormonal peptide complexes, the dense vascularization explains why the T2-relaxation is mostly enhanced in the anterior lobe. The intermediate lobe has the longest T2-value resulting in a hyper-intense signal on T2-weighted images. It can be ascribed to the less structured organization of the intermediate lobe. As a conclusion, the different signal intensities of the three lobes are due to

specific structural and biochemical tissue characteristics which are reflected by the different local T2-decay times.

According to the literature, the MR characteristics of non-fixed rat brain have been found not to change within the first 24 hours after biopsy (Carvlin et al., 1989; Thickman et al., 1983). For that reason, it can be assumed that the T1- and T2-relaxation decay times reflect rather well the *in vivo* values. As a confirmation, the T1- and T2-weighted *in vivo* images of the pituitary gland indeed reveal similar contrast intensities **(Fig. 4.4)**. It demonstrates the feasibility to obtain *in vivo* images of the rat brain with good resolution and contrast within a relative short time. Although no synchronic triggering for heart-lung related movements was applied, the posterior and anterior lobe can be clearly differentiated on T1-weighted images, while the three lobes can be delineated on T2-weighted *in vivo* images **(Fig. 4.4)**.

Therefore, high resolution MRI offers new perspectives for an *in vivo* functional exploration of the pituitary gland in rat animal models. Experimental therapeutic or diagnostic interventions can be evaluated and optimized in rat animal models and later on extrapolated to the clinical setting. Especially in the field of pituitary tumor studies, MR imaging looks promising. High resolution MRI combined with contrast labeled ligands can be used for early diagnosis and staging of pituitary tumors as they express high levels of somatostatin receptors (Burdette, 2008; Heaney and Melmed, 2004). A better understanding of the molecular characteristics, leading to the normal appearance of the pituitary gland, can further enforce the use of MRI in evaluating pathological abnormalities. T2-weighted imaging can be used to demonstrate the presence of iron depositions in the anterior lobe of the PG in thalassemia. The PG seems to be a common target organ for iron deposition and this may result in complications as hypogonadism or short stature (Sparacia et al., 1999). The (normalized) signal intensity in T2-weighted images of the anterior lobe obtained from thalassemia patients correlated well with ferritin levels in the blood (Lam et al., 2008). Therefore measuring the signal intensity in T2-weighted images might be useful to reflect hemosiderosis in the PG or could have a role in monitoring chelation

therapy or evaluating newly developed chelation drugs in animal models. The clear visualization of the three lobes on T2-weighted images offers the opportunity to determine the size of each lobe in all imaging directions. When peripheral endocrine glands are removed or become dysfunctional, the negative feedback mechanisms towards the PG become disturbed. It might result in hypertrophic changes of the PG lobes. MR-images can non-invasively provide morphometric information to evaluate the size of the global PG or of each lobe separately (Teshima et al., 2009).

Not only high resolution *in vivo* small animal imaging is gaining more interest, but also human scanners with high magnetic fields (> 3 T) are more and more introduced in the clinic for acquiring qualitative high resolution images. There are currently more than thousand 3 T MRI scanners and about thirty 7 T clinical MRI systems in use - or about to be installed - around the world, more than half of them in Europe. Two 9.4 T human MRI scanners are already operating in Germany, while France will soon install an 11.7 T clinical MRI system (Vedrine et al., 2008). Imaging at high field increases the SNR, improves anatomic resolution and reduces scan time while preserving image quality.

4.5 Conclusions

High resolution T2-weighted MRI images, acquired at 9.4T in the sagittal and axial planes and in the absence of contrast agents, clearly delineate the three distinct lobes of the rat's pituitary gland, i.e. the posterior, the intermediate and the anterior lobe. The differentiating signal intensities of the three lobes are due to a different tissue organization which is reflected by the different T1- and T2-decay times. This makes high field MRI a powerful tool to reveal morphological or pathological abnormalities of the pituitary gland in rat animal models. Moreover, this study provides new perspectives for *in vivo* functional exploration of PG pathologies in rat animal models.

References

Adams EF. 2006. The study of the pituitary gland using animals and alternative: can the latter completely replace the former? Environmental toxicology and pharmacology 21:141-147.

Anderson JR, Antoun N, Burnet N, Chatterjee K, Edwards O, Pickard JD, Sarkies N. 1999. Neurology of the pituitary gland. Journal of neurology, neurosurgery and psychiatry 66(6):703-721.

Armstrong WE. 2004. In: Paxinos G, editor. The rat nervous system. 3th ed.15. Elsevier Academic Press. p 369-388.

Bonneville F, Cattin F, Marsot-Dupuch K, Dormont D, Bonneville JF, Chiras J. 2006. T1 signal hyperintensity in the sellar region: spectrum of findings. Radiographics 26(1):93-113.

Burdette JE. 2008. In vivo imaging of molecular targets and their function in endocrinology. Journal of molecular endocrinology 40(6):253-261.

Caruso RD, Postel GC, McDonald CS, Sherry RG. 2001. High signal on T1-weighted MR images of the head: a pictorial essay. Clinical imaging 25(5):312-319.

Carvlin MJ, Asato R, Hackney DB, Kassab E, Joseph PM. 1989. High-resolution MR of the spinal cord in humans and rats. American journal of neuroradiology 10(1):13-17.

Castillo M. 2005. Pituitary gland: development, normal appearances, and magnetic resonance imaging protocols. Topics magnetic resonance imaging 16(4):259-268.

Castro M, Goverdhana S, Hu J, Jovel N, Yuan X, Lowenstein P. 2003. Gene therapy for pituitary tumors: from preclinical models to clinical implementation. Frontiers in neuroendocrinology 24(1):62-77.

Chuang KH, Koretsky AP. 2009. Accounting for nonspecific enhancement in neuronal tract tracing using manganese enhanced magnetic resonance imaging. Magnetic resonance imaging 27(5):594-600.

Cross DJ, Flexman JA, Anzai Y, Sasaki T, Treuting PM, Maravilla KR, Minoshima S. 2007. In vivo manganese MR imaging of calcium influx in spontaneous rat pituitary adenoma. American journal of neuroradiology 28(10):1865-1871.

Davidovici BB, Orion E, Wolf R. 2008. Cutaneous manifestations of pituitary gland diseases. Clinics in dermatology 26(3):288-295.

di Iorgi N, Secco A, Napoli F, Calandra E, Rossi A, Maghnie M. 2009. Developmental abnormalities of the posterior pituitary gland. Endocrine development 14:83-94.

Finkelstein Y, Zhang N, Fitsanakis VA, Avison MJ, Gore JC, Aschner M. 2008. Differential deposition of manganese in the rat brain following subchronic exposure to manganese: a T1-weighted magnetic resonance imaging study. The Israel medical association journal 10(11):793-798.

Heaney AP, Melmed S. 2004. Molecular targets in pituitary tumours. Nature Reviews. Cancer 4(4):285-295.

Hiller-Sturmhofel S, Bartke A. 1998. The endocrine system: an overview. Alcohol health and research world 22(3):153-164.

Lam WW, Au WY, Chu WC, Tam S, Ha SY, Pennell DJ. 2008. One-stop measurement of iron deposition in the anterior pituitary, liver, and heart in thalassemia patients. Journal of magnetic resonance imaging 28(1):29-33.

Paxinos G, Watson C. 1998. The rat brain in stereotaxic coordinates. 4th edition. Academic Press.

Saleem SN, Said AH, Lee DH. 2007. Lesions of the hypothalamus: MR imaging diagnostic features. Radiographics 27(4):1087-1108.

Seo Y, Takamata A, Ogino T, Morita H, Nakamura S, Murakami M. 2002. Water permeability of capillaries in the subfornical organ of rats determined by Gd-DTPA(2-) enhanced 1H magnetic resonance imaging. The Journal of physiology 545(Pt 1):217-228.

Serizawa N. 1993. Initial characterization of a new miniature animal model in the rat: studies on anatomy, pituitary hormones and GH mRNA in miniature rat Ishikawa. Nippon naibunpi gakkai zasshi 69(1):33-45.

Seyama S, Pearl GS, Takei Y. 1980. Ultrastructural study of the human neurohypophysis. III. Vascular and perivascular structures. Cell and tissue research 206(2):291-302.

Sparacia G, Midiri M, D'Angelo P, Lagalla R. 1999. Magnetic resonance imaging of the pituitary gland in patients with secondary hypogonadism due to transfusional hemochromatosis. Magma (New York, NY 8(2):87-90.

Takeuchi M. 2001. The Mammalian Pars Intermedia — Structure and Function. Zoological science 18: 133–144.

Teshima T, Hara Y, Takekoshi S, Nezu Y, Harada Y, Yogo T, Teramoto A, Osamura RY, Tagawa M. 2009. Trilostane-induced inhibition of cortisol secretion results in reduced negative feedback at the hypothalamic-pituitary axis. Domestic animal endocrinology 36(1):32-44.

Thickman DI, Kundel HL, Wolf G. 1983. Nuclear magnetic resonance characteristics of fresh and fixed tissue: the effect of elapsed time. Radiology 148(1):183-185.

van Nesselrooij JH, Szeverenyi NM, Ritter-Hrncirik C, Tillapaugh-Fay GM, Feron VJ. 1992. Rat pituitary changes observed with magnetic resonance imaging following removal of estrogen stimulus: correlation with histopathology and immunohistology. Carcinogenesis 13(2):277-282.

Vedrine P, Aubert G, Beaudet F, Belorgey J, Beltramelli J, Berriaud C, Bredy P, Chesny PH, Donati A, Gilgrass G, Grunblatt G, Juster FP, Molinie F, Meuris C, Nunio F, Payn A, Quettier L, Rey JM, Schild T, and Sinanna A. 2008. "The whole body 11.7 T MRI magnet forIseult/INUMAC project," IEEE transactions on applied superconductivity 18:868-873.

Yamada K, Chen CJ, Satoh H, Hirota T, Aoyagi K, Enkawa T, Ozaki Y, Sekiguchi F, Furuhama K. 1997. Magnetic resonance imaging of rat head with a high-strength (4.7 T) magnetic field. The Journal of veterinary medical science / the Japanese society of veterinary science 59(4):303-306.

Chapter 5

Post-mortem high resolution MRI of spinal cord injury. Qualitative correlation with histology and its relevance for morphometric analysis of lesioned spinal cord

In collaboration with Dr. Scholtes Felix
University of Liège

Outline chapter 5

5.1 Introduction

5.2 Materials and methods

5.3 Results

      5.3.1 Proton density MRI of an injured spinal cord-spine block

      5.3.2 Pathologic hallmarks at different survival times after SCI as visualized on PD images

      5.3.3 Inversion recovery imaging for selective detection of spared white matter

      5.3.4 Behavioural recovery after SCI

      5.3.5 Morphometric parameters derived from PD MR-images with support of IR MR-images

5.4 Discussion

5.5 Conclusions

5.1 Introduction

Spinal cord injury (SCI) is a devastating clinical disorder leading to lifetime disability. Normal motor, sensory or autonomic functions are temporarily or permanently disturbed because descending or ascending white matter tracts are damaged by the trauma. A high incidence of SCI is seen among persons younger than 40, mostly of male gender (Sekhon and Fehlings, 2001). In the United States, it is estimated that the annual incidence is approximately 10 000 new cases each year. The etiology of SCI can be ascribed to motor vehicle accidents, falls, violence and sport injuries in decreasing order, although this may vary between different socio-economic regions (Ackery et al., 2004). This debilitating insult results in enormous emotional and physical cost for the individual but there is also an expensive long-time financial load to be carried by society (Priebe et al., 2007).

Up to now, there are no suitable therapeutic agents available to cure. A lot of biomedical research is performed on animal models to understand lesion development and mechanisms of natural recovery, but also new therapeutic strategies to improve recovery and life quality are under investigation (Basso, 2000). In many of these studies, it was demonstrated that remaining spared tissue after SCI was able to mediate some recovery of function (Basso et al., 1996). Therefore, new therapeutic approaches can focus on different aspects aiming to improve functional outcome after SCI. Neuroprotective strategies attempt to preserve the remaining tissue while repair mechanisms induce processes that replace the damaged tissue. Rehabilitation procedures stimulate the plasticity of the tissue resulting in new neuronal connections and restoration of functional outcome. In order to evaluate the potential effect of these three therapeutic interventions, it is important to have knowledge about the amount of spared tissue since it is known to be correlated with locomotor function as well as with recovery capacity. Several researchers have developed standarized histological methods to determine the peripheral rim of spared tissue (Behrmann et al., 1992; Moriarty et al., 1998; Olby and Blakemore, 1996) but also other techniques can be of interest when determining morphometric analysis, such as

MRI. That technique would be beneficial to perform serial follow-up of the lesioned animals during the therapeutic interventions without sacrificing the animals and moreover the resulting images show detailed information about the lesion site. MRI is at present an ideal, non invasive imaging modality to study the CNS, and in particular the spinal cord, due to very high soft tissue contrast (Tyszka et al., 2005). In the clinical setting, it has proven its usefulness in the evaluation of SCI: it can provide information about the presence of oedema or haemorrhage in the parenchyma, and the degree of extrinsic cord compression (Miyanji et al., 2007)

The rat spinal cord has been depicted using MRI since the late 1980s (Carvlin et al., 1989). MRI data (e.g. the length of the lesion and qualitative estimations of white matter sparing) could be correlated with post-SCI neurological function (Gensel et al., 2006; Mihai et al., 2008). However, until recently, the resolution of experimental MRI remained rather low. Therefore, the topography of the lesion was ill-defined, and the degree and anatomy of white matter sparing difficult to assess. White matter sparing is a key factor in behavioural recovery. The severity of SCI is mainly determined by the degree of injury inflicted on the long white matter tracts, disconnecting the sub-lesional cord from the supra-spinal control centres (You et al., 2003). Therefore, in any research that investigates behaviour after SCI, and which assesses the locomotor effects of therapeutic strategies in particular, knowledge about the severity and the anatomy of the lesion is essential. The axial topography of injury appears particularly interesting, because the different motor fibre tracts driving locomotion run in defined areas in the spinal cord white matter funiculi (Matesz et al., 2002; Webb and Muir, 2004).

MRI technology can provide the means for visualizing the injury and white matter sparing. Experimental *in vivo* SCI MRI has been increasingly tested; the hardware for very high field *in vivo* spinal cord MRI is available for small rodents, including mice (Behr et al., 2004; Bilgen et al., 2006; Weber et al., 2006). Being technically less challenging than *in vivo* MRI and immediately

applicable at the present state of technology, *ex vivo* MRI also has the potential for higher image quality.

The MRI study therefore presents *post-mortem* investigation at 9.4 tesla of a spinal cord-spine block after experimental partial SCI using standard MRI sequences.

Goals were:

1) to show macroscopic changes *in situ* (like cord swelling due to acute oedema and cord atrophy due to chronic scarring processes),

2) to detect and distinguish lesion components (e.g. haemorrhage, oedema and necrosis),

3) to characterize the development of these changes over time (using different survival times),

4) to determine the precision of MR-based anatomical lesion assessment (histological correlation),

5) to demonstrate the feasibility to depict white matter sparing and other morphometric parameters that correlate with locomotor recovery.

A compromise was sought between best possible spatial resolution and minimal acquisition time, in order to obtain rapid and efficient *post-mortem* assessment of rat SCI severity and anatomy.

5.2 Materials and Methods

All experiments were performed in accordance with the rules and regulations of the Ethics Committee for Animal Research of the Belgian National Funds for Scientific Research (FNRS) and University of Hasselt.

Spinal cord compression lesion

Female Wistar rats of approx. 230 g (n=21) underwent surgery in order to create a moderate partial low thoracic spinal cord injury using a subdural balloon compression technique as described elsewhere (Martin et al., 1992) (**Fig. 5.1**).
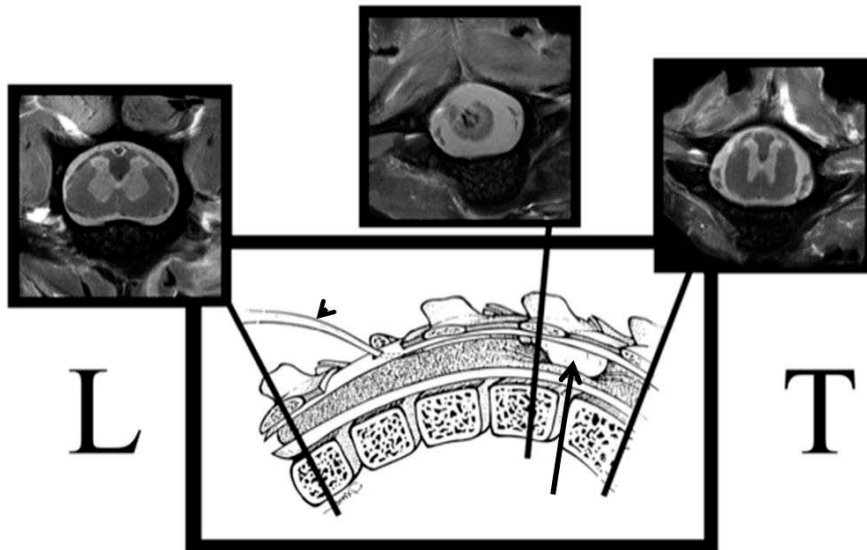
Figure 5.1: The inflated balloon technique was used in a closed spinal canal to induce a compression lesion at low thoracic level of the spinal cord. Legend: arrow – balloon, arrowhead – catheter to fill balloon, T – thoracic and L - lumbar.

Briefly, a balloon was introduced into the subdural space at the tenth thoracic level, moved 6 mm rostrally and inflated with 20 µl of sterile water for five minutes. After removal of the balloon, the muscles and skin were closed in two layers. After surgery, dehydration was prevented by intraperitoneal physiological

saline injections and infection by immediate post-operative intraperitoneal injection of amoxicilline-clavulanic acid. The bladder was manually expressed daily until rats developed spontaneous micturition. Urinary infections were treated as needed. Rats were housed separately. Food and water were provided *ad libitum*.

Rats used for visualizing the pathological hallmarks: to show the pathological hallmarks of SCI and their evolution over time on MR images, 16 rats were operated and sacrificed at different survival times, ranging from 1 day to 5 months **(Table 5.1)**.

Survival time (dpo)	1	4	7	14	21	28	56	150
Number of rats	3	3	3	1	1	3	1	1

Table 5.1: Animal groups used to study the evolution of pathologic hallmarks after SCI. At different survival times, animal were sacrificed and submitted to MR imaging and histologic analysis. Dpo = day post operation.

Rats used for visualizing spared white matter: the potential of high resolution MR images to visualize spared white matter and to determine morphometric parameters that might correlate with locomotor recovery patterns after SCI was investigated on another set of 5 operated rats. Their behavioural recovery was followed for 8 weeks (56 dpo) before analysis by MRI and histology.

Behavioural analysis

The motor function in the hind limbs of the five rats was evaluated weekly using the Basso, Beattie, Bresnahan (BBB) open field locomotor test (Bilgen et al., 2000). The first evaluation was accomplished four days post-operation and the last one after 2 months (eighth weeks). Before the behavioural observation, bladders were emptied to avoid the hind limb activity associated with voiding.

Two blinded examiners scored locomotion from 0 to 21 for both hind limbs over four minutes in a standardized open field.

Magnetic Resonance Imaging

Post-mortem imaging was carried out on following survival delays: 1 day post-operation (dpo), 4 dpo, 7 dpo, 14 dpo, 21 dpo, 28 dpo, 56 dpo and 150 dpo. Animals were deeply anesthetised by intraperitoneal pentobarbital (Nembutal® 0.7 ml, i.e. 300 µl / 100 g body weight) and perfused with 4% PFA. The spine was removed and post-fixed in 4% PFA for 48 hours, then stored for MRI in phosphate buffered saline (PBS)-azide. After a rapid preliminary image acquisition to locate the lesion level, spine specimens were analysed over a length of 23 mm, centred on the lesion site, using nuclear magnetic resonance imaging (MRI) performed in a 25 mm birdcage coil on a 9.4 T vertical bore magnet (Varian Inova 400 spectrometer, Varian, Nuclear Magnetic Resonance Instruments, Palo Alto, California, U.S.A.). All imaging acquisitions were performed at room temperature (20°C).

The following imaging sequences (and parameter settings) were used:

For all cords:

- Proton density (PD) images were obtained with a repetition time (TR) and an echo time (TE) of 2500 and 18 ms, respectively.

- All axial PD images were obtained as consecutive 1-mm slices using the multi-slice spin-warp technique. PD-images with an in-plane resolution of 38 µm x 38 µm (FOV of 17 mm x 17 mm and imaging data matrix 450 x 450) were acquired with a number of averages (NA) of 32, resulting in a total acquisition time of approximately 10 hours. Gradient strengths used were 6.21, 5.18 and 8.2 G/cm for read, phase (max) and slice direction, respectively and the slew rate was 15000 G/cm/s. PD-images with a medium resolution of 68 µm x 68 µm (FOV of 17 mm x 17 mm and imaging data matrix 250 x 250) were acquired with NA=8 (total acquisition time of about 1 hour) and with NA=4 (total acquisition time of less than half an hour). Gradient strengths were 3.45, 2.88 and 8.2 G/cm in the read, phase and slice direction respectively with the same slew rate.

In addition, horizontal images were acquired with 32 averages resulting in an acquisition time of approximately 10 hours for high resolution images (33 μm x 33 μm – FOV 30 mm x 13 mm and imaging data matrix 900 x 400). Gradient strengths were 7.04, 6.02 and 9.61G/cm in the read, phase and slice direction respectively with the same slew rate.

Rat for visualizing pathological hallmarks and their evaluation:

- This group was additionally imaged with a T1-, T2-, gradient echo (GE) and an inversion recovery (IR) weighted sequence, adjusted to suppress the signal of free water.

- The parameters for T1-weighted imaging were: TR=400 ms, TE=18 ms, NA = 64 and for gradient echo imaging TR=200 ms, TE=6 ms, NA=200 and pulse angle=22.5°. T2-weighted images [TR=2500 ms / TE=55 ms] were obtained with NA=28 (tat about 6 hours). IR images were acquired with a TR=2500 ms, TE=18 ms and an inversion time (TI) of 1750 ms to suppress the signal of free water. The IR images were acquired over a distance of 11 mm centred on the lesion. IR-imaging was accomplished with NA=16 in about 21 hours. The images, acquired using these sequences, have a medium resolution of 68 x 68 μm.

Rats for visualizing spared white matter and performing morphometric analysis :

- The 2 month survival group for morphometric analysis was imaged with an IR-sequence, adjusted to suppress the signal of normal white matter.

- Hereto, IR images were acquired with a TR=2500 ms, TE=18 ms and a TI of 525 ms to suppress the signal of normal white matter. The images were acquired over a distance of 11 mm centred on the lesion. IR imaging was accomplished with NA=16 in about 7 hours. The images, acquired using this sequence, have a medium resolution of 68 x 68 μm.

Histology

After careful removal from the spinal canal and cryoprotection for a minimum of 48 h in 30% sucrose at 4°C, the spinal cords were frozen and cut transversally at a thickness of 15 µm on a cryostat, mounted onto gelatine coated slides and stained with a combination of haematoxylin and luxol fast blue to visualize myelin (Scholtz, 1977). One histological section out of 10 was analyzed, i.e. one section every 150 µm. This was sufficient to assess lesion anatomy, because the axial topography of the lesion and the shape and amount of residual spinal cord tissue did not change significantly over this distance. Each histological section was systematically compared to the MRI images. Photographs were taken of representative histological sections.

Morphometric analysis of chronic lesions

Image analysis was carried out on MR image overviews which showed consecutive images from the sub-lesional lumbar area to the supra-lesional thoracic area. Data were obtained using the Olympus FIVE® software with the help of two observers, blinded to BBB scores, who delineated the axial lesion extent on histological and MRI images. PD and IR images were used simultaneously to assign hypo-intense IR signal as spared white matter if this hypo-intensity was not observed in the PD image. When the hypo-intensity was observed in the PD and IR images, it was assigned to haemorrhage, i.e. due to the presence of iron. The morphometric measurements themselves were carried out on the higher resolution PD images.

For histological measurements, one out of 33 sections was analysed in the periphery of the lesion centre (two 6 mm blocks) and one out of 22 in the central block (11 mm), resulting in 10 peripheral sections and 30 central sections. Measurements were only made on sections that showed a lesion. Total spinal cord area and lesion area were determined. Spared white matter was calculated by subtracting for each individual MRI slice, the lesion area from the cord area. Spared white matter was subdivided into "total" and "ventral", the latter being ventral to a horizontal line centred on the ependymal canal if possible. In the other cases, ventral was defined to be in the ventral half of

the cord, and dorsal in the dorsal half. Areas were expressed in mm² and volumes in µl.

Graphs were established, showing the section number on the X-axis and the area measurements on the Y-axis in mm², depicting cord atrophy, lesion size, and spared matter **(Fig. 5.11)**. Atrophy of the spinal cord was defined by the minimal total cord area measured in each cord. Lesion volume was calculated as the area under the curve of the lesion area measurements; missing histological data points (due to excluded histological slices) were compensated for by the mean value of the two adjacent values. Spared matter (gray + white) was calculated by subtracting "lesion area" from "cord area". Non quantitative correlative figures were created to visually compare all five rats' BBB evolution with this morphometry.

5.3 Results

5.3.1 Proton density MRI of an injured spinal cord-spine block

As discussed in chapter 3, the fragile spinal cord is imaged within its backbone to avoid accidental damage to the tissue. The quality of the resulting PD-weighted MR images was very high in most of the cases **(Fig. 5.2 and 5.3)**. However, in some of the spines, air had entered the spinal canal and reduced image quality.
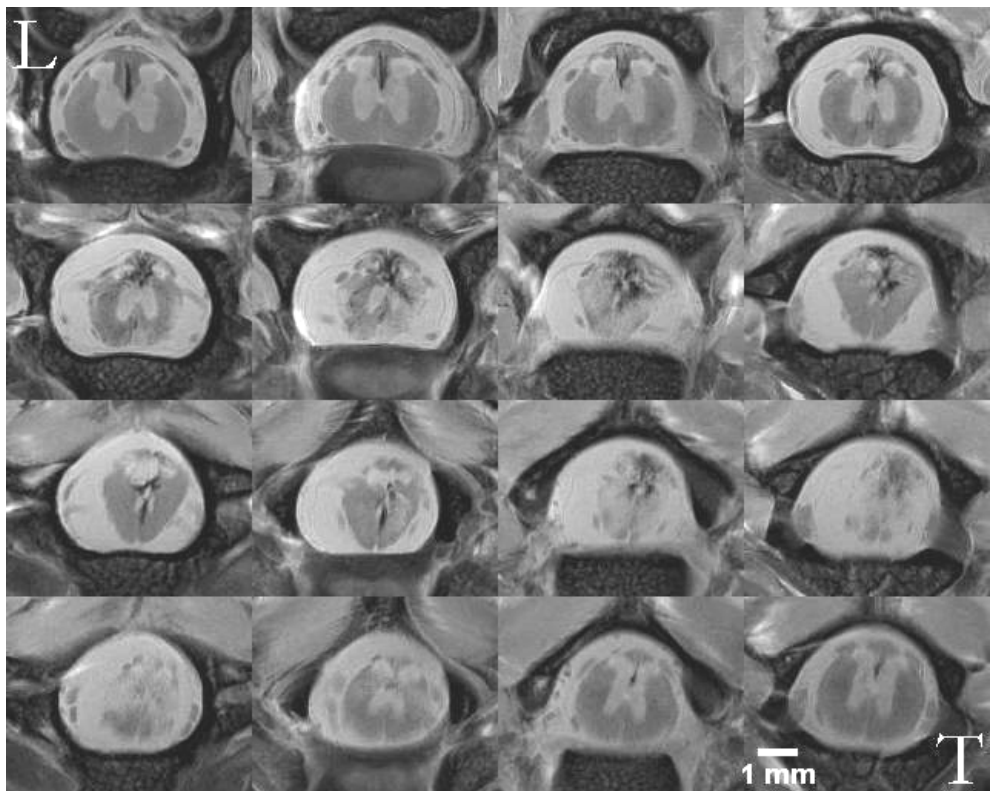
Figure 5.2: Overview of consecutive MR images of a lesioned spinal cord. The PD-weighted axial images show the spinal cord *in situ*, from lumbar to thoracic level (56 dpo; resolution 38 x 38 μm, NA=32). The first row depicts the sub-lesional area containing the characteristic gray matter shape, surrounded by white matter. In the next two rows, the induced compression lesion is represented. The supra-lesional area is seen in the last two images of row four. Legend: L = lumbar; T = thoracic. Scale bars indicate 1 mm.
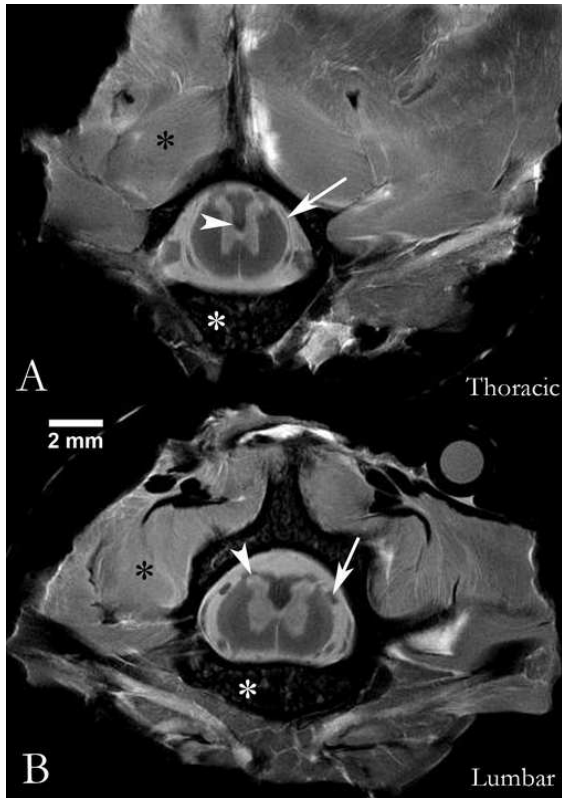
Figure 5.3: High resolution PD weighted MRI of the spinal cord-spine block (resolution 38 x 38 µm; NA=32); A: thoracic, B:lumbar. *In situ*, the vertebral bone (white asterisk) surrounds the spinal canal as low MR signal, i.e. almost black, except for the inter-trabecular spaces of the spongy bone in the vertebral body, ventral to the cord. The spine itself is surrounded by paravertebral muscle (black asterisk). Pronounced hypo-intense signal indicates the presence of the myelinated corticospinal tract in the ventral part of the dorsal columns, between the bases of the dorsal horns (A, arrowhead). Topping the dorsal horns, the substantia gelatinosa is hyper-intense (B, arrowhead). The dural sac can be seen around the spinal cord (A, arrow), and the two anterior and two posterior nerve roots appear with lower signal intensity (B, arrow).

The images do not only show the spinal cord tissue in detail, but they also provide information about its relation to surrounding tissues including muscular structures around the vertebra's, lesion level and even surgical traces of the balloon insertions. MRI precisely located the spinal cord lesion, in all three planes **(e.g., Fig. 5.2 and 5.4)**. Axial overviews show that the sub- and supra-lesional area contain normal appearing gray and white matter. The characteristic gray matter shape is indicative of the segmental level and has a more hyper-intense shade compared to the surrounding white matter. The lesion itself contains a mixture of signal intensities, which will be discussed further on in this chapter. The liquid filled spinal canal appears with high signal intensity, almost white.

The horizontal longitudinal images show the spinal cord from ventral part to the dorsal part. At the ventral side, the vertebral bodies are separated by the intervertebral disks. In the spinal canal, the gray matter can be distinguished from the white matter. The level of the lesion centre can be seen in relation to the vertebra. These horizontal images provide information about the lesion extension in the longitudinal direction.
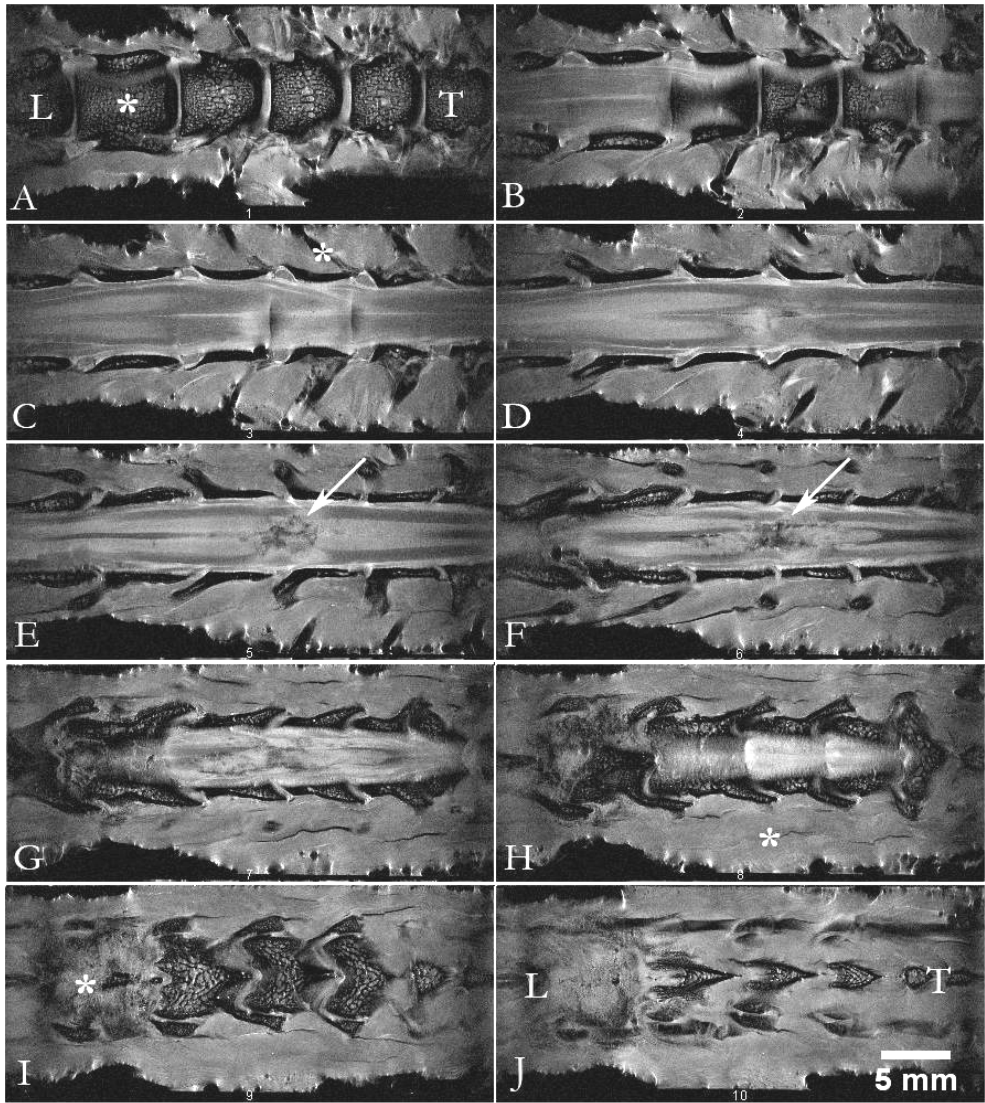
Figure 5.4: Longitudinal horizontal PD weighted images, from ventral (A) to dorsal (J); L=lumbar, T=thoracic: hypo-intense bony vertebral bodies (A, asterisk) separated by intervertebral disks; ribs (C, asterisk); paravertebral muscle (H, asterisk). In the canal, the spinal cord: rostrally and caudally, intact parenchyma; in between, the injury centre is precisely located in relation to the vertebrae and the nerve roots (E–F, arrows). Two metamers rostrally to the insertion site of the balloon (I, caudally: asterisk), the mostly hyper-intense, spindle-shaped lesion. The latter is seen mainly in the posterior half of the cord (D–G). The hyper-intense spindle extends rostro-caudally in the dorsal columns, between hyper-intense dorsal horns. The lesion centre shows some hypo-signal intensities (E-F, arrows). The dorsal laminae and the spinous processes close the spinal canal dorsally (H-J). Kyphosis of the rat spine at this level explains that each section shows different tissue planes. 7 days post-SCI. Resolution 38 x 38 µm; NA=32.

PD-weighted imaging provided the best compromise between acquisition time, resolution and image quality. Neither T1- nor T2-weighting offered better contrast (not shown). The inversion recovery technique adjusted for the suppression of free water, which had been developed in an attempt to distinguish oedema and necrosis in the acute state, simply suppressed the signal of the liquid in the CSF space. Oedema and necrosis or scarring processes could not be distinguished purely on the basis of the MR signal (not shown). Gradient echo imaging was used only on a few cords, because no information was added as compared to PD-weighted imaging. Therefore, all analyses were performed on PD-weighted images.

MRI could distinguish between lesion components. Luxol fast blue staining for visualization of myelin (i.e. intact white matter) combined with a haematoxylin counterstain demonstrated a precise correlation between abnormal PD MR signal intensity and histopathological changes in all cords **(Fig. 5.5)**. Increased MR signal in the acute stage corresponded to oedema, and in more chronic lesions to necrosis followed by scarring. Decreased MR signal intensity ("black") corresponded to haemorrhage, i.e. haemoglobin in the acute stage, and haemosiderin in the chronic stage, both being paramagnetic. MRI accurately

reproduced the lesion's topography. It precisely delimited the lesion's axial extent, depicted preserved tissue anatomy and detected intact white matter in the lesion periphery.

High versus "low" resolution PD MRI

When comparing lower resolution PD images (68 µm x 68 µm; NA=4 and 8) to higher resolution images (38 µm x 38 µm; NA=32), the difference in resolution is evident. However, image quality is still very good at lower resolutions, i.e. haemorrhage and oedema / necrosis can be detected and the lesion is well delineated, with acquisition times reduced to 25-50 minutes **(Fig. 5.5)**. The difference in the images obtained with a NA of 4 *versus* 8 resides only in the signal to noise ratio (SNR).

5.3.2 Pathologic hallmarks at different survival times after SCI as visualized on PD images

1 day post-SCI

24 hours after surgery, the spinal cord was invaded by a haemorrhagic lesion. **Figure 5.5** illustrates the precision of the topographical correlation between PD MRI and histology of the lesion. Haemorrhage clearly predominated in the grey matter **(e.g. Fig. 5.5 D)**, which appears to be mechanically more fragile than the white matter and subjected to greater stress by acute compression (Ichihara et al., 2003; Ichihara et al., 2001). However, in some areas it ruptured into the white matter funiculi **(Fig. 5.5 B-C)**. In the periphery of the lesions, gray and white matter were still distinct and clearly delimited after 24h **(Fig. 5.5 A-B)**. However, the delineation of preserved tissue was not very clear, because the distinction between oedematous, but non necrotic (i.e. potentially preserved) tissue and necrosis is difficult, since both appear as relatively hyper-intense. In addition, this relative hyper-intense signal between the scattered hypo-intensities of the haemorrhage **(e.g. Fig. 5.5 C)** was difficult to interpret (uninjured tissue *versus* oedema *versus* necrosis).
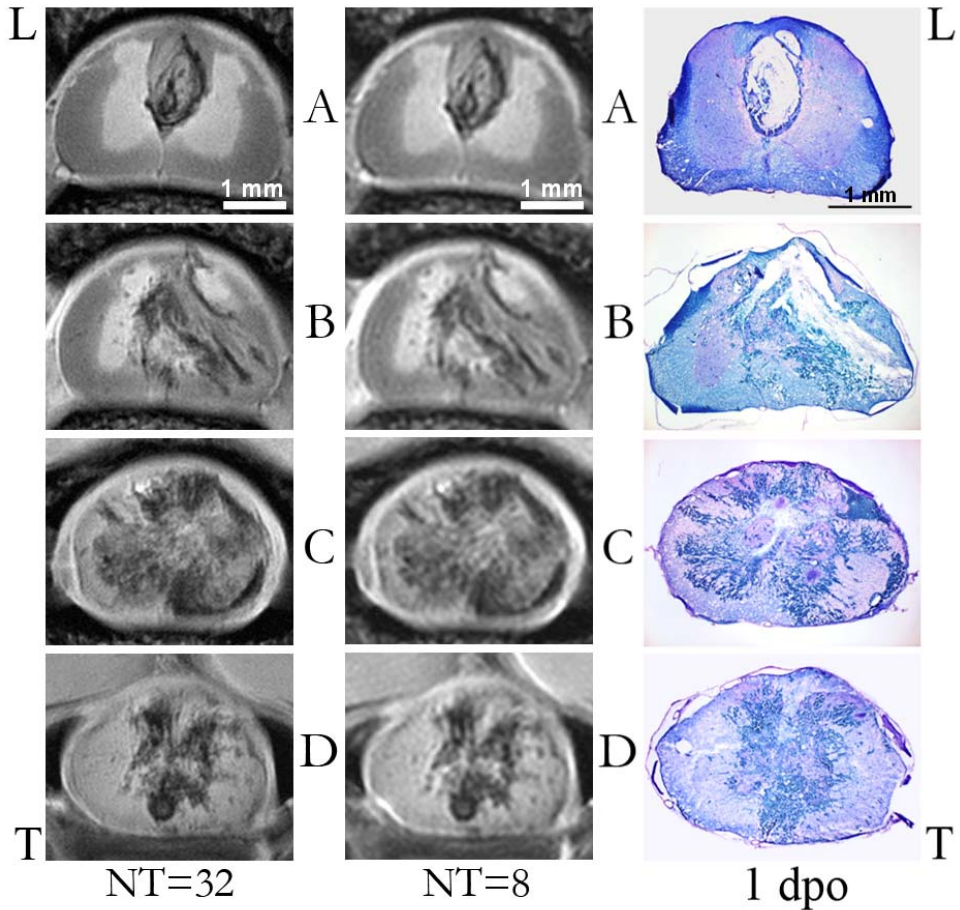
Figure 5.5: Axial sections, high and lower resolution PD MRI (left and middle) compared to histology of an acute cord 1 day post-injury (right, haematoxylin and Luxol Fast Blue). 1 dpo, from lumbar (A) to thoracic (D). Acquisition times were 8-10 hours for NA=32 and 50 minutes for NA=8. Resolution was 38 µm x 38 µm for NA=32 and 68 µm x 68 µm for NA=8. Grey and white matter contrast is preserved in the periphery of the lesion (A, B). Row C shows the lesion centre with massive haemorrhage (hypo-intense) in the grey and white matter. In the more rostral part (row D), the haemorrhage forms mainly in the grey matter, in a characteristic topographic pattern.

Figure 5.6: Example of an acute cord at 7 days post-injury with massive oedema / necrosis detected by MRI (hyper-intense) (A) and histology (B, Haematoxylin, Luxol fast blue): black asterisk. Areas of haemorrhage can also be seen and the topographical correlation is precise (hypo-intense signal, red asterisk). The cord volume is increased at the lesion site: the spinal cord completely fills the spinal canal.
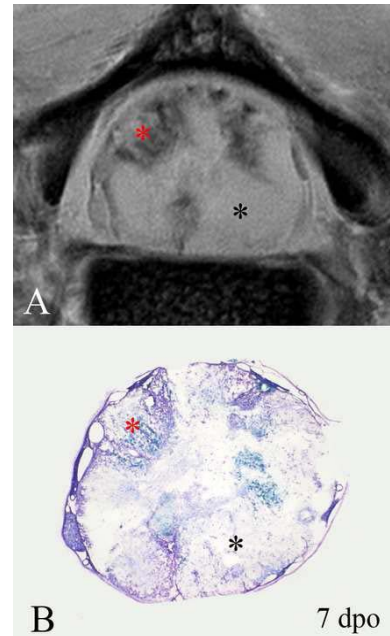
4 to 7 days post-SCI

At four and seven days post-SCI there was major cord swelling. Histological analysis confirmed cord oedema and necrosis, with haemorrhagic areas mainly in the grey matter **(Fig. 5.6)**. At this stage, at the lesion centre, it was impossible to delineate spared peripheral white matter. At the periphery of the lesion, grey matter also appeared swollen and grey-white matter contrast was slightly reduced.

28 days post-SCI and later

At 28 and 56 days post-SCI, the lesion was well circumscribed. The cord's axial diameter had progressively decreased at the lesion centre: from day 14 on, the size of the fluid filled perimedullary subarachnoid space increased. At 56 days, cord atrophy appeared clearly **(Fig. 5.7). Figure 5.8** illustrates the high precision of the lesion detection: the topography of the lesion was well delineated by MRI. The MRI data were congruent with histology. In particular, necrotic areas appeared hyper-intense, except where traces of haemorrhage

were seen (hypo-intense), corresponding to macrophages laden with haemosiderin. Even slight deposits of haemosiderin could be detected. At this chronic stage, preserved tissue was more easily distinguished from the lesion than during the acute phase. Although the cord-spine block of the 5 month survival rat was excised and analysed, the interpretation was hindered by air entry into the canal.
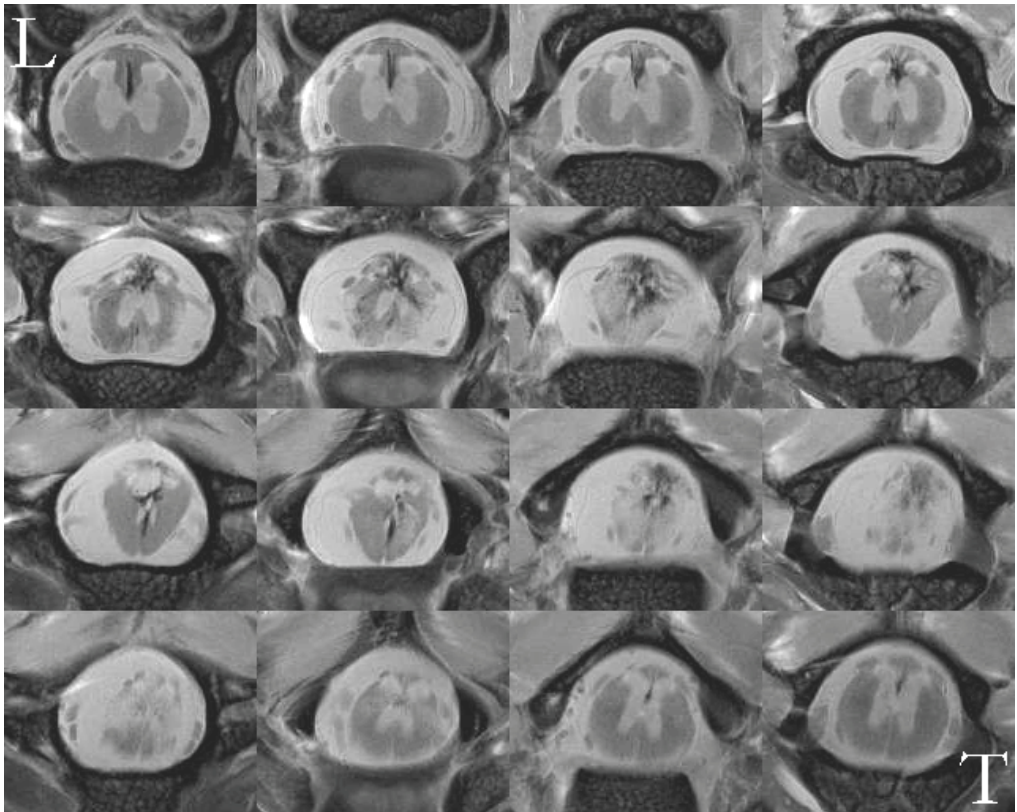
Figure 5.7: PD imaging (NA=32) at 56 dpo, from lumbar (L) to thoracic (T), showing atrophy of the spinal cord over the entire lesion length. Post-MRI histological analyses (not shown) confirmed cord shape and lesion extension, including the rhomboid deformity of the cord, the dorsal cyst in the third row, and the wing shaped lesion periphery towards the thoracic cord (last row, second from the left).
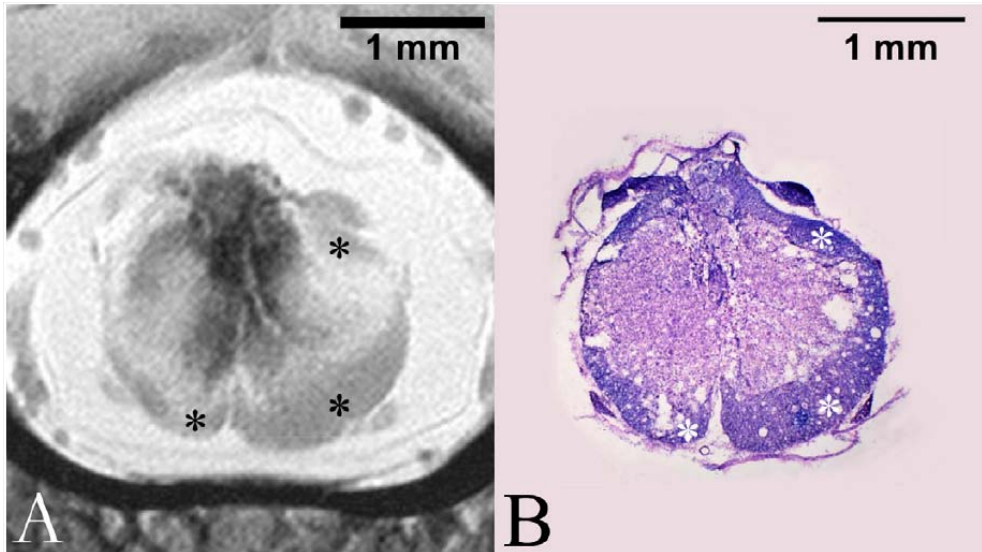
Figure 5.8: Correlation of PD MRI (NA= 32, A) with histology (haematoxylin, Luxol Fast Blue, B) at the lesion site, 28 dpo. MRI shows that the ventral and ventro-lateral funiculi are partially spared by the lesion at this level. The lesion topography, including central hypo-signal/haemosiderin deposits seen at high magnification (not shown), and white matter sparing (asterisks) are congruent. Note that there are histological artefacts in B including the loss of tissue, whereas the MR image shows the necrotic and intact parenchyma completely.

5.3.3 Inversion recovery imaging for selective detection of spared white matter

The interpretation of the presence of preserved white matter was based on the combined analysis of the PD and the IR images (TI = 525 ms). IR images increased the contrast between the now hypo-intense white matter and very discrete white matter changes, almost imperceptible and difficult to interpret on PD images. This was also confirmed by histology in every case **(Fig. 5.9).** These images illustrate the usefulness of inversion-recovery imaging for the detection of white matter damage over the entire length of the spinal cord lesion. Vacuolation of the white matter, which is not detected by the standard PD sequence, appears clearly on the IR images **(Fig. 5.9 row G).** Spared white matter was mainly seen in the ventral and ventro-lateral funiculi. Cord atrophy was severe **(Fig. 5.9 row D)**. Some cords show the presence of a liquid filled cyst (**Fig. 5.9 row F**, hyper-intense**)**. Extensive gliosis (hyper-intense) with evidence for haemorrhage (hypo-intense) was seen at the lesion centre **(Fig. 5.9 rows B, C, and E)**. The topographical correlation between MRI and histology was precise: spinal cord shape, white matter preservation, and lesion extent were congruent **(Fig. 5.9 and 5.12).**

A

B

C

D

E

F

G

PD   IR   (60 dpo)
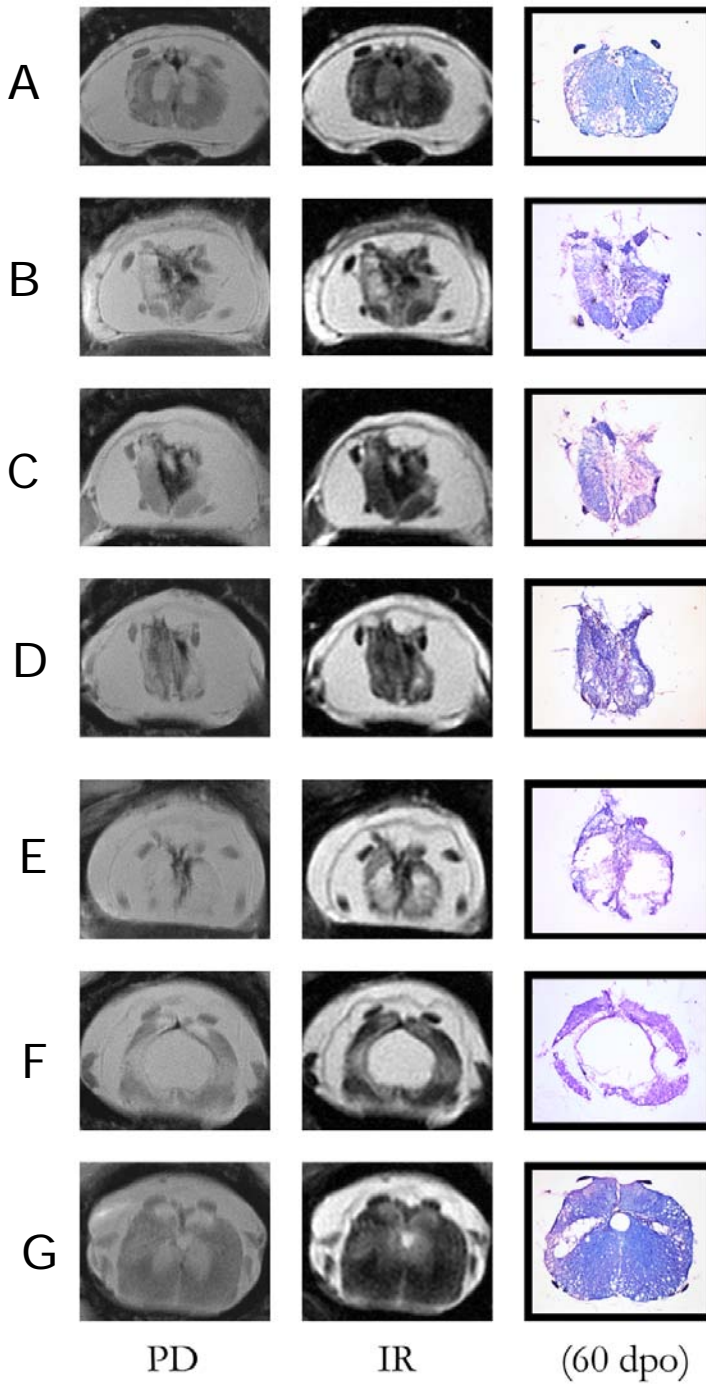
Figure 5.9: Correlation of PD and IR MRI with histology (rat n° 1).

Proton density weighted MRI (left column, resolution 37.8 μm x 37.8 μm per pixel), inversion recovery MRI (middle column, resolution 68 μm x 68 μm per pixel), and histology (right column), from caudal (A) to rostral (G) to compare MRI and histology. A: lumbar extremity of the lesion zone with beginning cord atrophy. The main part of the lesion is seen in the posterior part of the cord, between the two dorsal horns. Some white matter vacuolation can be seen in the periphery. B: The topography of haemosiderin deposits in the centre of the cord (hypo-intense) and of bilateral ventral white matter sparing are matched between MRI and histology. C to E: the progressive atrophic deformation of the cord and the lesion topography are congruent between histology and MRI. F: cystic degeneration of the lesion in the centre of the cord, surrounded by preserved white matter in the lateral funiculi. G: proximal lesion periphery with ventral vacuolation of white matter, and a typical lesion topography with central atrophic scarring resulting in the juxtaposition of the hyper-intense dorsal horns and with a wing shaped extension of the lesion into the lateral cord.

5.3.4 Behavioural recovery after SCI

The locomotor behaviour of five lesioned rats was scored each week during two months **(Fig 5.10)** after SCI. From this graph, three locomotor recovery patterns could be distinguished. In pattern 1, the rats (n°1 and 2) only show limited locomotor recovery. They had an initial low BBB-score and over time the score increased slowly to a medium score of 10. Pattern 2 is an intermediate form. The rat (n°3) started at a low BBB-score but reached a high of score of 21 in about 5 weeks. The third pattern reflects fast recovery (n°4 and 5). The starting BBB-score is around 10 and increases within two weeks to the maximum score of 21 which corresponds to normal over ground locomotion.
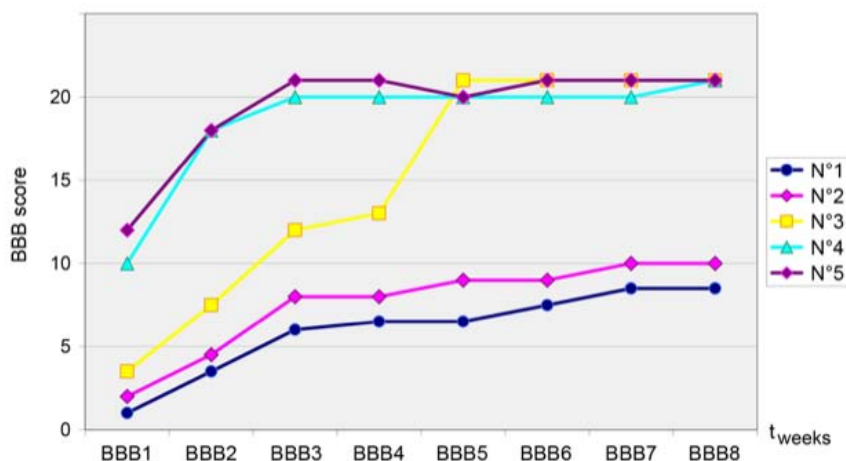
Figure 5.10: BBB evolution over time after SCI. Three different patterns are observed: partial recovery in two rats (plantar placement of the paws in rat n° 1, limited stepping in rat n° 2), slow recovery of the maximum BBB score of 21 in rat n° 3, and rapid recovery to the maximum BBB score of 20-21 in rats n° 4 and n° 5.

5.3.5 Morphometric parameters derived from PD images with support of IR MR-images

The morphometric parameters, which were determined, are the remaining cord area, lesion area, spared white matter and more specific spared ventral white matter **(Table 5.2)**. The evolution of the remaining cord area and the lesion size over the total length of the spinal cord are plotted on a graph **(Fig. 5.11).** The red curve represents the remaining cord area of the spinal cord. To show that atrophy has occurred after two months of recovery, the cord area of a normal spinal cord was measured and plotted (black line). The black curve starts at lumbar level and its value decreases as it reaches thoracic level. The discrepancy between both the red and black curve indicates that the cord has become atrophic. From this graph, the total spared matter can be calculated.
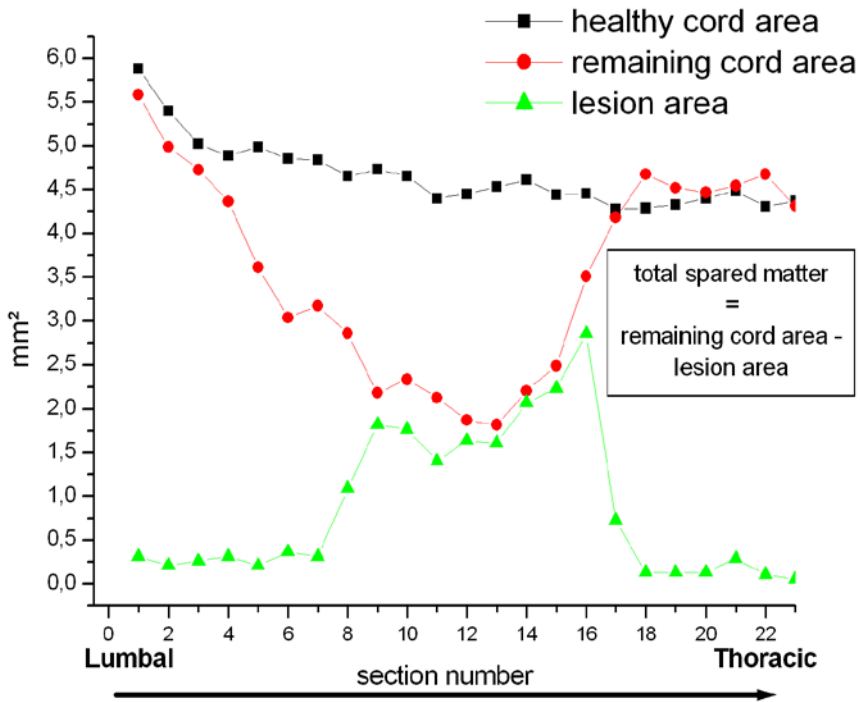
Figure 5.11: Graphical representation of the morphometric analysis on SC tissue (rat n°1). Spinal cord (red curve) area and lesion (green curve) area are measured on each MRI section of the injured spinal cord and depicted on the graph. The area between both of these curves shows the remaining spared matter, i.e. spared white and gray matter. To show the degree of atrophy after 2 months of recovery, the cord area of a normal spinal cord was measured at corresponding locations. The measurements are performed in lumbo-thoracic direction. Legend: L lumbar (sub-lesional area), T thoracic (supra-lesional area).
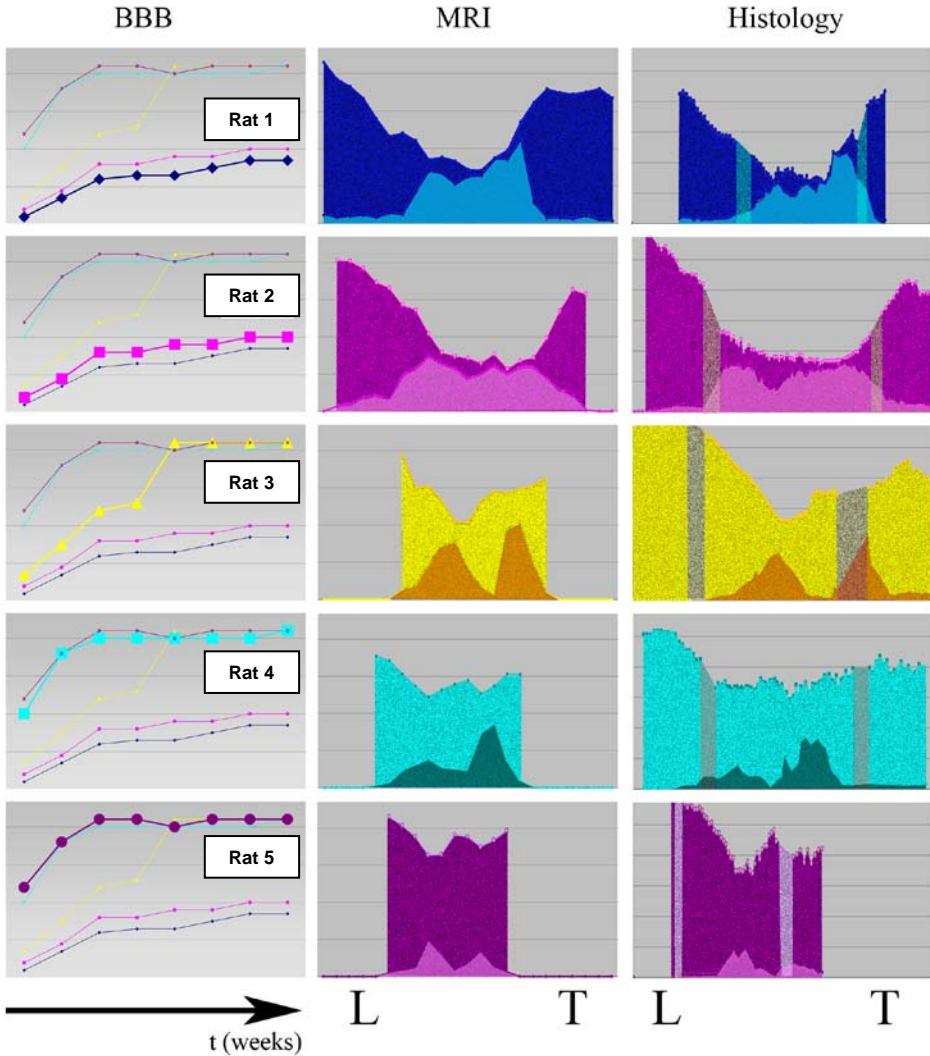
Figure 5.12: Illustrative graph showing the pattern of locomotor recovery (BBB evolution, left column) in the light of the quantity of spared matter / lesion severity measured on the MR images (middle column) **and histology** (right column). In both the MRI and the histology graphs, the upper curves correspond to the cord area measured and the lower curves to the lesion area measured. Despite the absence of a mathematical correlation, this figure shows the expected visual correspondence between severity of the injury and the recovery pattern. The severity of the injury can be appreciated by the "dip" of the upper curve (corresponding to atrophy of the cord due to scarring), the height of the lower curve (corresponding to lesion size), and the distance between the curves (corresponding to spared matter).

The graphical evolution of the cord's area and lesion extent over the complete spinal cord length are illustrated in **figure 5.12**. When confronting morphometry with locomotor recovery, the behavioural expression of lesion severity appears clearly. As expected, the smallest amount of spared matter was seen in rat n°1 and n°2, for which lesion size and atrophy were also higher. The cords of rat n°3, 4 and 5 showed more spared white matter, less atrophy and reduced lesion size **(Fig. 5.12)**. This was confirmed by the quantitative MRI results (for MRI data, see **table 5.2)**.

	N°1	N°2	N°3	N°4	N°5
Lesion volume (µl)	22.33	22.39	15.45	10.74	5.13
Atrophy (minimal cord area: mm²)	1.82	2.13	3.56	3.90	5.46
Minimal spared white matter (mm²)	0.13	0.32	0.96	1.30	2.39
Minimal ventral spared white matter (mm²)	0.07	0.24	0.67	0.91	1.91

Table 5.2: Morphometric parameters derived from PD images supported by IR images. Next to the lesion volume (summed lesion area x 1 mm slice thickness for all slices of a spine block), the evolution of cord area, spared white matter and ventral spared white matter were measured over the complete length of the spinal cord-spine block. For the three latter, the 'minimal area' was measured in the axial 1 mm slice in which the area of the selected parameter was minimal. These minimal values qualitatively correlate with locomotor recovery in rats with spinal cord injury. Lesion volume also provides information about the extent of the tissue damage and seems to qualitatively correlate with functional recovery.

Locomotor recovery of rat n° 3 was asymmetrical. IR MRI showed that, at the lesion's centre, there was extensive white matter sparing in the left half of the cord, with abnormal signal on the entirety of the right half. At the initial BBB evaluations, all joints of the left hind limb showed extensive movement, whereas the right hind limb did not move at all in the first week and then recovered **(Fig. 5.13)**.
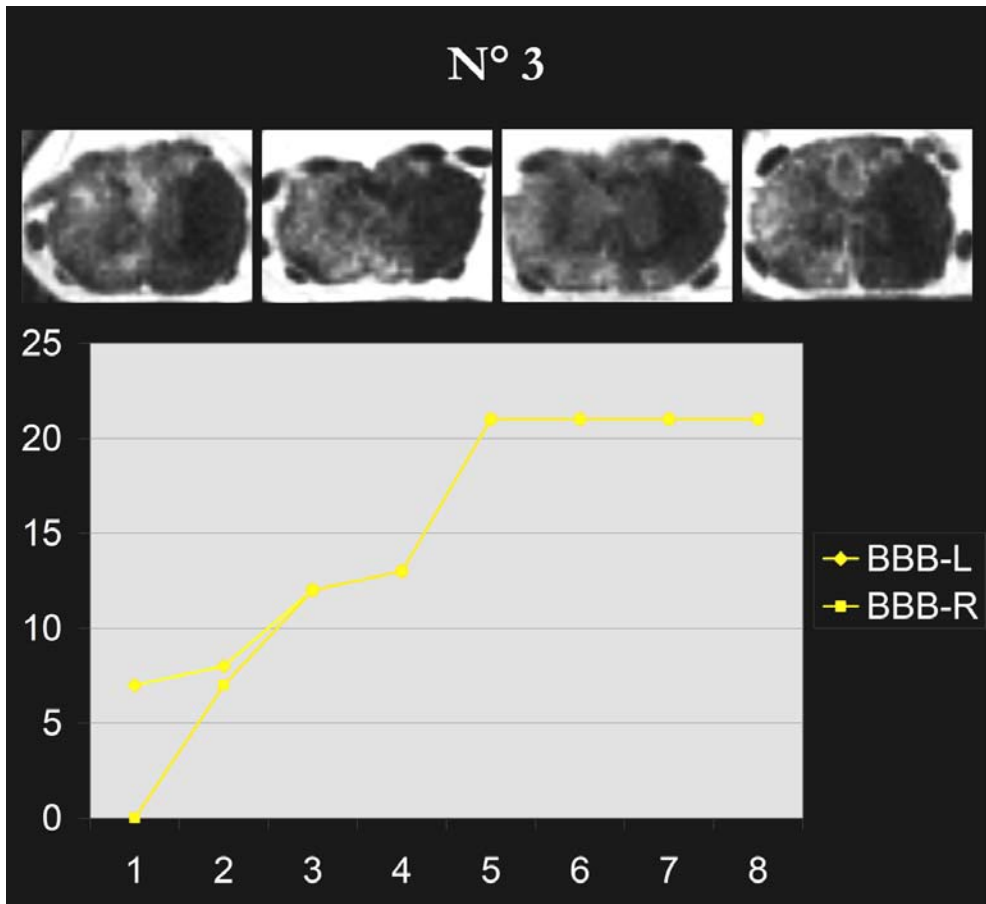
Figure 5.13 Correlation of right and left BBB score evolution in rat n°3. Slower recovery of the right hind limb, which attains the same score as the left after less than a month, ultimately resulting in symmetric recovery up to a normal BBB score of 21. Axial IR images show the maximal lesion extent, with a clear predominance of the lesion on the right side and extensive white matter sparing on the left side, especially in the ventral and lateral funiculi.

5.4 Discussion

In this study, it was preferred not to manipulate the fragile spinal cord tissue and to image the cord in its spine block. PD imaging sequences were used because PD weighting showed excellent contrast in *ex vivo* CNS MRI, by others (Bilgen et al., 2005) and in our own lab (Beuls et al., 1993; Scholtes et al., 2006). The present set-up resulted in rapidly acquired and high quality *post-mortem* images of the spinal cord-spine block, providing different types of information. First of all, the technique showed the unhandled spinal cord within its surrounding structures, allowing the appreciation of global spinal cord changes in its anatomical setting. Second, the spinal cord lesion, in particular its extent in the axial plane, can be micro-anatomically demonstrated. Third, the lesion can be assessed for its histological components. Therefore, the present results indicated that MRI can provide complementary data to the histological analyses – with a number of methodological advantages. The analysis of the cord "*in situ*" (in the spine) in 3 planes, without being physically sectioned or even handled, leaves the parenchyma intact and undistorted for further analysis, but already provides a wealth of information. In the present experimental SCI model in particular, MRI determined the level of the lesion and its extension. Moreover, pathological changes like cord swelling or atrophy could be assessed in relation to the spinal canal (which is difficult with histology where decalcification of the spinal bone would be needed, with a series of technical disadvantages). Furthermore, the "*in situ*" analysis of the cord also allowed precise axial (anterior, posterior, left and right) localisation of pathological changes even in severely injured cords where atrophic changes and scarring often makes anatomical orientation more difficult.

In that perspective, the MRI assessment of the anatomical lesion extent provided information about the anatomy of spared cord parenchyma. This is of major importance after experimental SCI, because the assessment of experimental treatment strategies is based on their effect on locomotor recovery, and locomotor recovery depends on spinal cord white matter sparing (Basso et al., 2002; Loy et al., 2002a). The latter is, based on our data, best

assessed in the axial plane, where one can gather precise information about the maximal extension of the lesion and microanatomy of white matter damage (Schucht et al., 2002; You et al., 2003). In this respect, our investigation differs from published work with comparable image quality (Weber et al., 2006), where MRI and histology were correlated in longitudinal sections. Although this depicts many aspects of the cord lesion, it does not provide the same type of information.

Also lesion components were depicted using PD weighting. Haemorrhage was hypo-intense from dpo 1 to dpo 60; confirming the literature (Falconer et al., 1994; Hackney et al., 1994). Oedema and necrosis / scarring processes were shown as hyper-intensities but could not be distinguished with the present acquisition sequences. The evolution of the spinal cord lesion could be followed using as little as two to three rats per survival group, in addition to the evolution of cord swelling and atrophy: during the first week, the cord completely fills the spinal canal at the lesion level, then the volume regresses and the scarring processes result in atrophy. The observed oedema-necrosis-scarring sequence confirmed previous MRI studies with lower resolution, but with Gadolinium contrast injection (Runge et al., 1997). It also appears from these images that precise MRI lesion analysis with useful delimitation of the lesion extension and estimation of cord atrophy is only possible after, at least, two to three weeks. These assessments could be extended to other experimental SCI models, or even to other rodent species as recently proposed (Bilgen et al., 2007). Various lesion models have been used to induce contusive or compressive spinal cord injury (Basso et al., 1996; Martin et al., 1992; Rivlin and Tator, 1978), of which the type of impact is different resulting in varying topography of injury (Choo et al., 2007). However, these different techniques have never been precisely compared side to side for the sequence of pathological events. *Post-mortem* MRI has the potential for less laborious comparisons of the temporal evolution of acute and chronic processes in different lesion models, e.g., the locomotor patterns may be functionally restructured under unilateral long tract progressive atrophy appearing from 14 dpo on, which has been described and quantified before (Deng et al., 2007). This may provide insight into the comparability of

these different approaches which have been used more or less randomly in the past in SCI research.

In addition to the biological information and from the technical viewpoint, MRI compares favourably to histology. We have found that even the lower resolution PD images (68 x 68 µm) acquired with a NA=8 and even NA=4, are sufficient to depict the spinal cord lesion's topography, and particularly to assess damage to the white matter tracts, because the key tracts involved in locomotion are diffusely distributed in the ventral and lateral funiculi (Harris et al., 1994; Loy et al., 2002b). Therefore, the possibility for rapid tissue analysis (less than half an hour) with the lower resolution protocol offers a high potential in SCI research, e.g. for rapid inter-rat lesion comparison, in order to assess the homogeneity of lesion severness in operated experimental groups.

Limitations of the set-up used include the difficulty to distinguish necrosis (i.e., definitive tissue injury) from oedema (i.e. reversible tissue injury), known to occur at the acute stage. A further limitation, as for histology, is the *ex vivo* design of the study. Any single spinal cord can only be analysed at one time point and conclusions concerning the sequential pathological events are derived from the observation of different cords. It is obvious that *in vivo* MRI has the potential to take these results further and, in particular, to allow follow-up of the same rat / the same lesion over time. This may allow better interpretation of early post-SCI MRI data and, e.g. confirm haemorrhage as a prognostic indicator for lesion severity like in humans (Flanders et al., 1999; Miyanji et al., 2007). However, in order to obtain useful *in vivo* image resolutions, invasive techniques like coil implantations (Bilgen et al., 2001) or high field magnets (Behr et al., 2004) have to be used, the latter becoming more and more accessible. Of course, attention has to be paid to respiratory and heart-rate coupling and anaesthesia to reduce the mortality risk in these small rodents (Weber et al., 2006).

This investigation also showed that IR MRI offers a strong support to fast, medium resolution PD MR images since it allows to visualize the spared white

matter selectively. Each tissue has a specific T1-relaxation decay time due to the specific degree of structuration of the tissue. With IR imaging, one can selectively "remove" the signal from a specific tissue by choosing a well-selected inversion recovery time (TI) in the IR sequence. This results in a very hypo-intense signal intensity for the corresponding tissue in the image, i.e. the normal spared white matter in this thesis. PD and IR images were used simultaneously to define a very hypo-intense IR signal as spared white matter when this hypo-intensity was not seen in the PD images. Hypo-intensities present in IR as well as in PD images were considered to be due to the presence of iron, i.e. secondary to haemorrhage. Histology confirmed that IR enhanced the detection of pathological changes in white matter. The technique reveals even discrete white matter changes, like vacuolation in the descending white matter tracts. The functional significance of these discrete changes is not clearly established, but the possibility to detect them by IR MRI demonstrates the latter's diagnostic precision. This is highly important since white matter sparing is a key factor with respect to locomotor recovery after SCI (Basso, 2000; Schucht et al., 2002).

In a small group of rats with clearly different lesion intensities, the quantitative information provided by IR supported PD MRI regarding white matter sparing as well as the other morphometric parameters assessed, i.e. lesion size and cord atrophy, compared well with the locomotor recovery patterns: rats with the least amount of white matter sparing performed worst, and vice versa. Preservation of ventral, ventro-lateral and dorso-lateral white matter at the level of maximal lesion extent was associated with rapid recovery of normal basic open field locomotion, confirming previous results (Loy et al., 2002b). Even moderate sparing of a lateral funiculus was sufficient to promote functional recovery up to a score of 21. From initially asymmetric locomotion, the progressive recovery of the weaker limb over one month (i.e. the time period known to be necessary for locomotor stabilization (Martin et al., 1992; Multon et al., 2003) confirms that, despite the complete damage to the ipsilateral cord, the sublesional locomotor patterns may be functionally restructured under unilateral long tract influence (Bareyre et al., 2004; Webb and Muir, 2004). Moderate locomotor recovery observed in rats n° 1 and n° 2 was associated with minimal sparing in the

ventral funiculus. These data, obtained from a limited series of five rats, illustrate the wealth of information that can potentially be obtained by IR-supported PD imaging of the spinal cord-spine block, including the precise micro-anatomical assessment of white matter damage with high efficiency in terms of acquisition speed, contrast, SNR and resolution. The combination of a rapidly acquired PD weighted image and a "low resolution" IR image (e.g. 100 x 100 μm per pixel, which could be obtained in about 1hour with NA=4) may provide similarly high diagnostic accuracy and should be the subject of future studies. The latter should be carried out on larger experimental groups with more homogenous lesions, in order to determine the true "behavioural" sensitivity of the technique.

5.5 Conclusions

The present investigation has demonstrated that *post-mortem* SCI MRI efficiently provides useful information regarding lesion severity and progression over time and shows the precision of preserved white matter detection in its anatomical setting. It showed the evolution of the injured SC over time – from acute to chronic stage – and correlated it with the histological sequence of events. However, it was not possible to distinguish oedema from necrosis in the acute stage after SCI using the MRI contrast settings as described here. This might be a challenge for future research. This research work provided evidence that the MR imaging technique holds promise for the detection of white matter sparing and the prediction of locomotor outcome in the experimental setting. The extent of this correlation needs to be investigated further in the future and it should be attempted to transfer the described set-up to the *in vivo* setting. In addition, parameters were determined for efficient MR imaging in terms of (1) image acquisition time and (2) quality of the MR image. In the setting of SCI, "image quality" means: demonstration of lesion components, delineation of the lesion and, as a correlate, detection and localization of spared spinal cord parenchyma.

References

Ackery A, Tator C, Krassioukov A. 2004. A global perspective on spinal cord injury epidemiology. Journal of neurotrauma 21(10):1355-1370.

Bareyre FM, Kerschensteiner M, Raineteau O, Mettenleiter TC, Weinmann O, Schwab ME. 2004. The injured spinal cord spontaneously forms a new intraspinal circuit in adult rats. Nature neuroscience 7(3):269-277.

Basso DM. 2000. Neuroanatomical substrates of functional recovery after experimental spinal cord injury: implications of basic science research for human spinal cord injury. Physical therapy 80(8):808-817.

Basso DM, Beattie MS, Bresnahan JC. 1996. Graded histological and locomotor outcomes after spinal cord contusion using the NYU weight-drop device versus transection. Experimental neurology 139(2):244-256.

Basso DM, Beattie MS, Bresnahan JC. 2002. Descending systems contributing to locomotor recovery after mild or moderate spinal cord injury in rats: experimental evidence and a review of literature. Restorative neurology and neuroscience 20(5):189-218.

Behr VC, Weber T, Neuberger T, Vroemen M, Weidner N, Bogdahn U, Haase A, Jakob PM, Faber C. 2004. High-resolution MR imaging of the rat spinal cord in vivo in a wide-bore magnet at 17.6 Tesla. Magma 17(3-6):353-358.

Behrmann DL, Bresnahan JC, Beattie MS, Shah BR. 1992. Spinal cord injury produced by consistent mechanical displacement of the cord in rats: behavioral and histologic analysis. Journal of neurotrauma 9(3):197-217.

Beuls E, Gelan J, Vandersteen M, Adriaensens P, Vanormelingen L, Palmers Y. 1993. Microanatomy of the excised human spinal cord and the cervicomedullary junction examined with high-resolution MR imaging at 9.4 Tesla. American journal of neuroradiology 14(3):699-707.

Bilgen M, Abbe R, Liu SJ, Narayana PA. 2000. Spatial and temporal evolution of hemorrhage in the hyperacute phase of experimental spinal cord injury: in vivo magnetic resonance imaging. Magnetic resonance in medicine 43(4):594-600.

Bilgen M, Abbe R, Narayana PA. 2001. Dynamic contrast-enhanced MRI of experimental spinal cord injury: in vivo serial studies. Magnetic resonance in medicine 45(4):614-622.

Bilgen M, Al-Hafez B, Alrefae T, He YY, Smirnova IV, Aldur MM, Festoff BW. 2007. Longitudinal magnetic resonance imaging of spinal cord injury in mouse: changes in signal patterns associated with the inflammatory response. Magnetic resonance imaging 25(5):657-664.

Bilgen M, Al-Hafez B, Malone TM, Smirnova IV. 2005. Ex vivo magnetic resonance imaging of rat spinal cord at 9.4 T. Magnetic resonance imaging 23(4):601-605.

Bilgen M, Peng W, Al-Hafez B, Dancause N, He YY, Cheney PD. 2006. Electrical stimulation of cortex improves corticospinal tract tracing in rat spinal cord using manganese-enhanced MRI. Journal of neuroscience methods 156(1-2):17-22.

Carvlin MJ, Asato R, Hackney DB, Kassab E, Joseph PM. 1989. High-resolution MR of the spinal cord in humans and rats. American journal of neuroradiology 10(1):13-17.

Choo AM, Liu J, Lam CK, Dvorak M, Tetzlaff W, Oxland TR. 2007. Contusion, dislocation, and distraction: primary hemorrhage and membrane permeability in distinct mechanisms of spinal cord injury. Journal of neurosurgery 6(3):255-266.

Deng X, Ramu J, Narayana PA. 2007. Spinal cord atrophy in injured rodents: high-resolution MRI. Magnetic resonance in medicine 57(3):620-624.

Falconer JC, Narayana PA, Bhattacharjee MB, Liu SJ. 1994. Quantitative MRI of spinal cord injury in a rat model. Magnetic resonance in medicine 32(4):484-491.

Flanders AE, Spettell CM, Friedman DP, Marino RJ, Herbison GJ. 1999. The relationship between the functional abilities of patients with cervical spinal cord injury and the severity of damage revealed by MR imaging. American journal of neuroradiology 20(5):926-934.

Gensel JC, Tovar CA, Hamers FP, Deibert RJ, Beattie MS, Bresnahan JC. 2006. Behavioral and histological characterization of unilateral cervical spinal cord contusion injury in rats. Journal of neurotrauma 23(1):36-54.

Hackney DB, Finkelstein SD, Hand CM, Markowitz RS, Black P. 1994. Postmortem magnetic resonance imaging of experimental spinal cord injury: magnetic resonance findings versus in vivo functional deficit. Neurosurgery 35(6):1104-1111.

Harris RM, Little JW, Goldstein B. 1994. Spared descending pathways mediate locomotor recovery after subtotal spinal cord injury. Neuroscience letters 180(1):37-40.

Ichihara K, Taguchi T, Sakuramoto I, Kawano S, Kawai S. 2003. Mechanism of the spinal cord injury and the cervical spondylotic myelopathy: new approach based on the mechanical features of the spinal cord white and gray matter. Journal of neurosurgery 99(3 Suppl):278-285.

Ichihara K, Taguchi T, Shimada Y, Sakuramoto I, Kawano S, Kawai S. 2001. Gray matter of the bovine cervical spinal cord is mechanically more rigid and fragile than the white matter. Journal of neurotrauma 18(3):361-367.

Loy DN, Magnuson DS, Zhang YP, Onifer SM, Mills MD, Cao QL, Darnall JB, Fajardo LC, Burke DA, Whittemore SR. 2002a. Functional redundancy of ventral spinal locomotor pathways. Journal of neuroscience 22(1):315-323.

Loy DN, Talbott JF, Onifer SM, Mills MD, Burke DA, Dennison JB, Fajardo LC, Magnuson DS, Whittemore SR. 2002b. Both dorsal and ventral spinal cord pathways contribute to overground locomotion in the adult rat. Experimental neurology 177(2):575-580.

Martin D, Schoenen J, Delree P, Gilson V, Rogister B, Leprince P, Stevenaert A, Moonen G. 1992. Experimental acute traumatic injury of the adult rat spinal cord by a subdural inflatable balloon: methodology, behavioral analysis, and histopathology. Journal of neuroscience research 32(4):539-550.

Matesz C, Bacskai T, Nagy E, Halasi G, Kulik A. 2002. Efferent connections of the vestibular nuclei in the rat: a neuromorphological study using PHA-L. Brain research bulletin 57(3-4):313-315.

Mihai G, Nout YS, Tovar CA, Miller BA, Schmalbrock P, Bresnahan JC, Beattie MS. 2008. Longitudinal comparison of two severities of unilateral cervical spinal cord injury using magnetic resonance imaging in rats. Journal of neurotrauma 25(1):1-18.

Miyanji F, Furlan JC, Aarabi B, Arnold PM, Fehlings MG. 2007. Acute cervical traumatic spinal cord injury: MR imaging findings correlated with neurologic outcome--prospective study with 100 consecutive patients. Radiology 243(3):820-827.

Moriarty LJ, Duerstock BS, Bajaj CL, Lin K, Borgens RB. 1998. Two- and three-dimensional computer graphic evaluation of the subacute spinal cord injury. Journal of the neurological sciences 155(2):121-137.

Multon S, Franzen R, Poirrier AL, Scholtes F, Schoenen J. 2003. The effect of treadmill training on motor recovery after a partial spinal cord compression-injury in the adult rat. Journal of neurotrauma 20(8):699-706.

Olby NJ, Blakemore WF. 1996. A new method of quantifying the extent of tissue loss following spinal cord injury in the rat. Experimental neurology 138(1):82-92.

Priebe MM, Chiodo AE, Scelza WM, Kirshblum SC, Wuermser LA, Ho CH. 2007. Spinal cord injury medicine. 6. Economic and societal issues in spinal cord injury. Archives of physical medicine and rehabilitation 88(3 Suppl 1):S84-88.

Rivlin AS, Tator CH. 1978. Effect of duration of acute spinal cord compression in a new acute cord injury model in the rat. Surgical neurology 10(1):38-43.

Runge VM, Wells JW, Baldwin SA, Scheff SW, Blades DA. 1997. Evaluation of the temporal evolution of acute spinal cord injury. Investigative radiology 32(2):105-110.

Scholtes F, Adriaensens P, Storme L, Buss A, Kakulas BA, Gelan J, Beuls E, Schoenen J, Brook GA, Martin D. 2006. Correlation of postmortem 9.4 tesla magnetic resonance imaging and immunohistopathology of the human thoracic spinal cord 7 months after traumatic cervical spine injury. Neurosurgery 59(3):671-678.

Scholtz CL. 1977. Quantitative histochemistry of myelin using Luxol Fast Blue MBS. The histochemical journal 9(6):759-765.

Schucht P, Raineteau O, Schwab ME, Fouad K. 2002. Anatomical correlates of locomotor recovery following dorsal and ventral lesions of the rat spinal cord. Experimental neurology 176(1):143-153.

Sekhon LH, Fehlings MG. 2001. Epidemiology, demographics, and pathophysiology of acute spinal cord injury. Spine 26(24 Suppl):S2-12.

Tyszka JM, Fraser SE, Jacobs RE. 2005. Magnetic resonance microscopy: recent advances and applications. Current opinion in biotechnology 16(1):93-99.

Webb AA, Muir GD. 2004. Course of motor recovery following ventrolateral spinal cord injury in the rat. Behavioural brain research 155(1):55-65.

Weber T, Vroemen M, Behr V, Neuberger T, Jakob P, Haase A, Schuierer G, Bogdahn U, Faber C, Weidner N. 2006. In vivo high-resolution MR imaging of neuropathologic changes in the injured rat spinal cord. American journal of neuroradiology 27(3):598-604.

You SW, Chen BY, Liu HL, Lang B, Xia JL, Jiao XY, Ju G. 2003. Spontaneous recovery of locomotion induced by remaining fibers after spinal cord transection in adult rats. Restorative neurology and neuroscience 21(1-2):39-45.

Chapter 6

Applying the MRI reference frame to study the infiltration kinetics of SPIO labeled immune cells in the EAE animal model for MS

In collaboration with Dr. Baeten Kurt in the frame of his PhD work

Outline chapter 6

6.1 Introduction

6.1.1 Etiology and disease mechanism of MS

6.1.2 Experimental autoimmune encephalomyelitis and MRI

6.1.3 General goals of this study

6.2 Materials and methods

6.3 Results and discussion

6.3.1 Kinetics of macrophage infiltration

6.3.2 Kinetics of myelin reactive T cell infiltration in healthy and EAE rats

6.4 Conclusions

6.1 Introduction

Multiple sclerosis (MS) is the most common neurological impairment among young adults worldwide (Kornek and Lassmann, 1999). The underlying immunological mechanisms leading to myelin destruction and oligodendrocyte damage are still not well understood. To further unravel the role of the immune system in the disease pathogenesis more information has to be gathered on the migration patterns of the different immune cell subsets. To develop new treatment strategies for MS, it is of great importance to understand the underlying disease mechanisms. Therefore, knowledge about the underlying immunopathology can be acquired by using animal models which mimic the disease features (Ben-Chetrit and Brocke, 2005). Tracking of immune cell subsets by means of MRI can provide information about sequential events underlying the immunopathogenesis of MS.

6.1.1 Etiology and disease mechanism of MS

Multiple sclerosis (MS) is an auto-immune disease of the central nervous system, characterised by inflammation, demyelinating lesions and axonal degeneration. For most patients the disease course is characterized by episodes of neurological impairment followed by periods of recovery (Hauser and Oksenberg, 2006). Finally, most of the patients will suffer from progressive disability. Currently there are only immunomodulatory treatments available that influence the disease course by their impact on the inflammation.

Although the exact cause of MS is still unknown, it is generally accepted that pro-inflammatory myelin reactive CD4+ T-cells play an important role. This is supported by the high amounts of these cells present in the peripheral blood and in brain lesions (Merrill, 1992). These myelin reactive T cells are probably initially activated in the periphery via molecular mimicry, i.e. infectious agents present epitopes which share similarities with CNS self-antigens (Fujinami et al., 2006).

Once activated, autoreactive T cells expand and traffic to the CNS. Upon entering into the CNS, the autoreactive T-cells are confronted with CNS self-antigens which are presented by microglia or perivascular macrophages. After reactivation of myelin reactive T cells, adhesion molecules are up-regulated and chemokines are secreted, which results in the attraction of secondary effector cells like macrophages (Esiri and Reading, 1987). This is supported by the fact that secondary effector cells like CD8+ T cells and macrophages are present in brain lesions (Crawford et al., 2004).

6.1.2 Experimental autoimmune encephalomyelitis and MRI

Different models reflect specific aspects of the disease, but no model represents all the aspects of MS. The myelin protein induced EAE model is most commonly used. Depending on the animal strain and myelin protein used, the disease follows either an acute monophasic course or a chronic relapsing course. The EAE model mainly represents the inflammatory aspects of MS, although chronic models also present demyelination and axonal injury.

In EAE, the disease is elicited by injecting myelin antigens in combination with an adjuvant to activate myelin reactive T cells in the periphery. Once the myelin reactive T cells have crossed the blood brain barrier, they become reactivated in the CNS by microglia presenting self-antigens. The activated T cells produce Th1 cytokines and chemokines that attract secondary effector cells such as macrophages and microglia. It is clear that several types of immune cells play a role in the disease course and contribute to the damaging of the CNS (Karpus and Ransohoff, 1998).

To study the role of the different subsets of immune cells, magnetic resonance imaging (MRI) in combination with super paramagnetic contrast particles like SPIO and USPIO (small and ultra small particles of iron oxide) can be applied. These small particles of dextran-coated iron oxide are known to enhance the T2 relaxation of proton nuclei in close proximity of these labeled cells (Stark et al.,

1988). Such particles are either spontaneously taken up by phagocytic cells or can be used to label non-phagocytic cells upon the addition of cationic transfections agents, such as poly-L-lysine (PLL), Superfect or protamine sulphate (Bulte and Kraitchman, 2004). On T2 weighted MR images, the labeled cells are expected to show very hypo-intense signal intensities and so allow to monitor cell migration during disease.

6.1.3 Main goals of this EAE study

In this chapter, the kinetics of the infiltration of macrophages and myelin reactive T cells into the CNS during the EAE disease course are investigated using MRI. Hereto, labeled immune cells are tracked and visualized at different time points during disease to acquire information about their migration pattern.

To reach these goals, images were compared to the corresponding images of the reference frame of the rat's CNS, as discussed in chapter 3, in order to detect hypo-intense regions due to the presence of SPIO labeled immune cell subtypes.

6.2 Materials and methods

The protocols on the EAE induction, disease course and scoring, generation of myelin reactive T cells, cell labelling and imaging are extensively described by Dr. Baeten Kurt in his doctoral thesis: "Magnetic resonance based imaging of immune cells in EAE", 2009 (Baeten, 2009) . Only a brief summary is provided in this thesis.

Kinetics of macrophage infiltration

Imaging experiments were conducted on immunised rats intravenously injected with USPIO (Sinerem 600 µmol Fe/kg; Guerbet, France) at different time points during disease: at disease onset (n=4), top of the disease (n=4) or at clinical recovery (n=4). Twenty-four hours after USPIO injection, animals were sacrificed by decapitation and MRI images of the CNS were acquired. Furthermore, USPIO was administrated to EAE animals at disease onset followed by MRI either at disease top (n=4) or at clinical recovery (n=4).

Kinetics of myelin reactive T cells infiltration

Myelin reactive T cells were labeled *in vitro* with 400 µg Fe/ml (Endorem 11,2 mg/ml; Guerbet, France) and 1 µg PLL/ml (MW > 300 000; Sigma-Aldrich, Belgium). This SPIO/PLL ratio leads to a high intracellular iron content and minimal free SPIO/PLL aggregates. The labeled cells were intraperitoneally injected in naive rats (n=2) or at the onset of disease (n=2) in actively immunised animals. Three to four days after transfer, rats were sacrificed by decapitation and MRI was performed.

Magnetic resonance imaging

Images were acquired in a 25 mm birdcage coil on a Varian Inova 400 spectrometer (Varian, Nuclear Magnetic Resonance Instruments, Palo Alto, California, USA) operating at 9.4 T by using the multislice spin-warp technique. The consecutive T2 weighted (TR = 2500 ms, TE = 65 ms) brain images had a slice thickness of 1 mm, a field of view of 25 x 25 mm and an in-plane resolution of 62.5 x 62.5 µm. For the spinal cord, coronal images of 1 mm slice thickness were acquired with an in-plane resolution of 43.3 x 43.3 µm and a field over view of 13 x 13 mm.

Histology

Immediately after MRI, brains and spinal cords were dissected, embedded in OCT compound 4583 and flash frozen on liquid nitrogen. Frozen sections of 10 µm were used for detection of SPIO particles and T cell infiltrates. The presence of iron was detected with a Prussian blue staining (60 minutes in Perls' solution containing 5% HCl and 5% potassium ferrocyanide) followed by a nuclear fast red counterstain (Klinipath, Belgium). For immunohistochemistry, a biotinylated anti-CD3 antibody was used to detect T cell infiltrates (1:20, Serotec, UK). Binding of the primary antibody was revealed by either avidin-biotin-peroxidase with reagent supplied by Vector laboratories or by Streptavidin Alexa-Fluor 488 conjugate (Molecular Probes, Invitrogen, The Netherlands). The presence of dextran coated SPIO particles was detected using the primary mouse anti-dextran antibody (StemCell Technologies, Vancouver, Canada) and the goat anti-mouse 555 (Molecular Probes, Invitrogen, The Netherlands) as secondary antibody. Images were taken using a Nikon eclipse 80i microscope (Nikon).

6.3 Results and discussion

Post-mortem high resolution MR images were obtained from EAE rats after injection with USPIO or with labeled myelin reactive T-cells. In order to detect abnormal hypo-intense signal intensities, caused by the contrast particles and therefore representing the immune cells of interest, the acquired images were compared to the images of the reference frame, which are shown in detail in chapter 3.

6.3.1 Kinetics of macrophage infiltration

The spatio-temporal distribution of macrophages was visualized by injecting USPIO at various time points during the disease course, i.e. onset, top and recovery phase. Twenty-four hours after the injection, post-mortem MR images were obtained and analysed. As an example, **figure 6.1 A** shows consecutive MR images of an EAE animal which was injected with USPIO at top of the disease. As compared to control images **(Fig. 6.1 B)**, hypo-intense signal alterations can be detected in the diencephalon (see chapter 3 for annotation). To analyse the local amount of USPIO loaded cells, the hypo-intensity was quantified in the main affected regions which are indicated by the green lines in **figure 6.1 A**. Results show that at disease onset most of the hypo-intense areas are located in the caudal part of the brainstem **(Fig. 6.1 C: slices 1-3)** whereas at the top of the disease, these are mainly seen in the midbrain **(Fig. 6.1 C: slices 6-8)**. During the recovery phase, no specific hypo-intense areas can be detected. In combination with additional histochemical analyses, it could be concluded that the hypo-intense areas mainly represent peripheral macrophages that infiltrate in the time frame between USPIO injection and MR imaging.

As a conclusion, the infiltration pattern of macrophages during disease course occurs in a caudo-rostral pattern as it starts in the caudal part of the brainstem and shifts to more rostrally located regions as the disease progresses.
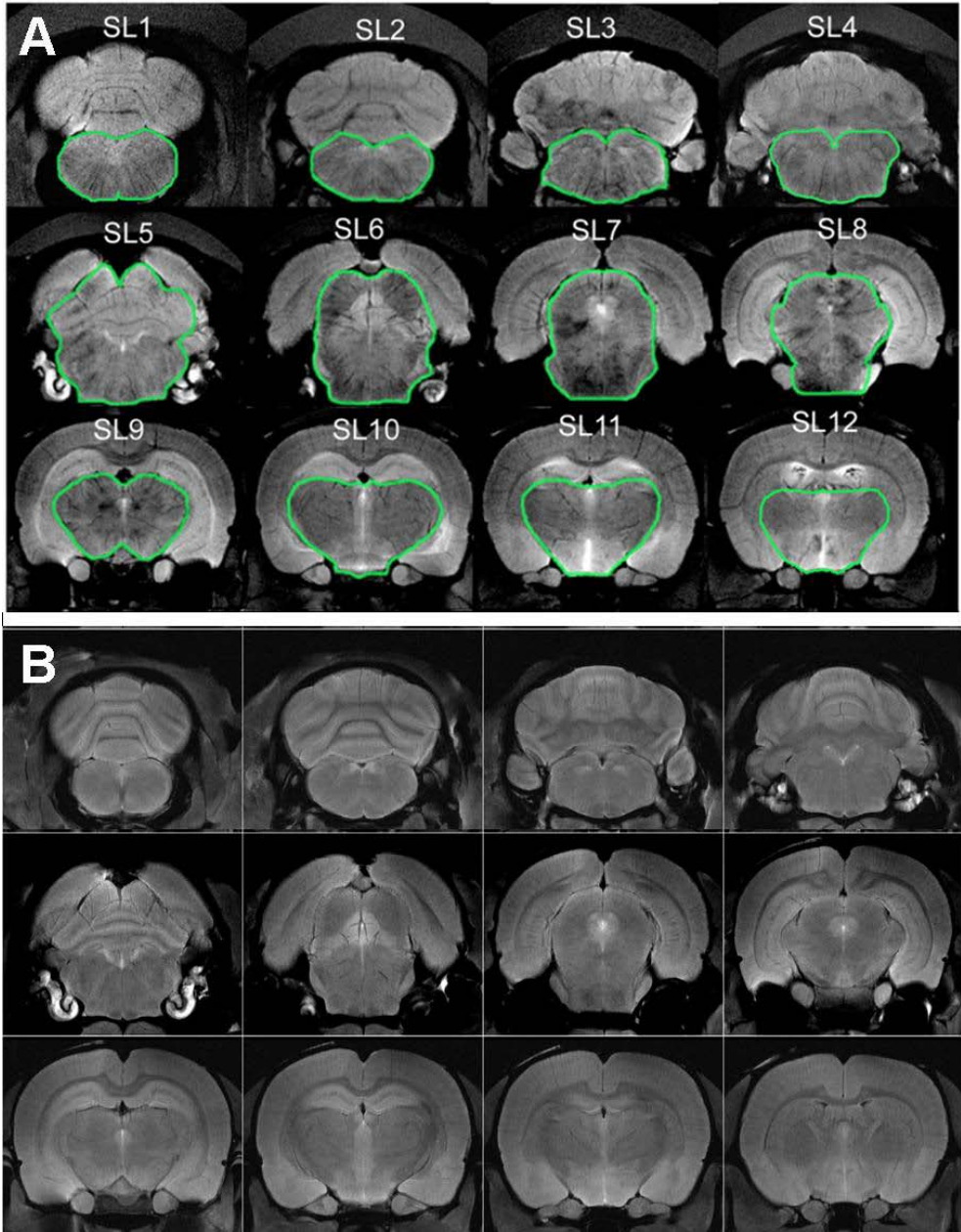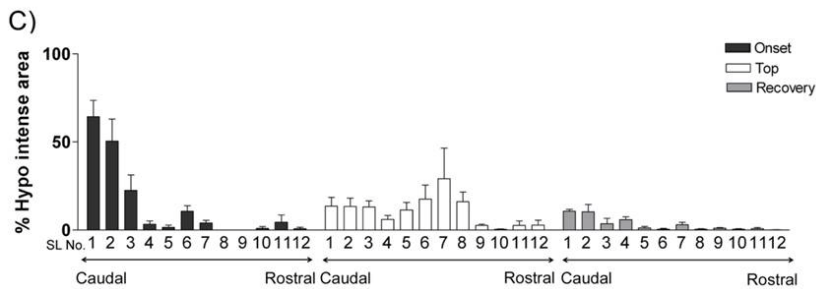
Figure 6.1: Spatio-temporal distribution of macrophage infiltration in the brain during EAE. USPIO was injected at different time points (i.e. onset, top and recovery) of the disease course of EAE followed by MRI of the animals 24h later. An example of an EAE rat injected at top of disease and imaged 24h later is shown (A). The green lines define the regions which are mainly affected. During the disease progress hypo-intense spots, representing USPIO labeled macrophages, can be detected in these regions as compared to healthy rats (B). Quantifying hypo-intense areas at different time points shows a changing distribution of signal attenuation (C).

6.3.2 Kinetics of infiltration of myelin reactive T cells in healthy and EAE rats

In order to study the migration pattern of myelin reactive T cells in the CNS of naive rats, SPIO labeled myelin reactive T cells were transferred to healthy animals and MRI was performed when symptoms as tail and hindlimb paralysis occurred, i.e. after three or four days. As compared to control images **(Fig. 6.2 A)**, MR images of the brain and spinal cord depict hypo-intense areas in the lower part of the spinal cord whereas no hypo-intense signals could be detected in the brain or in the rostral parts of the spinal cord **(Fig. 6.2 B).** When labeled myelin reactive T cells were transferred to an EAE animal at the onset of the disease and subjected to MRI after three or four days, hypo-intense areas can be seen in the caudal part of the spinal cord as well as in the regions of the brainstem **(Fig. 6.2 C)**.
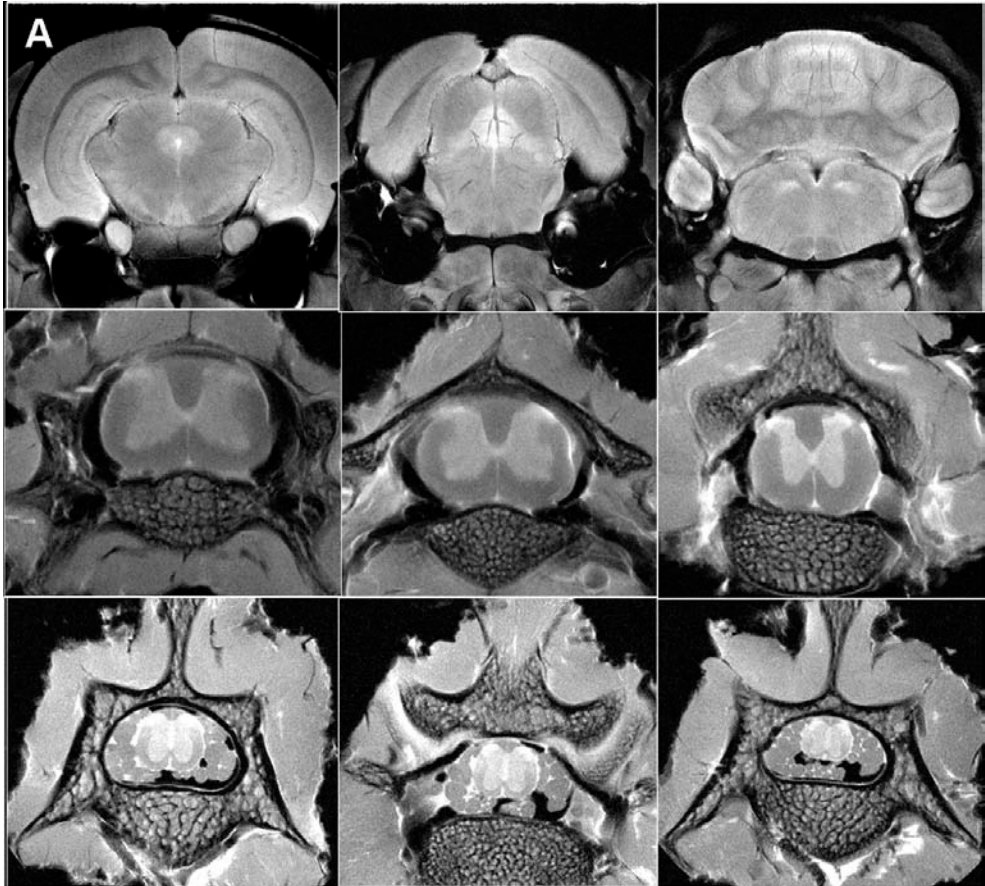
Figure 6.2: MR imaging of the infiltration of transferred SPIO labelled myelin reactive T cells into the CNS. Stimulated myelin reactive T cells were labeled with SPIO particles and transferred into naïve rats (B) or MBP primed rats at onset of the disease (C). When comparing the MR images to those of healthy not transferred rats (A), hypo-intense regions could be detected (arrows) indicating the presence of myelin reactive T cells.
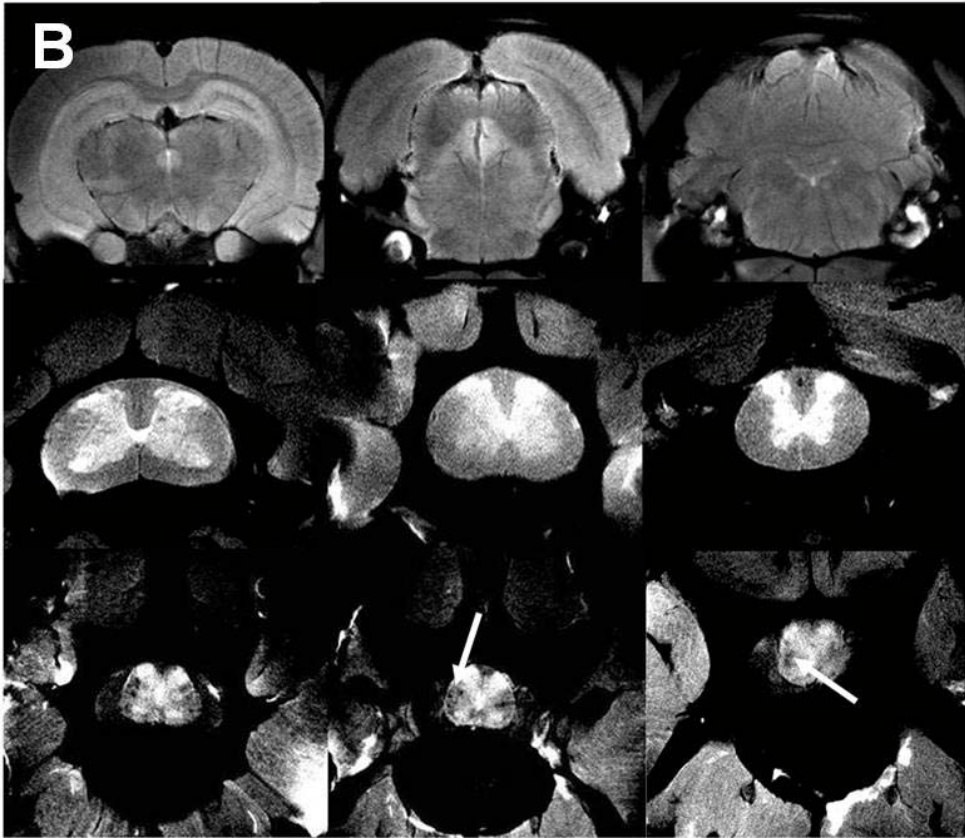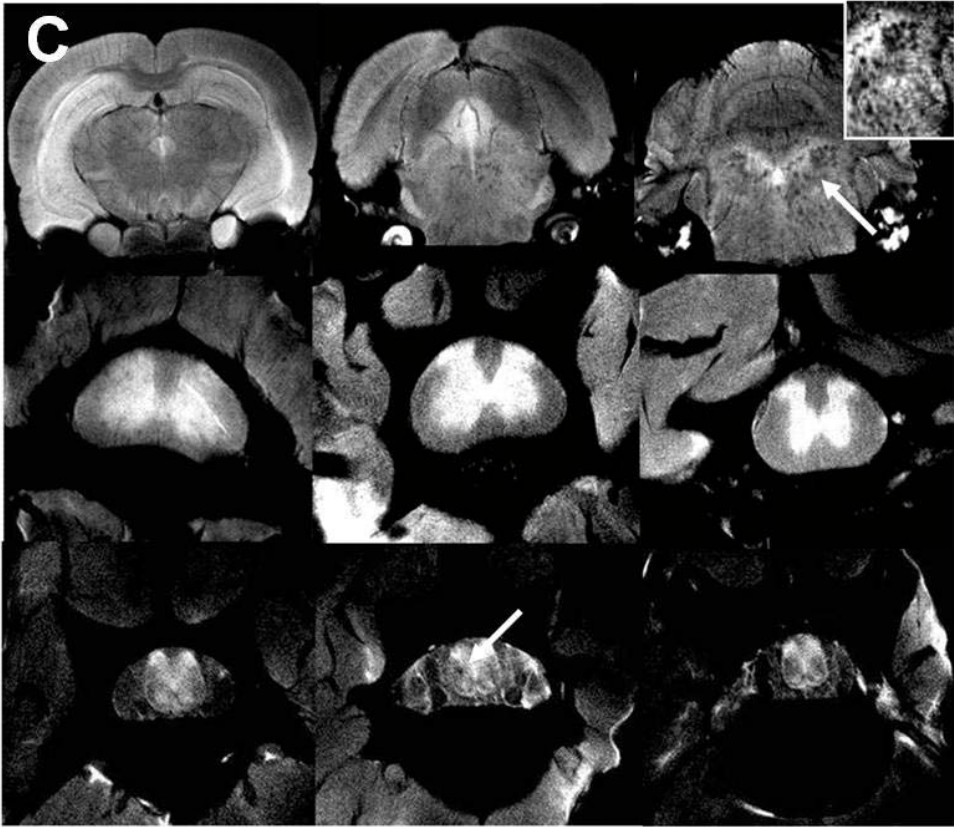
Prussian blue staining of the brain stem and cerebellum confirmed the presence of iron oxide labeled cells in this region **(Fig. 6.3 A and B)**. Immunohistochemical staining using an antibody directed against the CD3 surface marker of T cells further indicated the infiltration of T cells into these CNS regions **(Fig. 6.3 C)**. Immunofluorescent staining of the dextran coating of the contrast particles (red) showed the predominant localization of the particles within the T cells (green) **(Fig.6.3 D)**.

These results demonstrate the feasibility of visualizing the migration of systemically injected labeled myelin reactive T cells in the CNS of rats. As a conclusion, it proves that the distribution of myelin reactive T cells is different in naive and EAE primed animals.
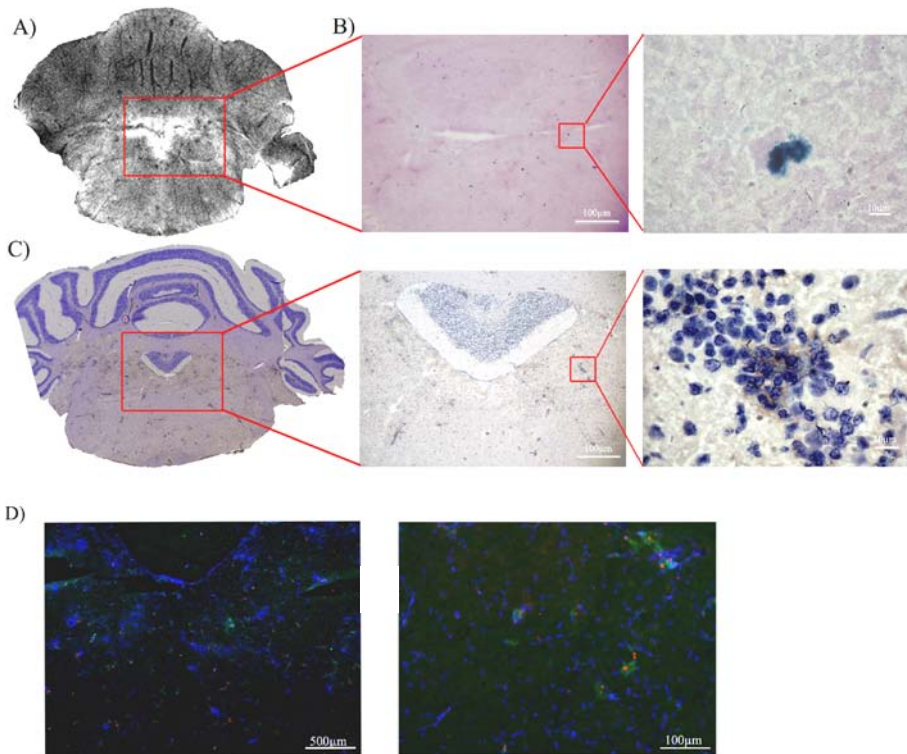
Figure 6.3: Histological confirmation of MRI findings: the hypo-intense regions detected in the brain stem after transfer of SPIO labeled T cells at the onset of disease (a) are shown to correspond to sites of iron particle accumulation as demonstrated by Prussian blue staining (b). Furthermore, using an anti-CD3 staining, the presence of T cells within this region was confirmed (c). Immunohistochemistry for dextran (red) and T cells (green) confirms the localization of the SPIO particles within the transferred T cells (d).

6.4 Conclusions

The high resolution MRI reference set of images obtained from the rats CNS, as shown and described in chapter 3, proves its value when evaluating the presence and spatial location of contrast labeled cells as demonstrated in this chapter. It offers not only the establishment of changes in signal intensity, but also provides accurate spatial information. The highly detailed images of the reference frame show many small anatomical structures of the CNS, whereas investigational images often suffer from low resolution, especially when acquired *in vivo*, and therefore depict limited details. Here, the high resolution reference images allow the determination of highly detailed structures that might be affected in the investigation setting.

Therefore the following main conclusions can be drawn with regard to this study: Post-mortem high resolution MRI of EAE animals, which are injected with USPIO at different time points during the disease course, demonstrates that monocytes are recruited to different inflamed regions of the CNS during the time course of the disease. Knowledge about the spatio-temporal distribution of these cells contributes to improved insights about the disease mechanism of EAE and eventually multiple sclerosis (Baeten et al., 2008).

This study further shows the potential of the MRI technique to visualize labeled myelin reactive T cells in the spinal cord and brain of recipient rats after administration. The presence of SPIO labeled T-cells was confirmed by histological double staining (dextran and CD3) afterwards. Different infiltration patterns of autoreactive T cells into the CNS were revealed in naive and EAE rats. Although labeling cells with SPIO is an interesting cellular imaging modality, caution must be taken with regard to selectivity and specificity. When SPIO-labeled T-cells die, the SPIO particles might be taken up by resident phagocytic cells, resulting in a non-specific macrophage labeling. This might cause misinterpretation of MRI hypo-intensities. All together, these results open new perspectives to investigate the role of different T cell subsets and to evaluate new MS therapies by means of MRI (Baeten et al., 2009).

References

Baeten K. 2009. Magnetic resonance based imaging of immune cells in experimental autoimmune encephalomyelitis. Diepenbeek: School for life sciences.

Baeten K, Hendriks JJ, Hellings N, Theunissen E, Vanderlocht J, Ryck LD, Gelan J, Stinissen P, Adriaensens P. 2008. Visualisation of the kinetics of macrophage infiltration during experimental autoimmune encephalomyelitis by magnetic resonance imaging. Journal of neuroimmunology 195(1-2):1-6.

Baeten K, Adriaensens P, Hendriks JJA, Theunissen E, Gelan J, Hellings N and Stinissen P. Tracking of myelin-reactive T cells in EAE animals using small particles of iron oxide and MRI. NMR in biomedicine. Published Online: April 2010. DOI: 10.1002/nbm.1501

Ben-Chetrit E, Brocke S. 2005. In: Lavi E, Constantinescu C, editors. Experimental models of multiple sclerosis. Induction of EAE: Springer US. p 11-24.

Bulte JW, Kraitchman DL. 2004. Iron oxide MR contrast agents for molecular and cellular imaging. NMR in biomedicine 17(7):484-499.

Crawford MP, Yan SX, Ortega SB, Mehta RS, Hewitt RE, Price DA, Stastny P, Douek DC, Koup RA, Racke MK, Karandikar NJ. 2004. High prevalence of autoreactive, neuroantigen-specific CD8+ T cells in multiple sclerosis revealed by novel flow cytometric assay. Blood 103(11):4222-4231.

Esiri MM, Reading MC. 1987. Macrophage populations associated with multiple sclerosis plaques. Neuropathology and applied neurobiology 13(6):451-465.

Fujinami RS, von Herrath MG, Christen U, Whitton JL. 2006. Molecular mimicry, bystander activation, or viral persistence: infections and autoimmune disease. Clinical microbiology reviews 19(1):80-94.

Hauser SL, Oksenberg JR. 2006. The neurobiology of multiple sclerosis: genes, inflammation, and neurodegeneration. Neuron 52(1):61-76.

Karpus WJ, Ransohoff RM. 1998. Chemokine regulation of experimental autoimmune encephalomyelitis: temporal and spatial expression patterns govern disease pathogenesis. Journal of immunology 161(6):2667-2671.

Kornek B, Lassmann H. 1999. Axonal pathology in multiple sclerosis. A historical note. Brain pathology (Zurich, Switzerland) 9(4):651-656.

Merrill JE. 1992. Proinflammatory and antiinflammatory cytokines in multiple sclerosis and central nervous system acquired immunodeficiency syndrome. Journal of immunotherapy (1991) 12(3):167-170.

Stark DD, Weissleder R, Elizondo G, Hahn PF, Saini S, Todd LE, Wittenberg J, Ferrucci JT. 1988. Superparamagnetic iron oxide: clinical application as a contrast agent for MR imaging of the liver. Radiology 168(2):297-301.

Chapter 7

Visualization of labeled
mesenchymal stem cells by MRI

Outline chapter 7

7.1 Introduction

7.2 Materials and methods

7.2.1 Characterisation of bone marrow derived mesenchymal stem cells

7.2.2 Determination of optimal labeling conditions for MSCs in culture

7.2.3 Visualization of labeled MSCs after administration

7.3 Results

7.3.1 Microscopic analysis of MSCs

7.3.2 Determination of the optimal labeling conditions for MSCs in culture

7.3.3 Visualizing the migration of labeled MSCs

7.3.4 Preliminary results of alternative experimental routes to administer MSCs in order to study their migration towards the CNS

7.4 Discussion

7.1 Introduction

Mesenchymal stromal cells (MSCs) possess clinical potential for treating diseases with cell-based therapies and are recently subjected to numerous early phase clinical trials (Giordano et al., 2007). Friedenstein and colleagues were the first who discovered a population of plastic adherent, fibroblast-like, colony-forming, multipotent stromal cells in the bone marrow (Friedenstein et al., 1968). MSCs can also be isolated from a number of other tissues as adipose tissue, liver, placenta, umbilical cord and teeth (Beyer Nardi and da Silva Meirelles, 2006; Troyer and Weiss, 2008; Yen and Sharpe, 2008). It is not clear at the moment whether tissue-specific resident MSCs create a reservoir of stem cells which contribute to maintenance and repair, or if the bone marrow forms a reservoir of stem cells which is mobilised when needed for tissue remodelling or regeneration (Kassem et al., 2004). MSCs have the capacity for extensive self-renewal and the potential to differentiate *in vitro* into various cell types such as adipocytes, chrondocytes and osteocytes on appropriate stimulation (Pittenger et al., 1999). Recent evidence exists that MSCs can also differentiate across germ layers towards neural or myocardial cell fates (Wakitani et al., 1995; Woodbury et al., 2002; Wislet-Gendebien et al., 2005) but this is still under debate. An important concern about the MSCs is the lack of a specific marker or combination of markers to define MSCs. *In vitro* expanded MSCs are known to express several non-specific markers, including CD29, CD44, CD73, CD90, CD105 and CD166, but are negative for hematopoietic (CD38, CD45) and endothelial markers (CD11, CD31) (Stewart et al., 2003; Beyer Nardi and da Silva Meirelles, 2006; Dominici et al., 2006).

Apart from their ability for multilineage differentiation, MSCs also have other interesting therapeutically relevant features: 1) capacity to migrate to sites of tissue damage and inflammation, 2) a hypo-immunogenic phenotype, 3) strong immunosuppressive properties and 4) the ability to produce growth factors and cytokines that might facilitate repair of injured tissues (Rasmusson, 2006; Chamberlain et al., 2007; Tyndall et al., 2007; Jones and McTaggart, 2008; Karussis et al., 2008). While there is emerging evidence in regard to target migration of MSCs, the fate of administrated MSCs requires elucidation. It has

been hypothesized that chemokines and chemokine receptors are involved in guiding migration of MSCs to specific targets (Honczarenko et al., 2006; Ozaki et al., 2007). The mechanisms by which MSCs home towards tissues and migrate across the endothelium is not yet fully understood. It is likely that injured tissues express specific receptors or ligands to facilitate trafficking, adhesion and infiltration of MSCs to the site of injury, as is known for the recruitment of leukocytes to sites of inflammation. The use of appropriate cell tags can provide information about the distribution of MSCs in the host upon administration. As mentioned above, MSCs have the advantage that they are immunologically privileged. They do not express MHC II antigens and have low expression of class I antigens. In addition, MSCs lack the expression of T-cell costimulatory molecules CD80 and CD86. This suggests that MSCs can avoid T-cell responses (Chamberlain et al., 2007) which makes them attractive for transplantation therapies. Additionally, *in vitro* studies show that MSCs can suppress ongoing immune reactions by the secretion of soluble factors or by cell-to-cell contact (Glennie et al., 2005; Fibbe et al., 2007). The immunomodulatory effects of MSCs have already been demonstrated in many animal models of injury including myocardial injury, renal ischemia and reperfusion injury, hepatic failure, burn wounds and autoimmune encephalomyelitis (Rasulov et al., 2006; Gerdoni et al., 2007; Ohnishi et al., 2007; Parekkadan et al., 2007; Semedo et al., 2007). Modulating the immune response together with the production of beneficial growth factors and cytokines could facilitate tissue repair or prevent worsening of the damage.

With regard to these characteristics of MSCs and previous chapters in this work, MRI in combination with the use of contrast particles is suggested as a powerful technique to study the migration of administrated MSCs towards inflammatory lesion sites and tissue injury in the CNS (Baeten et al., 2008). The experimental autoimmune encephalomyelitis (EAE) animal model, as described in chapter 6, displays both tissue damage and inflammation in the CNS and therefore provides a good model to investigate the migration and homing capacity of MSCs by MRI. Recent studies demonstrated that MSC transplantation improves clinical outcome in experimental EAE, an animal model for multiple sclerosis

(MS) (Zappia et al., 2005; Bai et al., 2009; Rafei et al., 2009b). MS is an auto immune mediated inflammatory disease of the central nervous system (CNS) leading to myelin breakdown. One of the great challenges in MS research is to develop strategies that will promote remyelination and neuroregeneration in the CNS. While endogenous adult neuronal cells of the CNS have limited capabilities for promoting full and long-lasting intrinsic self-repair, MSCs have been demonstrated to have immunomodulatory and neuroprotective potential in EAE (Kassis et al., 2008). Therefore, MSCs application holds promise for therapy of MS. While a peripheral immunosuppressive effect has been demonstrated, it is unclear whether MSCs also exert local protective effects in EAE by migrating to the multi-focal inflammatory lesion sites in the CNS (Zappia et al., 2005).

Goals of the study

The migration of administered murine MSCs in chronic EAE mice will be investigated by means of MRI and contrast particles. Due to the multi-focal character of the disease, a systemic iv injection is used to transplant MSCs to achieve an optimal migration of the MSCs towards the lesion sites in the CNS. Moreover, this administration route is self-evidently attractive when bearing the clinical applicability for MS in mind (Scolding et al., 2008). Prior to MSC transplantation, the cells are characterized and optimal conditions to label the MSCs with contrast particles are investigated.

7.2. Materials and methods

7.2.1 Characterisation of bone marrow derived mesenchymal stem cells

The MSCs-line, used in following experiments, was a kind gift of the Laboratory of Experimental Haematology at the University of Antwerp. The isolation procedure, immunophenotyping and cell modifications are described in (Bergwerf et al., 2009). Here, we only provide a brief summary.

MSCs were isolated from male ROSA26-L-S-L-Luciferase transgenic mice following a protocol previously described by Peister et all (2004), with minor modifications. The cells were expanded in 'complete expansion medium' (CEM), consisting of Iscove modified Dulbecco's medium (IMDM, Invitrogen) supplemented with 8% fetal calf serum (FCS, Invitrogen), 8% horse serum (HS, Invitrogen), 100 U/ml penicillin (Invitrogen), 100 mg/ml streptomycin (Invitrogen) and 1.25 mg/ml amphotericin B (Invitrogen). The cultured MSCs population has uniform expression of Sca-1, V-CAM and MHC I, without detectable expression of haematopoietic (CD45, c-kit, MHC II), endothelial (CD31) and neural (A2B5) surface markers. One parental MSC line was then chosen *ad random* and used for further experiments described in this chapter.

MSCs were transduced with a lentivirus encoding the enhanced green fluorescence protein (eGFP) and the puromycin resistance gene (Pac) to facilitate the tracking after transplantation. Flowcytometric analysis of BMSC-Luc/eGFP/Pac demonstated eGFP transgene expression in 95% of the cells, which remained stable in culture for at least 15 passages. In addition, phenotypical properties and luciferase activity were not influenced following lentiviral-transduction of MSC-Luc.

Microscopic analysis

Micrographs were obtained from the clonal MSCs to study their morphology and their ability to form colonies. Phase-contrast images were taken from MSCs in culture. For light microscopic and transmission electron microscopic (TEM)

images, MSCs were seeded on plastic coverslips (Thermanox®) (25000 cells/well) in 24-well plates. After 24 hours, MSCs were washed with PBS to discard the culture medium and subsequently fixed with UNIFIX® for 15 minutes at 4°C for light microscopic analysis. After fixation, cells were washed again with PBS and stained with hematoxilin. For electron microscopy, washed cells were fixed with 2% glutaraldehyde in a 0.05M cacodylate buffer (pH 7.3) at 4°C, post-fixed in 2% osmium tetroxide for 1 hour, stained with 2% uranyl acetate in 10% acetone for 20 minutes, dehydrated in graded concentrations of acetone, and embedded in expoxy resin (Araldite). Ultra-thin sections (0.06 μm) were mounted on grids, contrasted with uranyl acetate followed by lead citrate, and examined with a Philips EM 208 transmission electron microscope (TEM) operating at 80 kV.

7.2.2 Determination of optimal labeling conditions for MSCs in culture

Cell labeling with SPIO

Poly-L-lysine (PLL) was used as a transfection agent to facilitate the uptake of the iron particles by adherent MSCs. The superparamagnetic iron particles were provided as a solution with an iron concentration of 11.2 mg/ml (Endorem; Guerbet, France). SPIO-PLL complexes were made by mixing different amounts of SPIO particles and PLL (MW > 300 000; Sigma-Aldrich, Belgium) in serum-free CEM medium on a rotating shaker for 60 minutes at room temperature. An equal volume of SPIO-PLL complexes was added to the MSCs culture. The final concentrations of iron and PLL varied between 15 to 50 μg/ml and 0 to 1.5 μg/ml respectively. Cells were incubated at 37°C for 24 hours with the SPIO-PLL complexes and washed 3 times with PBS before further analysis.

Microscopic analysis of labeled MSCs

MSCs were seeded on plastic coverslips (Thermanox®) at a concentration of 30 000 cells/well in 24-well plates and grown for 24 hours before the SPIO-PLL complexes were added. After the labeling, the cells were washed with PBS to remove excess of contrast agent. For Prussian blue staining, which indicates the

presence of iron oxide, the cells were fixed with Unifix® for 15 minutes at 4°C, washed with PBS and incubated for 2 hours with a mixture of 2% potassium ferrocyanide and 2% hydrochloric acid. Afterwards the cells were counterstained with hematoxylin. To detect the distribution of SPIO /PLL complexes in the cells with TEM, labeled cells were pelleted and fixed with 2% glutaraldehyde in a 0.05M cacodylate buffer (pH 7.3) and routinely processed for electron microscopy, as previously described.

Determining iron content

The iron concentration of the MSCs after 24 hours of labeling with variable amounts of SPIO and PLL, was quantified by inductively coupled plasma (ICP) spectrometry using a Perkin Elmer Optima. After labeling, MSCs were washed three times, trypsinized and collected. Pellets of 1.10^6 cells were dissolved in 100 µl of an aqueous solution containing 65% HNO_3 and 10% H_2O_2. After 1 hour the suspension was diluted to 1 ml with H_2O. For Fe-measurements, the spectrometer was set to 239.56 nm and calibrated with 9 standards dissolved in HNO_3.

Viability and proliferation of labeled MSCs

The viability of labeled cells was analysed by incubating the cells for 20 minutes with 7-aminoactinomyocin (7-AAD) (BD Biosciences, Belgium) at 4°C. Then the cells were washed and the 7-AAD emission was immediately measured on a FACS Calibur system and analysed using CellQuest Software (BD Biosciences, Belgium).

7.2.3 Visualization of labeled MSCs after administration

Induction of chronic EAE

C57BL/6J mice were purchased from Harlan. 200 µg of MOG 35-55 (MEVGWYRSPFSRVVHLYRNGK) (Ansynth, The Netherlands) was dissolved in 100 µl PBS, to which 100 µl Complete Freund's Adjuvant (Sigma-Aldrich, Belgium) containing 5 mg/ml mycobacterium (Sigma-Aldrich, Belgium) was added. This

mixture was injected subcutaneously into the flanks. Directly after immunization and 48h later, mice received and intraperitoneal injection of 200 ng pertussis toxin. Mice were weighted and monitored daily for clinical signs of EAE. Disease severity was graded using a standard 5-point scale: 0, no symptoms; 1, decreased tail tone; 2, hindlimb paresis; 3 hindlimb paralysis 4, quadraparesis; 5, death. Mice that reached grade 4.5 were killed in accordance with the requirements of the ethics committee. All experiments were approved by the Hasselt University Ethics Committee for animal experiments.

Administration of labeled stem cells

During the injection procedures, mice were anaesthetized with an isoflurane gas mixture and placed on a heating pad.

Intravenous administration route

Labeled MSCs were injected in the tail vein of the immunised mice at the occurrence of the decreased tail tone (score 1). Hereto, labeled MSCs were dissolved in PBS at a concentration of $10*10^6$ cells/ml followed by an intravenous injection of $1*10^6$ cells/animal.

Intracisternal administration route

After sedating the mice, the back of the head was shaved and a 30-gauge needle (BD 30 Gx1/2″ REF 304000) (bent at a 40° angle 3 mm from the tip) attached to a 25 µl Hamilton syringe was inserted percutanously into the cleft between the occiput and the atlas vertebra providing access to the subarachnoid space of the cisterna magna (cerebellomedullary cistern) as described previously (Furlan et al., 2003; Tatlisumak and Fisher, 2006). Cell viability was tested by trypan blue dye exclusion before injection and only samples with over 90% viable cells were injected. Labeled MSCs suspended in sterile PBS were injected over 30 seconds in healthy mice (n=5) ($5*10^3$ MSCs in 10 µl PBS per animal).

Magnetic resonance imaging

Animals were transcardially perfused with PBS and 4% paraformaldehyde (PFA) 24 hours after MSCs administration. Post-mortem MR images were obtained in a 40 mm birdcage coil on a 400 MHz vertical bore spectrometer (Varian, VNMRS system, Palo Alto, California, USA) operating at 9.4 Tesla. Gradient echo (GEMS) imaging of the brain was performed with a TR=250 ms, TE=6 ms and NA=20. Axial images with an in-plane resolution of 100 x 100 µm were acquired using a data matrix of 256x256.

Fluorescence microscopy

Formalin fixed brain tissue was isolated and put on the vibratome (Microm international, Walldorf, Germany) to prepare coronal brain slices of 50 µm thickness for fluorescence microscopic analysis. Brain slices were loaded with a fluorescent probe, propidium iodide (PI) (5 µg/ml final concentration) to visualize the nuclei of cells, for 5 minutes at room temperature. Then, the slices were washed in PBS for 5 minutes to remove excess of PI. For fluorescence microscopic analysis (Eclipse 80i microscope and NIS-elements Basic Research version 2.3 microscopy software, Nikon), brain slices were transferred onto a glass slide and the presence of labeled eGFP positive MSCs was investigated with filters for eGFP (FITC) and PI (TRITC).

7.3 Results

The clonal MSC line, used in this chapter, was modified by the lab of origin in order to perform cell tracking experiments. The MSCs are eGFP-positive and also exhibit the possibility to trace them with bioluminescence imaging. After these cell modifications, the *in vitro* characteristics, i.e. morphology and immune phenotype, were investigated and no differences were observed with the parental MSCs derived from ROSA26-L-S-L-luciferase transgenic mice (Bergwerf et al., 2009). Additionally, (ultra)microscopic analysis was performed in our lab. In order to perform cell tracking by MRI, the labeling of MSCs with MR visible contrast particles (SPIO) was optimized in our lab.

7.3.1 Microscopic analysis of MSCs

After hematoxylin staining of a non-confluent monolayer, the clonal MSCs show diverse morphologies, including small spindle shaped and flattened polygonal phenotypes **(Fig. 7.1 A-B)**. Sporadically, colony formation is observed in the cultures **(Fig. 7.1 C)**. It is visualized on a phase-contrast micrograph as a multi-layered structure with outgrowth of cells at the base. After multiple passages, the spindle-like MSCs gradually were transformed into broad flattened polygonal cells. This transformation appeared to be accompanied by a progressive decrease in the tendency of the cells to form colonies.

Transmission electron microscopic (TEM) images **(Fig. 7.2)** show that MSCs contain an ovoid/elliptical euchromatic nucleus with several nucleoli. The chromatin is dispersed except for a thin dense layer located immediately inside the perinuclear membrane. The inner part of the cytoplasm was rich in round and elongated mitochondria. The rough endoplasmatic reticulum was often distended and contained moderately electron-dense secretory material. Cytoplasmic filaments were observed, but were rare and their alignment was irregular. The perinuclear zone is an organel rich area, while the peripheral cytoplasm and cell processes are lacking organelles.
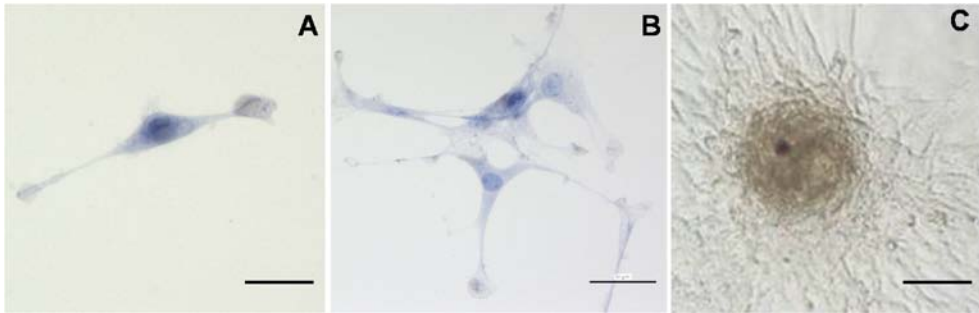
Figure 7.1: MSCs in culture are heterogeneous in morphology and form colonies. Light microscopic images show that MSC cultures contain spindle-shaped (A) and flat polygonal (B) cells. Colony formation is observed on the phase-contrast micrograph (C). Colonies have a rosette-like structure with densely overcrowded cell layers. Scale bars: 100 μm (A), 50 μm (B) and 200 μm (C).
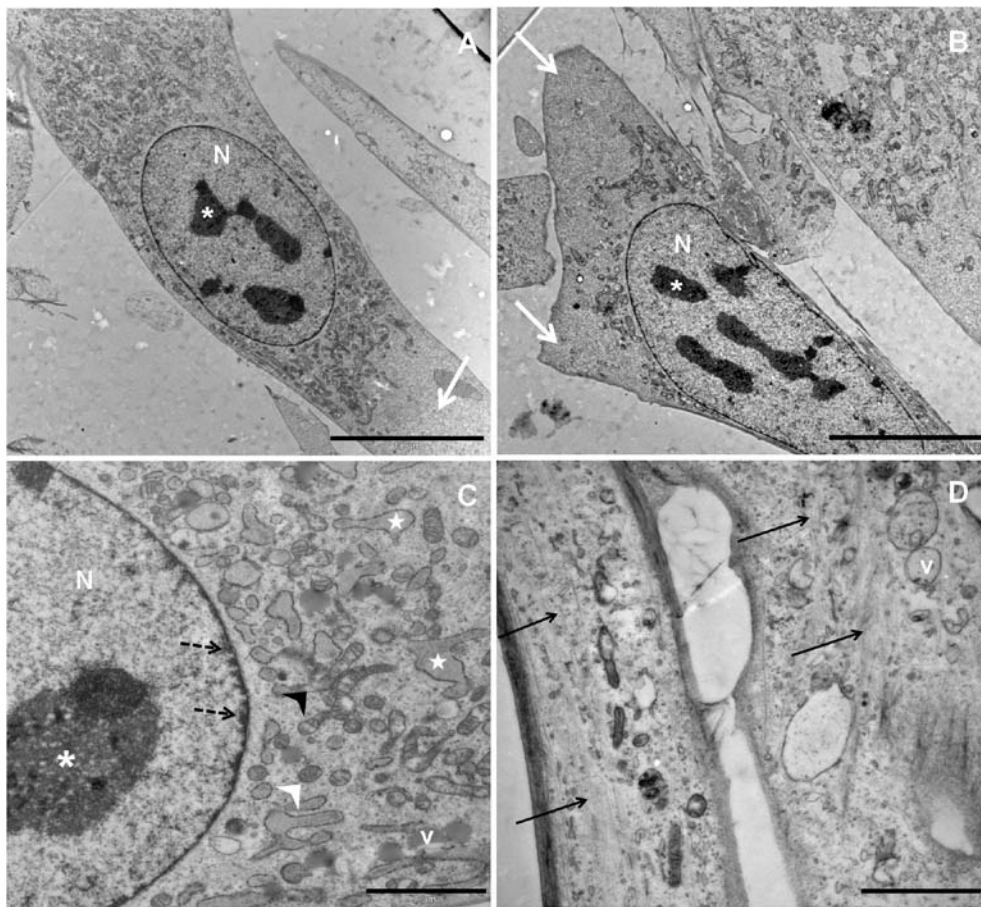
Figure 7.2: Ultrastructural characteristics of MSCs. All cells show an elliptical nucleus (N) with multiple nucleoli (asterisks). Chromatin is spread throughout the nucleus (euchromatin) except for a thin dense layer (heterochromatin) in close relationship to the inside of the perinuclear membrane (dashed arrows). The inner part of the cytoplasm is rich in organelles whereas the peripheral zone was lacking organelles (white arrows). The perinuclear zone contained rough endoplasmatic reticulum cisternae, which are often dilated (pentagram), round or elongated mitochondria (white or black arrowheads respectively) and many vesicles (v). Filaments are seen throughout the cytoplasm (black arrows). Scale bars: 10 µm (A-B), 2 µm (C-D).

7.3.2 Determination of the optimal labeling conditions for MSCs in culture

Microscopic evaluation

Prussian blue stains of MSCs incubated for 24 hours with different ratios of SPIO and PLL are presented in **figure 7.3**. When the MSCs are incubated with varying concentration of SPIO alone, intracellular labeling is not detectable with Prussian blue staining **(Fig. 7.3 first row)**. Numerous iron-containing intracytoplasmatic deposits are observed with Prussian blue staining when PLL, the transfection agent, is added. Under the conditions of 25 and 50 µg SPIO/ml combined with 0.75 µg PLL/ml, almost all cells haven taken up contrast particles. In contrast, under the condition of 15 µg SPIO and 0.75 µg PLL/ml only a small portion of the population contains contrast particles. However, as the concentration of SPIO increases (≥ 50 µg SPIO/ml), more extracellular aggregates are observed in the culture. This might introduce misinterpretation as they circulate free in the bloodstream after injection and are taken up by macrophages. Therefore, it can be concluded that the combination of 25 µg SPIO and 0.75 µg PLL/ml is the most optimal mixture to label the MSCs.

Figure 7.3: Prussian blue staining of MSCs labeled with different ratios of SPIO/PLL. Contrast particles are seen as bright blue dots (in images of row 2 – 0.75 µg PLL/ml. Efficient intracellular up-take is only seen when PLL, is added. Almost the complete MSC population is labeled when SPIO concentrations of 25 µg/ml or higher are used. Scale bars: 50 µm.
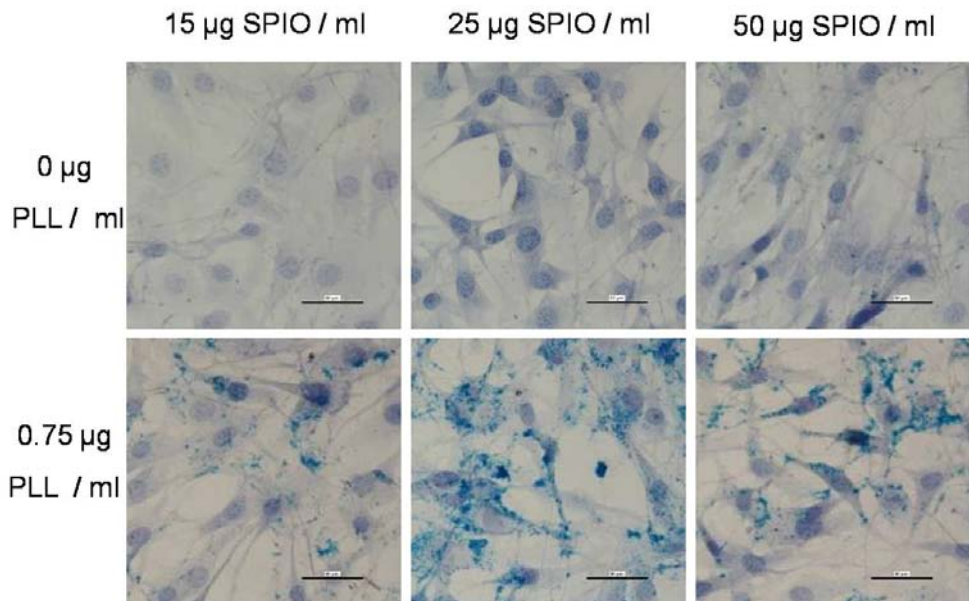
The presence of contrast particles inside the MSCs was confirmed by TEM images **(Fig. 7.4)** for MSCs that were incubated for 24 hours with mixture containing 25 μg SPIO/ml and 0.75 μg PLL/ml. Electron dense clusters of SPIO, surrounded by a membrane, are detected within the cell cytoplasm of MSCs and indicate that the SPIO/PLL complexes are taken up by an endocytotic process.
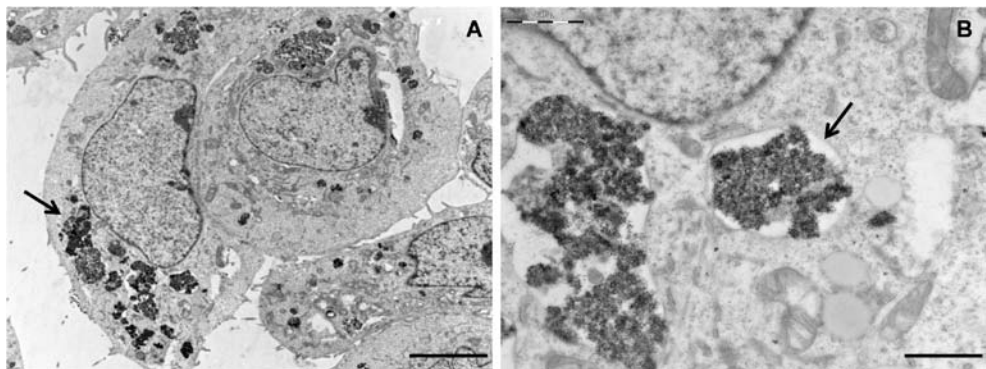
Figure 7.4: Transmission electron micrographs of SPIO-labeled MSCs with following mixture 25 μg SPIO/ml and 0.75 μg PLL/ml. SPIO clusters are seen as electron dense features on TEM images. The cytoplasm shows endosomal vesicles containing SPIO/PLL complexes (black arrow). Figure B clearly depicts the presence of a membrane surrounding the SPIO particles. Scale bar: 5 μm (A) and 1 μm (B).

Quantification of the cellular iron content

The mean iron content (in pictogram) per cell is quantified by ICP spectroscopy after 24 hours of labeling. **Figure 7.5** shows the resulting iron concentration for different ratios of SPIO/PLL. An increasing amount of iron is measured when increasing amounts of SPIO and a constant PLL concentration is used. When no transfection agent is added, a very low amount of iron (< 2 pg/ cell) is detected. The graph demonstrates that using a concentration 0.75 µg PLL/ml results in the highest uptake of SPIO per cell for each investigated SPIO concentration. The mean iron content per cell with a fixed concentration of 0.75 µg PLL/ml is 5.4, 8.9 and 14.3 pg when using 15, 25 or 50 µg SPIO/ml, respectively. However, more extracellular SPIO aggregates are detectable upon using higher SPIO concentrations as demonstrate by microscopic analysis.
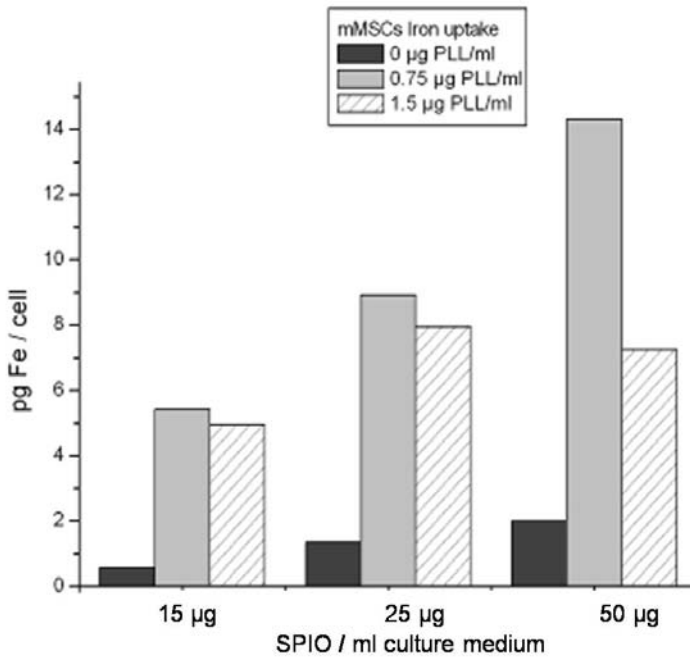
Figure 7.5: Quantification of the mean amount iron present per cell after an incubation period of 24 hours with different SPIO/PLL ratios. Using 0.75 µg PLL/ml results in the highest uptake of contrast particles for each investigated SPIO concentration. When incubating the MSCs with SPIO alone, only a very limited amount of contrast particles is internalized.

Cell viability after labeling

Immediately after SPIO labeling, the 7-AAD assay demonstrated no significant decrease in cell viability of MSCs labeled with various concentrations of SPIO and a fixed PLL concentration of 0.75 µg PLL/ml as compared to unlabeled MSCs **(Fig. 7.6)**.
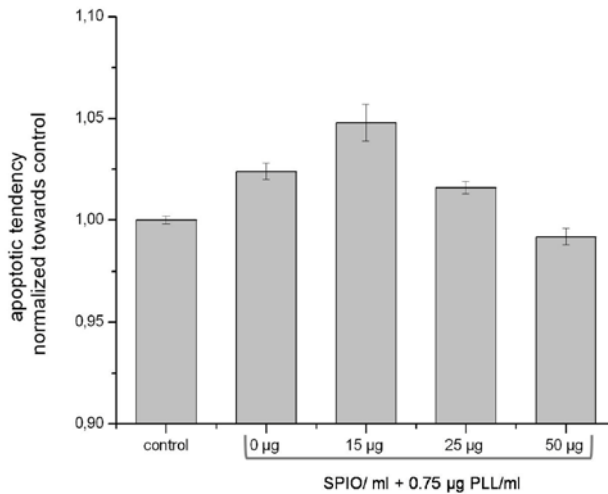
Figure 7.6: SPIO-labeling does not alter cell viability. When incubating MSCs with various concentrations of SPIO and 0.75 µg PLL/ml for 24 hours, the amount of cell death is not significantly increased for labeled cells as compared to unlabeled control MSCs. The amount of cell death is shown as a normalized value (unlabeled control MSCs = 1.00).

Based on microscopic inspection, determination of iron content and viability tests, it can be concluded that efficient labeling of MSCs can be achieved when using a combination of 25 µg SPIO and 0.75 µg PLL/ml culture medium. This mixture will be used for all the upcoming experiments in this chapter.

7.3.3 Visualizing the migration of labeled MSCs

Chronic EAE was induced in C57BL/6J mice (n = 14) by active immunization with MOG resulting in a disease characterised by significant weight loss at day 11-12 post immunization (p.i.) followed by total tail paralysis (score 1-1,5) and hind limb paralysis (score 2). When tail paralysis occurred, EAE mice were injected with $1*10^6$ labeled MSCs in a volume of 100 µl. Almost immediately after the MSCs were intravenously (IV) infused into the mice, respiratory failure, followed by death, was observed.

Embolic entrapment of the cells in the lungs probably leads to this adverse event **(Fig. 7.7)**. Although this administration route was successfully applied in several published studies (Zappia et al., 2005; Francois et al., 2006; Kassis et al., 2008), we were not able to avoid this adverse event despite numerous adaptations and precautions as listed below **(Table 7.1)** (Schrepfer et al., 2007; Fischer et al., 2009).
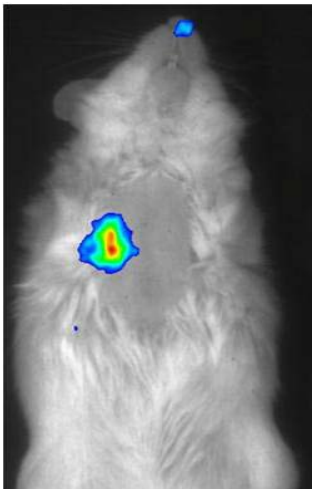
Figure 7.7: Visualization of MSCs trapped in the lungs with bioluminescence after iv injection. Infusion of SPIO labeled MSCs caused lethal pulmonary embolism in the EAE mice. Analogous experiments were carried out in the laboratory of origin (Prof. Dr. Ponsaerts, University of Antwerp), also with lethal outcome. Immediately after infusion, animals were studied by bioluminescence to confirm the presence of MSCs in the lungs. The bioluminescence image, here shown, is kindly provided by dra. Nathalie De Vocht and Prof. Dr. Peter Ponsaerts, Laboratory of Experimental Hematology, University of Antwerp, Belgium.

Table 7.1: Adaptations for intravenous administration of MSCs

1	Decreased cell concentration	Increase volume up to 200 µl
		Decrease amount of cells to $5*10^5$
2	Elongate administration time frame	Inject as slowly as possible
		Inject with time intervals
3	Induce massive dilatation of blood vessels	Warming-up animals with heating lamp besides standard used heating pad
4	Minimize clothing of the cells	Dilute in PBS without Ca and Mg
		Sqeezing cells through a mesh
5	Combinations of all protocols mentioned above	

7.3.4 Preliminary results of alternative experimental routes to administer MSCs in order to study their migration towards the CNS

As it was not possible to deliver the MSCs intravenously, alternative administration routes to inject the cells were found in literature: intra-arterial, intraventricular, intracisternal (IC) or local (intra- or perilesional) delivery (Pluchino et al., 2003; Ben-Hur and Goldman, 2008). In this chapter, the feasibility of administering labeled MSCs by intracisteral injection was further investigated.

Intracisternal injection of labeled MSCs

The cisterna magna is part of the subarachnoid space, which is filled with cerebrospinal fluid and lies in close relation to the brain stem area. In EAE mice, the brain stem is most often affected by infiltrating immune cells causing inflammation and tissue damage. Therefore it was hypothesized that the delivery of MSCs into the cisterna magna may offer a good alternative for

studying the migration of labeled MSCs towards the inflamed lesion in the brain stem by MRI. In the present experiment, healthy mice (n=5) received an injection with labeled MSCs ($5*10^3$ in 10 µl PBS) in the cisterna magna.

In this experiment, all the animals survived the IC injection for at least 24 hours. MR imaging showed either no hypo-intensities within the CNS tissue for 3 animals or depicted a hypo-intense area (**Fig. 7.8 A** white arrows) at the dorsal side of the brain stem in 2 animals. Prussian blue staining confirmed the presence of contrast particles (**Fig. 7.8 B** black arrows) in these hypo-intense areas. However, since the contrast particles are localized in areas where also bleeding had occurred (dashed arrows; bleeding also appears black on MRI images), it is not possible to discriminate between SPIO particles and hemorrhage with MRI. This tissue damage is probably related to a suboptimal injection procedure whereby the needle tip injures the brain tissue. On the fluorescence images **(Fig. 7.8 C-E)**, acquired at the ventral side of the brain stem, intense green signals were detected **(Fig. 7.8 D)**, which might indicate the presence of the eGFP positive MSCs. Prussian blue staining showed a few intense blue deposits at the ventral side of the brainstem **(Fig. 7.8 F-H)** confirming the presence of SPIO labeled MSCs. MR images cannot confirm this since the labeled cells are situated too close to the basal skull bones, which are also hypo-intense on MRI images. Moreover, the amount of labeled cells, as demonstrated by histology and fluorescence, is rather low.

This preliminary experiment shows the potential use of IC injections since it concerns an almost non-invasive technique which is advantageous for the survival of the animals. However, deeper investigation is required since the animals used for these initial experiments were healthy animals (not EAE animals). When inflammation is present in EAE animals, it might be hypothesized that IC injected MSCs are able to infiltrate the brain stem tissue and might be detectable on MR images. Also longer infiltration periods (longer than 24 hours) can be considered in this respect.
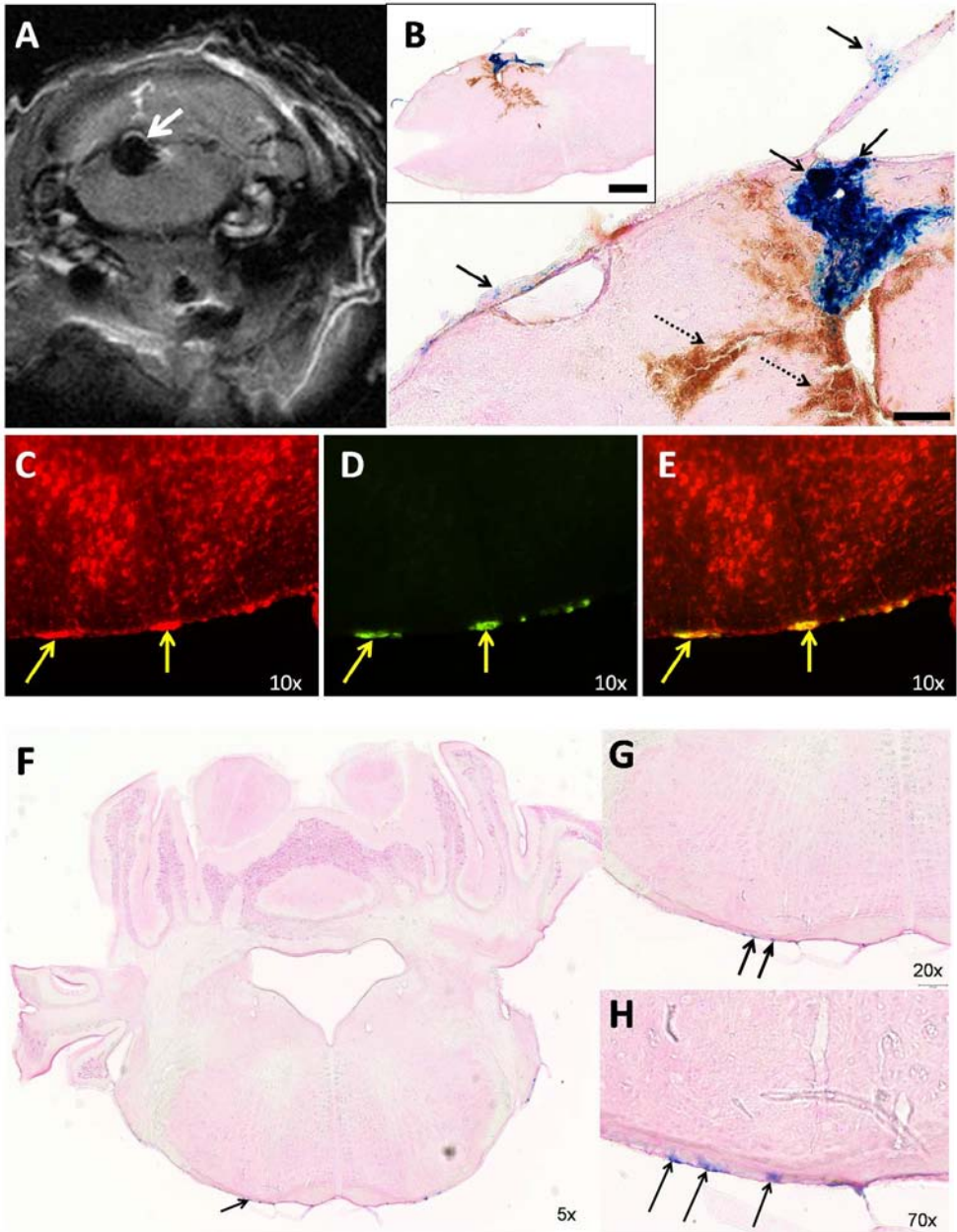
Figure 7.8: SPIO labeled MSCs are not detectable on MR images after intracisternal delivery. Hypo-intensities visible on MR-images (A, white arrow) correspond to areas containing both SPIO labeled cells (B, black arrows) and bleeding rests (B, dashed arrows). Fluorescence microscopic analysis shows the presence of eGFP positive cells (D, yellow arrow) at the ventral side of the brainstem (C depicts nucleus staining with PI and E shows overlay between C and D). Light blue SPIO deposits are detected on Prussian blue stained sections (B, F-H). The Prussian blue positive deposits (F and H, black arrows) at the ventral side of the brainstem correspond well with the eGFP positive cells on the fluorescence images. Scale bar: image B 100 µm and inset 500 µm.

7.4 Discussion

MSCs were first described in 1968 by Friedenstein et al, who discovered that MSCs adhered to tissue culture plates, resembled fibroblasts in morphology, and grew in form of a colony (Friedenstein et al., 1968). MSCs are a type of multipotent progenitor cells located in the stromal component of bone marrow. In addition to their promising potential for tissue repair and regeneration they also exert immunomodulatory properties. The use of these MSCs for cell-based therapies relies on the capacity of these cells to home and engraft long term into the appropriate target tissue. Although the mechanisms by which MSCs are recruited to tissues are not yet fully understood, it is possible that chemokines and their receptors are involved, as they are important factors known to control cell migration (Sordi, 2009). Thus, modulating MSC homing might be a potential strategy for tissue repair and development of new therapeutic applications. A better understanding of the MSC homing mechanisms may lead to the development of therapeutic strategies with the potential to improve clinical applications of MSCs.

With regard to these expectations, the delivery of sufficient MSCs into regions of interest is a prerequisite for achieving therapeutic benefits of cell therapy. Therefore a reliable technique for tracking grafted cells is desired. Potentially, MRI may be a suitable tool for visualizing migration and homing of administred MSCs in vivo. However, the cells need to be labeled prior to transplantation to be visible on MRI. Both gadolinium- and iron-based (SPIO) contrast agents can be used to label the selected cells (Bulte and Kraitchman, 2004). Gadolinium chelates cause a low relaxivity when taken up by targeted cells. Furthermore, gadolinium is not biocompatible and very little is known about its potential toxicity following cellular dechelation over time. On the other hand, SPIO particles such as Endorem$^®$ are clinically approved, biodegradable and can be safely re-used by a biological organism (Weissleder et al., 1989). Due to their strong effect on local magnetic field homogeneity and spin-spin relaxation times (increasing T2 relaxation rate), iron-based contrast agents can be readily detected as signal voids on T2-weighted images. This study examined the

feasibility of labeling murine MSCs, the effect of SPIO on cell viability and the administration of labeled MSCs via intravenous injection. The results of this study demonstrate the ability to label murine MSCs efficiently by combining commercially available (FDA approved) ferumoxides with a transfection agent. Although most non-phagocytotic cells do not take up SPIO particles efficiently or require high amounts of contrast particles in culture, these results indicate that with a relatively low concentration of SPIO (i.e. 25 µg SPIO/ml) in culture media, cellular labeling with these contrast particles and PLL can be accomplished. After incubating MSCs for 24 hours with SPIO/PLL mixtures, we observed high amounts (qualitatively) of intracytoplasmatic Prussian blue-positive particles in the cells, although intracellular aggregates appear when using high concentrations $\geq$ (50 µg/ml) of SPIO.   Ultrastructural analysis provided evidence that contrast particles are incorporated by the cell via endocytosis and reside in the endosomal compartments. Validation of the intracytoplasmatic iron content demonstrated that a sufficient amount of iron (at least 3 pg/cell) has to be taken up to be detectable on MRI (Bulte et al., 2004). For the most optimal labeling condition (25 µg SPIO and 0.75 µg PLL/ml) described in this work, the averaged iron content was about 8.9 iron pg/cell. Furthermore, it was shown that this amount of SPIO particles did not affect viability of the cells. Thus by taking into I) account the labeling quality, II) the averaged iron content/cell and III) the viability, it was concluded to use the combination of 25 µg SPIO and 0.75 PLL/ml as an optimal protocol to label the MSCs with contrast particles.

Several studies have demonstrated that systemic delivery of MSCs results in improved clinical outcome in EAE animals, the animal model for MS (Zappia et al., 2005; Bai et al., 2009; Rafei et al., 2009a). The substantial recovery seen in the CNS of EAE animals, treated with MSCs, suggests that they may act locally to promote repair through several distinct mechanisms such as secretion of neuroprotective factors, suppression of inflammation or stimulation of endogenous remyelination. Notwithstanding this local effect, it is also suggested that the embolization of the MSCs in the lung activates MSCs to secrete anti-inflammatory factor TSG-6 (Tumor necrosis factor alpha-induced protein 6)

(Hwa Lee et all, 2009). The secretion of this factor may in part explain the therapeutic effect observed after iv infusion of MSCs in animal models for EAE, diabetes type I, myocardial infarction or arthritis.

To elucidate whether MSCs migrate and home to injured and inflamed tissue in the CNS of EAE mice, SPIO labeled MSCs were intravenously injected and tracked by MRI. Although such a systemic delivery technique of MSCs seems to be successfully used by other groups, we were not able to show the biodistribution of injected labeled MSCs because they were strongly trapped in the microcirculation of the lung leading to death of the animals (Fischer et al., 2009).

As an alternative experimental setting to deliver the MSCs in close proximity of the inflamed CNS, the feasibility of an IC injection with contrast labeled MSCs was investigated. This IC procedure does not require stereotactic precision as needed for intraventricular injections and moreover, the method is fast and almost non-invasive, which benefits a good survival of the animals. These preliminary results show that MSCs injected in the subarachnoidal space can migrate towards the brain stem. However, since only few contrast labeled cells are present, no matching hypo-intensities can be detected on MR-images because the MR technique is not sensitive enough to detect single cells. Moreover, the locations where hypo-intensities should be detected on the MR images (based on histology and fluorescence images) correspond to areas where haemorrhage occurred due to the injection or to sites in close proximity to the skull bones. Although, more sensitive techniques such as histology and fluorescence microscopy can be used to detect small amounts of cells, these methods hamper serial follow up in time which is on the other hand the main advantage of MRI. Therefore, it might be interesting to perform these IC injection experiments with EAE animals since inflammation might lead to enhanced MSCs migration towards the inflamed regions in the brain stem. Also longer infiltration periods (longer than 24 hours) can be considered in this respect. To improve the detection of injected cells by MRI in future experiments, MSCs can be tagged with double contrast labels, i.e. gadolinium (Gd) and SPIO

particles. T1 imaging shows the presence of Gd labeled cells as hyper-intense signal intensities. This might provide a method to discriminate between Gd labeled cells (hyper-intense) and haemorrhages (hypo-intense) on T1-weighted images. The SPIO particles, on the other hand, can be used to trace labeled cells once they have migrated away from the injection site via T2-weighted images. The presence of SPIO labeled cells can then also be confirmed by Prussian blue staining of histologic sections afterwards.

Although labeling cells with SPIO is an interesting cellular imaging modality, caution must be taken with regard to selectivity and sensitivity. Upon cell death of SPIO labeled cells, the SPIO nanoparticles may be taken up by resident phagocytic cells, resulting in a non-specific macrophage labeling. This might cause misinterpretation of MRI hypo-intensities. Another drawback is that the average concentration intracellular agent concentration is diluted by every cell division, which tend to diminish the image contrast of the cells over time. The SPIO particles might also be subjected to degradation in the lysosomal compartments of the cells leading to the disappearance of the hypo-intense MR signal.

As a second alternative setting to deliver the MSCs in the proximity of the inflamed CNS, the use of a spinal cord injury model is suggested. In such a model there is only injury at a single, well-defined location in the spinal cord. This single target location facilitates the evaluation of the migration capacity of perilesional injected (double) labeled MSCs by MRI. Future experiments can focus on modifying the expression of functional chemokine receptors on MSCs in order to enhance the migration potential of MSCs, as it is hypothesized that the homing of MSCs is regulated by reciprocal interaction of chemokine receptors and gradients of chemoattractants. Increasing the portion of MSCs that find their way to the targets in the CNS will not only influence the clinical outcome, but also offers new strategies where MSCs can be used as vehicles to deliver neurotrophic factors or other beneficial molecules that promote tissue repair.

In conclusion, SPIO labeling is not deleterious to murine MSCs and offers a powerful method to elucidate migration mechanisms of MSCs by means of MRI. However, caution must be given when considering an appropriate administration route for these cells. Intravenous injection of MSCs often results in embolic entrapment of these cells in the lungs consequently leading to respiratory failure and death of the animals. IC administration is an interesting alternative for the delivery of cells in close proximity to the CNS.

References

Baeten K, Hendriks JJ, Hellings N, Theunissen E, Vanderlocht J, Ryck LD, Gelan J, Stinissen P, Adriaensens P. 2008. Visualisation of the kinetics of macrophage infiltration during experimental autoimmune encephalomyelitis by magnetic resonance imaging. Journal of neuroimmunology 195(1-2):1-6.

Bai L, Lennon DP, Eaton V, Maier K, Caplan AI, Miller SD, Miller RH. 2009. Human bone marrow-derived mesenchymal stem cells induce Th2-polarized immune response and promote endogenous repair in animal models of multiple sclerosis. Glia 57(11):1192-1203.

Ben-Hur T, Goldman SA. 2008. Prospects of cell therapy for disorders of myelin. Annals of the New York Academy of Sciences 1142:218-249.

Bergwerf I, De Vocht N, Tambuyzer B, Verschueren J, Reekmans K, Daans J, Ibrahimi A, Van Tendeloo V, Chatterjee S, Goossens H, Jorens PG, Baekelandt V, Ysebaert D, Van Marck E, Berneman ZN, Linden AV, Ponsaerts P. 2009. Reporter gene-expressing bone marrow-derived stromal cells are immune-tolerated following implantation in the central nervous system of syngeneic immunocompetent mice. BMC biotechnology 9:1.

Beyer Nardi N, da Silva Meirelles L. 2006. Mesenchymal stem cells: isolation, in vitro expansion and characterization. Handbook of experimental pharmacology(174):249-282.

Bulte JW, Arbab AS, Douglas T, Frank JA. 2004. Preparation of magnetically labeled cells for cell tracking by magnetic resonance imaging. Methods in enzymology 386:275-299.

Bulte JW, Kraitchman DL. 2004. Iron oxide MR contrast agents for molecular and cellular imaging. NMR in biomedicine 17(7):484-499.

Chamberlain G, Fox J, Ashton B, Middleton J. 2007. Concise review: mesenchymal stem cells: their phenotype, differentiation capacity, immunological features, and potential for homing. Stem cells 25(11):2739-2749.

Dominici M, Le Blanc K, Mueller I, Slaper-Cortenbach I, Marini F, Krause D, Deans R, Keating A, Prockop D, Horwitz E. 2006. Minimal criteria for defining multipotent mesenchymal stromal cells. The International Society for Cellular Therapy position statement. Cytotherapy 8(4):315-317.

Fibbe WE, Nauta AJ, Roelofs H. 2007. Modulation of immune responses by mesenchymal stem cells. Annals of the New York Academy of Sciences 1106:272-278.

Fischer UM, Harting MT, Jimenez F, Monzon-Posadas WO, Xue H, Savitz SI, Laine GA, Cox CS, Jr. 2009. Pulmonary passage is a major obstacle for intravenous stem cell delivery: the pulmonary first-pass effect. Stem cells and development 18(5):683-692.

Francois S, Bensidhoum M, Mouiseddine M, Mazurier C, Allenet B, Semont A, Frick J, Sache A, Bouchet S, Thierry D, Gourmelon P, Gorin NC, Chapel A. 2006. Local irradiation not only induces homing of human mesenchymal stem cells at exposed sites but promotes their widespread engraftment to multiple organs: a study of their quantitative distribution after irradiation damage. Stem cells 24(4):1020-1029.

Friedenstein AJ, Petrakova KV, Kurolesova AI, Frolova GP. 1968. Heterotopic of bone marrow. Analysis of precursor cells for osteogenic and hematopoietic tissues. Transplantation 6(2):230-247.

Furlan R, Pluchino S, Marconi PC, Martino G. 2003. Cytokine gene delivery into the central nervous system using intrathecally injected nonreplicative viral vectors. Methods in molecular biology 215:279-289.

Gerdoni E, Gallo B, Casazza S, Musio S, Bonanni I, Pedemonte E, Mantegazza R, Frassoni F, Mancardi G, Pedotti R, Uccelli A. 2007. Mesenchymal stem cells effectively modulate pathogenic immune response in experimental autoimmune encephalomyelitis. Annals of neurology 61(3):219-227.

Giordano A, Galderisi U, Marino IR. 2007. From the laboratory bench to the patient's bedside: an update on clinical trials with mesenchymal stem cells. Journal of cellular physiology 211(1):27-35.

Glennie S, Soeiro I, Dyson PJ, Lam EW, Dazzi F. 2005. Bone marrow mesenchymal stem cells induce division arrest anergy of activated T cells. Blood 105(7):2821-2827.

Honczarenko M, Le Y, Swierkowski M, Ghiran I, Glodek AM, Silberstein LE. 2006. Human bone marrow stromal cells express a distinct set of biologically functional chemokine receptors. Stem cells 24(4):1030-1041.

Hwa Lee R, Pulin A, Jeong Seo M, Kota D,Ylostalo J, Larson B,Semprun-Prieto L, Delafontaine P, Porckop D. 2009. Inravenous hMSCs improve myocardial infaction in mice because cells embolized in lung are activated to secrete the anti-inflammatory protein TSG-6. Cell Press 5:54-63.

6Jones BJ, McTaggart SJ. 2008. Immunosuppression by mesenchymal stromal cells: from culture to clinic. Experimental hematology 36(6):733-741.

Karussis D, Kassis I, Kurkalli BG, Slavin S. 2008. Immunomodulation and neuroprotection with mesenchymal bone marrow stem cells (MSCs): a proposed treatment for multiple sclerosis and other neuroimmunological/neurodegenerative diseases. Journal of the neurological sciences 265(1-2):131-135.

Kassem M, Kristiansen M, Abdallah BM. 2004. Mesenchymal stem cells: cell biology and potential use in therapy. Basic & clinical pharmacology & toxicology 95(5):209-214.

Kassis I, Grigoriadis N, Gowda-Kurkalli B, Mizrachi-Kol R, Ben-Hur T, Slavin S, Abramsky O, Karussis D. 2008. Neuroprotection and immunomodulation with mesenchymal stem cells in chronic experimental autoimmune encephalomyelitis. Archives of neurology 65(6):753-761.

Ohnishi S, Yanagawa B, Tanaka K, Miyahara Y, Obata H, Kataoka M, Kodama M, Ishibashi-Ueda H, Kangawa K, Kitamura S, Nagaya N. 2007. Transplantation of mesenchymal stem cells attenuates myocardial injury and dysfunction in a rat model of acute myocarditis. Journal of molecular and cellular cardiology 42(1):88-97.

Ozaki Y, Nishimura M, Sekiya K, Suehiro F, Kanawa M, Nikawa H, Hamada T, Kato Y. 2007. Comprehensive analysis of chemotactic factors for bone marrow mesenchymal stem cells. Stem cells and development 16(1):119-129.

Parekkadan B, van Poll D, Suganuma K, Carter EA, Berthiaume F, Tilles AW, Yarmush ML. 2007. Mesenchymal stem cell-derived molecules reverse fulminant hepatic failure. PloS one 2(9):e941.

Pittenger MF, Mackay AM, Beck SC, Jaiswal RK, Douglas R, Mosca JD, Moorman MA, Simonetti DW, Craig S, Marshak DR. 1999. Multilineage potential of adult human mesenchymal stem cells. Science 284(5411):143-147.

Pluchino S, Quattrini A, Brambilla E, Gritti A, Salani G, Dina G, Galli R, Del Carro U, Amadio S, Bergami A, Furlan R, Comi G, Vescovi AL, Martino G. 2003. Injection of adult neurospheres induces recovery in a chronic model of multiple sclerosis. Nature 422(6933):688-694.

Rafei M, Birman E, Forner K, Galipeau J. 2009a. Allogeneic mesenchymal stem cells for treatment of experimental autoimmune encephalomyelitis. Molecular therapy 17(10):1799-1803.

Rafei M, Campeau PM, Aguilar-Mahecha A, Buchanan M, Williams P, Birman E, Yuan S, Young YK, Boivin MN, Forner K, Basik M, Galipeau J. 2009b. Mesenchymal stromal cells ameliorate experimental autoimmune encephalomyelitis by inhibiting CD4 Th17 T cells in a CC chemokine ligand 2-dependent manner. Journal of immunology 182(10):5994-6002.

Rasmusson I. 2006. Immune modulation by mesenchymal stem cells. Experimental cell research 312(12):2169-2179.

Rasulov MF, Vasilenko VT, Zaidenov VA, Onishchenko NA. 2006. Cell transplantation inhibits inflammatory reaction and stimulates repair processes in burn wound. Bulletin of experimental biology and medicine 142(1):112-115.

Schrepfer S, Deuse T, Reichenspurner H, Fischbein MP, Robbins RC, Pelletier MP. 2007. Stem cell transplantation: the lung barrier. Transplantation proceedings 39(2):573-576.

Scolding N, Marks D, Rice C. 2008. Autologous mesenchymal bone marrow stem cells: practical considerations. Journal of the neurological sciences 265(1-2):111-115.

Semedo P, Wang PM, Andreucci TH, Cenedeze MA, Teixeira VP, Reis MA, Pacheco-Silva A, Camara NO. 2007. Mesenchymal stem cells ameliorate tissue damages triggered by renal ischemia and reperfusion injury. Transplantation proceedings 39(2):421-423.

Sordi V. 2009. Mesenchymal stem cell homing capacity. Transplantation 87(9 Suppl):S42-45.

Stewart K, Monk P, Walsh S, Jefferiss CM, Letchford J, Beresford JN. 2003. STRO-1, HOP-26 (CD63), CD49a and SB-10 (CD166) as markers of primitive human marrow stromal cells and their more differentiated progeny: a comparative investigation in vitro. Cell and tissue research 313(3):281-290.

Tatlisumak T, Fisher M. 2006. Handbook of Experimental Neurology: Methods and Techniques in Animal Research. Cambridge: Cambridge University Press. p 579.

Troyer DL, Weiss ML. 2008. Wharton's jelly-derived cells are a primitive stromal cell population. Stem cells 26(3):591-599.

Tyndall A, Walker UA, Cope A, Dazzi F, De Bari C, Fibbe W, Guiducci S, Jones S, Jorgensen C, Le Blanc K, Luyten F, McGonagle D, Martin I, Bocelli-Tyndall C, Pennesi G, Pistoia V, Pitzalis C, Uccelli A, Wulffraat N, Feldmann M. 2007. Immunomodulatory properties of mesenchymal stem cells: a review based on an interdisciplinary meeting held at the Kennedy Institute of Rheumatology Division, London, UK, 31 October 2005. Arthritis research & therapy 9(1):301.

Wakitani S, Saito T, Caplan AI. 1995. Myogenic cells derived from rat bone marrow mesenchymal stem cells exposed to 5-azacytidine. Muscle & nerve 18(12):1417-1426.

Weissleder R, Stark DD, Engelstad BL, Bacon BR, Compton CC, White DL, Jacobs P, Lewis J. 1989. Superparamagnetic iron oxide: pharmacokinetics and toxicity. American Journal of Roentgenology 152(1):167-173.

Wislet-Gendebien S, Wautier F, Leprince P, Rogister B. 2005. Astrocytic and neuronal fate of mesenchymal stem cells expressing nestin. Brain research bulletin 68(1-2):95-102.

Woodbury D, Reynolds K, Black IB. 2002. Adult bone marrow stromal stem cells express germline, ectodermal, endodermal, and mesodermal genes prior to neurogenesis. Journal of neuroscience research 69(6):908-917.

Yen AH, Sharpe PT. 2008. Stem cells and tooth tissue engineering. Cell and tissue research 331(1):359-372.

Zappia E, Casazza S, Pedemonte E, Benvenuto F, Bonanni I, Gerdoni E, Giunti D, Ceravolo A, Cazzanti F, Frassoni F, Mancardi G, Uccelli A. 2005. Mesenchymal stem cells ameliorate experimental autoimmune encephalomyelitis inducing T-cell anergy. Blood 106(5):1755-1761.

Chapter 8

General discussion

MRI has become one of the most important inventions in medical imaging of the twentieth century. Whereas in its early days MRI was primarily used for anatomical imaging, its role in biomedical research has expanded over the past 15 years (Hu and Norris, 2004). It is a non-invasive and risk-free method for the visualisation of soft tissues in different anatomical planes. MRI is often used as a diagnostic or monitoring tool to visualize morphological alterations in organs due to disease, but also changes in signal intensities can be indicative for ongoing pathological conditions. With regard to exquisite tissue contrast, the use of contrast agents offer specific tissue enhancement after administration. These substances are known to shorten the relaxation decay times what results in hyper- or hypo-intensity on T1- or T2-weighted images respectively (Lin et al., 2008; Runge, 2008). A lot of effort is put nowadays in the development of improved and innovative contrast particles. MR applications remained not limited to conventional MR images but also new techniques such as functional MR (fMRI), diffusion MRI (DWI), diffusion tensor imaging (DTI) or single voxel spectroscopy (MRSI) were introduced within a short time frame to study the inside human body (Bammer et al., 2005).

MRI has not only evolved into an essential instrument for routine clinical diagnosis but also turns out to be an interesting tool for biomedical research. The ability to spatially localize even subtle morphological changes or targeted contrast particles, which get hooked to cells or molecules of interest, leads to a better understanding of disease mechanisms and the development/evaluation of potential therapeutic treatments. MR images can be obtained from in vitro tissue specimens as well as from living animals. The capacity to perform repeated imaging of the same animal enables to study the evolution of disease progression or treatment. The majority of biomedical experiments make use of rodents because they are easy to keep and breed, share basic biology and chemistry with humans and the broad availability of genetically engineered strains. Therefore, small rodent MRI is playing now an increasingly important role as a non-invasive imaging modality in biomedical research.

Rat brain and spinal cord architecture studied by means of high resolution MRI

As for clinical applications, biomedical research MRI of small rodents will primarily focus on detecting morphological deviations and disease related changes in signal intensity compared to normal healthy animals. Therefore it is highly desirable to have a set of reference MR images of the studied anatomical structures before screening diseased animals. Such a reference frame allows to determine the normal morphometric parameters of anatomical structures, such as distance, height, width, area and even volume, but also to show the expected signal intensities for differently weighted pulse-sequences. This since contrast in MRI images can be introduced in several ways as there are for example: differences in local water amount (PD-weighting), differences in local relaxation (T1 and T2 weighting), differences in local diffusion properties (diffusion-weighted). Since MRI can produce anatomical images of any soft tissue by looking at the signals emanating from the hydrogen atoms of mobile molecules in biological tissues (mostly water), it provides an excellent method for imaging of the central nervous tissue of small rodents in both the *ex vivo* and *in vivo* setting.

In this work it is shown that the MRI-based reference frame of the rat's central nervous system offers a well established data set depicting high anatomical details of the brain and spinal cord (fixed and unfixed tissue) in different slice directions and contrast settings, i.e. PD- and T2-weighted sequences. This extended set of high resolution reference images can be used to identify structural abnormalities or changes in signal intensities related to pathological conditions. The TR value of 2500 ms and the TE values of 18 and 55 ms used for PD- and T2-imaging of unfixed CNS tissue, respectively, resulted in qualitative images with maximal overall (anatomical) structure delineation. Therefore, these values provide a good guideline, but need to be further optimized when focussing on a specific anatomical structure. The same holds for the TE value of 35 ms used for T2-weighted imaging of fixed tissue. Although many anatomical structures were depicted with these basic contrast weightings,

it was not possible to delineate the individual layers of the hippocampus based on endogenous contrast signals or to identify separate thalamic nuclei or brain stem nuclei. Other MR based imaging modalities such as diffusion weighted MRI might offer more detailed information.

Both formalin fixed and unfixed CNS tissue was used to create the reference frame and both methods have advantages and disadvantages which have to be taken into account when determining the experimental set-up of an MRI experiment. Tissue fixation results in improved contrast between gray and white matter structures and allows longer scan times in the *post-mortem* imaging setting. On the other hand, MR images of unfixed tissue show signal intensities that will be closer related to the signal intensities of *in vivo* imaging. However, *post-mortem* imaging of unfixed tissue, even cooled at 4°C, is limited in scan time (24 – 48 hours) due to tissue degeneration. Although *in vivo* imaging is even more restricted in acquisition time, it provides the advantage to follow-up the same animal in time. The TR and TE values used for optimal overall contrast in unfixed tissue are good starting values for *in vivo* imaging, but will need specific fine tuning depending on the anatomical structure in focus.

As an example regarding the anatomical details that can be obtained by high-resolution MRI, the pituitary gland of the rat was studied in more detail. The presented high resolution MR images contribute to the interpretation of the spatial intracranial organization of the pituitary gland and its anatomical relation with the complete rat brain and this without physical slicing up of the brain tissue.

Since the proton density (M_0) is rather similar all over the PG, contrast in the images has to arise mainly from differences in local relaxation. High resolution T2-weighted MR images, acquired at 9.4T in the sagittal and axial planes and in the absence of contrast agents, can clearly delineate the three distinct lobes of the rat's pituitary gland, i.e. the posterior, the intermediate and the anterior lobe. T2-weighted imaging results in improved contrast differences between the three lobes compared to PD-weighted imaging. The differentiating signal

intensity observed for the three lobes is due to a different tissue organization which is reflected by the different T2-relaxation decay times. T1-weighted imaging showed similar signal intensities for the posterior and intermediate lobe making their distinction not possible with the current parameter settings. This is confirmed by the almost identical T1-value for these two lobes. The T1-value of the anterior lobe was different enough to distinguish this lobe from the intermediate and posterior lobe. Although the pituitary gland is very small in dimension and has many interfaces with other tissues of different magnetic susceptibility (bones of sella turcica and gland tissue), images quality did not suffer from these susceptibility artefacts.

It can be assumed that the TR and TE values of the reference frame are good starting values for *in vivo* imaging. As a confirmation, the T1- and T2-weighted *in vivo* images of the pituitary gland indeed revealed similar contrast intensities as *ex vivo* acquired images, although the TR and TE value were slightly adapted to reduce the scan time. It demonstrates the feasibility to obtain *in vivo* images of the rat brain with good resolution and contrast within a relative short acquisition time. This makes high field MRI a powerful tool to reveal morphological or pathological abnormalities of the pituitary gland in rat animal models. Moreover, this study provides new perspectives for *in vivo* functional exploration of PG pathologies in rat animal models.

Post-mortem high resolution MRI of spinal cord injury. Qualitative correlation with histology and its relevance for morphometric analysis of lesioned spinal cord

A lot of biomedical research is performed on rat animal models in order to understand lesion development and mechanisms of natural recovery after spinal cord injury, but also to evaluate new therapeutic strategies to improve recovery and life quality (Basso, 2000). In many of these studies, it was demonstrated that remaining spared tissue after SCI was able to mediate some recovery of

function (Basso et al., 1996). Therefore, new therapeutic approaches can focus on different aspects aiming to improve functional outcome after SCI. In order to evaluate the potential effect of these interventions, it is necessary to measure the lesion size or the amount of preserved white or gray matter. The axial topography of injury appears particularly interesting, because the different motor fibre tracts that drive locomotion run in defined areas in the spinal cord white matter funiculi (Matesz et al., 2002; Webb and Muir, 2004).

The present investigation has demonstrated that *post*-mortem MR imaging of spinal cord injury in rats provides useful information regarding lesion severity and progression over time and shows the precision of detection of preserved white matter in its anatomical setting. Hereto, a partial low thoracic spinal cord injury, induced by the subdural balloon compression technique, was created in rats. Their locomotor behaviour was weekly determined. At different survival times, ranging from 1 dpo to 60 dpo, animals were sacrificed and submitted to MRI. MR images of injured spinal cord with high contrast and resolution can be acquired within short time. Lesion components are depicted using PD weighting. While haemorrhage is hypo-intense, oedema and necrosis / scarring processes were shown as hyper-intensities but could not be distinguished with the present acquisition sequences.

Inversion recovery MRI offers a strong support to fast, medium resolution PD MR images for visualizing white matter after experimental compressive SCI. Each tissue has a specific T1 relaxation decay time due to the specific degree of structuration of the tissue. With IR imaging, one can "remove" the signal from a specific tissue by choosing a well-selected inversion recovery time (TI) in the IR sequence. This results in a very hypo-intense signal intensity for the corresponding tissue in the image. PD and IR images were used simultaneously to define a very hypo-intense IR signal as spared white matter when this hypo-intensity was not seen in the PD images. Hypo-intensities present in IR as well as in PD images were considered to be due to the presence of iron, i.e. secondary to haemorrhage. IR images also increased the contrast between the in IR images hypo-intense normal white matter and very discrete white matter

changes, almost imperceptible and difficult to interpret on PD images. Histology confirmed that IR enhanced the detection of pathological changes in white matter. The behavioural observations of rats with clearly different lesion intensities (determined as morphometric parameters) varied from moderate to rapid recovery of normal locomotion. The quantitative information provided by IR supported PD MRI about white matter sparing as well as the other morphometric parameters assessed, i.e. lesion size and cord atrophy, compared well with the locomotor recovery patterns: rats with the lowest amount of white matter sparing performed worst, and vice versa. The extent of this correlation needs to be investigated further in the future and it should be attempted to transfer the described set-up to the in vivo setting.

Applying the MRI reference frame to detect the infiltration kinetics of SPIO labeled immune cells in the EAE animal model for MS

The high resolution MRI reference set of images obtained from healthy rats CNS was applied to evaluate the presence and spatial location of contrast labeled immune cells as demonstrated in chapter 6. It offers not only the establishment of changes in signal intensity, but also provides accurate spatial information.

Post-mortem high resolution T2-weighted MRI of EAE animals, which are injected with USPIO at different time points during the disease course, demonstrates that monocytes are recruited to different inflamed regions of the CNS during the time course of the disease. Knowledge about the spatio-temporal distribution of these cells contributes to improved insights about the disease mechanism of EAE and eventually multiple sclerosis (Baeten et al., 2008). This study further shows the potential of the MRI technique to visualize SPIO labeled myelin reactive T cells in the spinal cord and brain of recipient rats after administration. Different infiltration patterns of autoreactive T cells into the CNS were revealed in naive and EAE rats. T2-weighted imaging detected clusters of SPIO labeled cells. For these experiments, a TE value of 60 ms was used for

the T2-weigthing to improve the detection of hypo-intense signal intensities corresponding to SPIO labeled immune cells. The presence of SPIO labeled T cells was also confirmed by histological double staining (dextran and CD3) afterwards. The hypo-intense regions on the MR images corresponded with the histological findings. These results open new perspectives to investigate the role of different T cell subsets and to evaluate new MS therapies by means of MRI (Baeten et al., 2009).

Visualization of labeled mesenchymal stem cells by MRI

The use of MSCs for cell-based therapies relies on the capacity of these cells to home and engraft on long term into the appropriate target tissue. It is likely that injured tissues express specific receptors or ligands to facilitate trafficking, adhesion and infiltration of MSCs to the site of injury (Sordi, 2009). A better understanding of the MSCs homing mechanisms may lead to the development of therapeutic strategies with the potential to improve clinical applications of MSCs. MRI has proven to be a reliable tool for visualizing migration and homing of administred SPIO labeled cells as shown in chapter 6. The feasibility of labeling murine MSCs with commercially available contrast particles (SPIO) and the administration of labeled MSCs via intravenous injection were investigated in chapter 7. The results of this study demonstrated the ability to label murine MSCs efficiently with commercially available (FDA approved) ferumoxides (SPIO) and PLL as a transfection agent. Incubating MSCs for 24 hours with a mixture of 25 µg SPIO/ml and 0.75 µg PLL/ml resulted in labeled cells with sufficient amount of contrast particles and unaltered cell viability. To elucidate whether labeled MSCs migrate and home to injured and inflamed tissue, SPIO labeled MSCs were intravenously injected in EAE mice. Although such a systemic delivery technique of MSCs in mice seems to be successfully used by some other groups, we were not able to show the biodistribution of injected labeled MSCs because they were strongly trapped in the microcirculation of the lung leading to death (Gerdoni et al., 2007; Fischer et al., 2009).

As an alternative experimental setting to deliver the MSCs in close proximity of the inflamed CNS, the feasibility of an IC injection with contrast labeled MSCs was investigated. These preliminary results show that MSCs injected in the subarachnoid space of healthy mice can migrate towards the brain stem. However, since only few contrast labeled cells are present, no matching hypo-intensities can be detected on MR-images because the MR technique is not sensitive enough to detect single cells. Moreover, the locations where hypo-intensities should be detected on the MR images (based on histology and fluorescence images) corresponded to areas where haemorrhage (hypo-intense on MRI) occurred due to the injection of the labeled MSCs or to sites in close proximity to the skull bones (hypo-intense on MRI).

As a future perspective, these IC injection experiments can be performed with EAE animals since inflammation might lead to enhanced MSCs migration towards the lesions in the brain stem tissue. Also longer infiltration periods (longer than 24 hours) can be considered in this respect. To improve the detection of injected cells by MRI in future experiments, MSCs can also be tagged with double contrast labels, i.e. gadolinium (Gd) and SPIO particles. This might provide a method to discriminate between Gd labeled cells (hyper-intense) and haemorrhages (hypo-intense) on T1-weighted images. The SPIO particles, on the other hand, can be used to trace labeled cells once they have migrated away from the injection site. Although labeling cells with SPIO is an interesting cellular imaging modality, caution must be taken. Upon cell death of SPIO labeled cells, the SPIO particles might be taken up by resident phagocytic cells, resulting in non-specific macrophage labeling. Another drawback is that the average intracellular contrast agent concentration is diluted by every cell division, which tend to diminish the image contrast of the cells over time. The SPIO particles might also degrade in the lysosomal compartments of the cells leading to the disappearance of the hypo-intense MR signal.

As a second alternative setting to deliver the MSCs in the proximity of the inflamed CNS, the use of a spinal cord injury model is suggested. In such a model there is only injury at a single, well-defined location in the spinal cord.

This single target location facilitates the evaluation of the migration capacity of perilesional injected (double) labeled MSCs by MRI.

Future experiments may also focus on modifying the expression of functional chemokine receptors on MSCs in order to enhance the migration potential of MSCs, as it is hypothesized that the homing of MSCs is regulated by reciprocal interaction of chemokine receptors and gradients of chemoattractants. Increasing the portion of MSCs that find their way to the targets in the CNS will not only influence the clinical outcome, but also offers new strategies where MSCs can be used as vehicles to deliver neurotrophic factors or other beneficial molecules that promote tissue repair.

Conclusions

This work comprises a large diversity of biomedical application fields that benefit from complementary high resolution MRI. As increasing numbers of small animal models are in use in the field of neuroscience research, high resolution MRI provides an excellent method for non-invasive imaging of the central nervous tissue. Depending on the research question to be answered, MRI shows to be very efficient when applying the correct choice of acquisition conditions. Moreover, by incorporating contrast particles into the cells of interest, specific cells can be visualized and tracked by MRI. The non-invasiveness and the richness of the information that is obtained explain the important role of MR in biological and biomedical research.

Not only high resolution *in vivo* small animal imaging is gaining more interest, but also human scanners with high magnetic field strengths (> 3 T) are more and more introduced in the clinic for acquiring high quality, high resolution images. There are currently more than thousand 3 T MRI scanners and about thirty 7 T clinical MRI systems in use - or about to be installed - around the world, more than half of it in Europe. Two 9.4 T human MRI scanners are

already operating in Germany, while France will soon install an 11.7 T clinical MRI system (Vedrine et al., 2008). Imaging at high field increases the SNR, improves anatomic resolution and reduces scan time while preserving image quality. Moreover, even very fine lesions as well as biochemical reactions become detectable. This opens perspectives to treat frequently occurring diseases such as cancer, dementia, myocardial infarction, diabetes and other serious diseases in an earlier stage, and so should result in less burden to the human organism.

References

Baeten K, Hendriks JJ, Hellings N, Theunissen E, Vanderlocht J, Ryck LD, Gelan J, Stinissen P, Adriaensens P. 2008. Visualisation of the kinetics of macrophage infiltration during experimental autoimmune encephalomyelitis by magnetic resonance imaging. Journal of neuroimmunology 195(1-2):1-6.

Baeten K, Adriaensens P, Hendriks JJA, Theunissen E, Gelan J, Hellings N and Stinissen P. Tracking of myelin-reactive T cells in EAE animals using small particles of iron oxide and MRI. NMR in biomedicine. Published Online: Apr 2010. DOI: 10.1002/nbm.1501

Bammer R, Skare S, Newbould R, Liu C, Thijs V, Ropele S, Clayton DB, Krueger G, Moseley ME, Glover GH. 2005. Foundations of advanced magnetic resonance imaging. NeuroRx 2(2):167-196.

Basso DM. 2000. Neuroanatomical substrates of functional recovery after experimental spinal cord injury: implications of basic science research for human spinal cord injury. Physical therapy 80(8):808-817.

Basso DM, Beattie MS, Bresnahan JC. 1996. Graded histological and locomotor outcomes after spinal cord contusion using the NYU weight-drop device versus transection. Experimental neurology 139(2):244-256.

Fischer UM, Harting MT, Jimenez F, Monzon-Posadas WO, Xue H, Savitz SI, Laine GA, Cox CS, Jr. 2009. Pulmonary passage is a major obstacle for intravenous stem cell delivery: the pulmonary first-pass effect. Stem cells and development 18(5):683-692.

Gerdoni E, Gallo B, Casazza S, Musio S, Bonanni I, Pedemonte E, Mantegazza R, Frassoni F, Mancardi G, Pedotti R, Uccelli A. 2007. Mesenchymal stem cells effectively modulate pathogenic immune response in experimental autoimmune encephalomyelitis. Annals of neurology 61(3):219-227.

Hu X, Norris DG. 2004. Advances in high-field magnetic resonance imaging. Annual review of biomedical engineering 6:157-184.

Lin MM, Kim do K, El Haj AJ, Dobson J. 2008. Development of superparamagnetic iron oxide nanoparticles (SPIONS) for translation to clinical applications. IEEE transactions on nanobioscience 7(4):298-305.

Matesz C, Bacskai T, Nagy E, Halasi G, Kulik A. 2002. Efferent connections of the vestibular nuclei in the rat: a neuromorphological study using PHA-L. Brain research bulletin 57(3-4):313-315.

Runge VM. 2008. Advances in magnetic resonance (2008). Investigative radiology 43(12):893-898.

Sordi V. 2009. Mesenchymal stem cell homing capacity. Transplantation 87(9 Suppl):S42-45.

Vedrine P, Aubert G, Beaudet F, Belorgey J, Beltramelli J, Berriaud C, Bredy P, Chesny PH, Donati A, Gilgrass G, Grunblatt G, Juster FP, Molinie F, Meuris C, Nunio F, Payn A, Quettier L, Rey JM, Schild T, and Sinanna A. 2008. "The whole body 11.7 T MRI magnet for Iseult/INUMAC project," IEEE transactions on applied superconductivity 18:868-873.

Webb AA, Muir GD. 2004. Course of motor recovery following ventrolateral spinal cord injury in the rat. Behavioural brain research 155(1):55-65.

Nederlandse samenvatting

Magnetische resonantie imaging (MRI) is één van de belangrijkste innovaties geweest voor de medische beeldvorming in de twintigste eeuw. In de begin jaren tachtig werd MRI voornamelijk gebruikt voor anatomische beeldvorming, maar in de afgelopen 15 jaar is het gebruik van MRI in de biomedische onderzoekswereld sterk toegenomen. Het is een niet-invasieve en onschadelijke methode voor het visualiseren van zachte weefsels in verschillende anatomische vlakken. MRI wordt vaak toegepast om een diagnose te stellen maar kan ook als een observatiemethode worden gebruikt. Hiertoe worden morfologische veranderingen in aangetaste organen in beeld gebracht en kunnen afwijkende signaalintensiteiten eveneens wijzen op mogelijke pathologie. Contraststoffen worden gebruikt om bepaalde weefsels beter in beeld te brengen omdat ze de relaxatietijd van de proton spins in de weefsels verkorten. Deze verkorte relaxatietijden resulteren in hyper- en hypo-intensiteiten op T1- of T2-gewogen beelden, respectievelijk. Tegenwoordig wordt veel onderzoek gedaan naar de ontwikkeling van verbeterde en vernieuwende contrastdeeltjes. Naast de conventionele MR beelden werden er ook andere MR gebaseerde technieken ontwikkeld om het menselijk lichaam te bestuderen, zoals functionele MRI (fMRI), diffusie MRI (DWI), diffusie tensor imaging (DTI) en single voxel spectroscopie (MRSI).

MRI is niet enkel een essentieel instrument voor de dagelijkse klinische diagnostiek geworden, maar blijkt ook een waardevolle functie te hebben in biomedisch onderzoek. De mogelijkheid om subtiele morfologische veranderingen of contrastdeeltjes, die doelgericht aan cellen of moleculen zijn gehecht, ruimtelijk te lokaliseren, leidt tot een beter inzicht in ziektemechanismen en draagt ook bij tot de ontwikkeling en evaluatie van therapieën. MRI beelden kunnen zowel *ex vivo* als *in vivo* worden opgenomen. Deze beeldvormingtechniek maakt het mogelijk om herhaaldelijk beelden te maken van hetzelfde dier. Hierdoor kan het verloop van de ziekte of behandeling beter worden bestudeerd. Bij het merendeel van de biomedische experimenten gebruikt men knaagdieren omdat men deze gemakkelijk kan onderhouden en kweken. Bovendien heeft men een groot aantal genetisch gemodificeerde knaagdierstammen ter beschikking voor onderzoek. Hierdoor wint de beeldvor-

ming van kleine knaagdieren nog steeds aan belang in de biomedische onderzoekswereld.

Het centraal zenuwstel van de rat in beeld gebracht door MRI

Zoals voor de klinische toepassingen, zal MRI in het biomedisch onderzoek ook vooral worden toegepast om morfologische afwijkingen en ziektegerelateerde signaalveranderingen te detecteren. Daarom is het noodzakelijk om referentie MR beelden van gezonde dieren te hebben alvorens men pathologie in dieren kan opsporen door middel van MRI. Een referentieatlas maakt het mogelijk om normale morfometrische parameters, zoals afstand, hoogte, breedte, oppervlakte en zelfs volume van anatomische structuren te bepalen. De te verwachten signaalintensiteiten voor verschillende pulssequenties kunnen eveneens in kaart worden gebracht. Hierbij moet men weten dat er verschillende contrastvormen voor MR beelden kunnen worden gebruikt die gebaseerd kunnen zijn op verschillen in lokale waterhoeveelheid (proton densiteitweging), verschillen in lokale relaxatie (T1- en T2-weging) of verschillen in lokale diffusie-eigenschappen (diffusie-gewogen beelden). MRI beschikt over de mogelijkheid om anatomische beelden te creëren van zachte weefsels omdat een MR beeld gebaseerd is op signalen afkomstig van mobiele waterstofatomen, die overvloedig aanwezig zijn in biologische weefsels. Hierdoor is zowel *in vivo* als *ex vivo* MRI uitermate geschikt om het centraal zenuwweefsel van kleine knaagdieren in beeld te brengen.

Deze thesis toont aan dat de referentieatlas, bestaande uit MR beelden van het centraal zenuwstelsel van de rat, een zeer nauwkeurige beeldendatabank vormt waarin zeer precieze details van de hersenen en ruggenmerg in verschillende anatomische vlakken en contrasten, zoals proton densiteit (PD), inversion recovery (IR) en T2-contrast, zijn gebundeld. Deze uitgebreide set referentiebeelden kan worden gebruikt om structurele abnormaliteiten en afwijkende signaalintensiteiten gerelateerd aan een pathologie te detecteren. De TR waarde van 2500 ms en de TE waarden van 18 en 55 ms, respectivelijk

gebruikt voor PD- en T2-gewogen beelden van niet-gefixeerd CZS weefsel, leveren kwalitatieve MR beelden op met maximaal contrast tussen de anatomische structuren. Daarom kunnen deze opnameparameters worden gezien als een richtlijn, maar zullen toch best worden geoptimaliseerd wanneer men een specifieke anatomische structuur in beeld wilt brengen. Hetzelfde geldt voor de TE waarde van 35 ms die gebruikt wordt bij T2-gewogen opnames van gefixeerd weefsel. Hoewel veel anatomische structuren zichtbaar zijn met deze standaard contrastwegingen, is het toch niet mogelijk om de individuele lagen van de hippocampus in beeld te brengen. De afzonderlijke thalamuskernen en hersenstamkernen waren ook niet zichtbaar. Andere MR gebaseerde beeldvormingstechnieken zoals diffusie-gewogen beelden kunnen hier misschien een oplossing bieden.

Zowel formaline gefixeerd als niet-gefixeerd CZS weefsel werd gebruikt om het referentiekader op te stellen. En beide methodes hebben ieder hun voor- en nadelen die moeten worden afgewogen bij het opstellen van MRI experimenten. Het fixeren van weefsel leidt tot een verbeterd contrast tussen grijze en witte stof structuren en laat ook toe om langere opnametijden te gebruiken. Maar aan de andere kant, tonen MR beelden van niet-gefixeerd weefsel signaal-intensiteiten die meer overeenkomen met de signaalintensiteiten van *in vivo* MRI. Hierbij moet wel worden opgemerkt dat *post-mortem* MRI van niet-gefixeerd weefsel, zelfs gekoeld bij 4°C, beperkt is in opnametijd (24-48 uren) omdat er weefseldegeneratie optreedt. Hoewel de opnametijd bij *in vivo* imaging nog meer is gelimiteerd, heeft men hier wel het voordeel om hetzelfde dier in functie van de tijd op te volgen. De TR en TE waardes, die hier werden gebruikt voor de MR opnames van niet-gefixeerd weefsel, zijn goede startwaardes voor *in vivo* MRI, maar dienen vanzelfsprekend best verder geoptimaliseerd te worden indien men op een welbepaalde structuurfacet focust.

Als case-studie voor het aantonen van de anatomische details, waarneembaar met hoge resolutie MRI, werd de hypofyse van de rat gedetailleerd bestudeerd en beschreven. De hoge resolutiebeelden dragen bij tot het interpreteren van de ruimtelijke organisatie van de hypofyse en de relatie tot de rest van de hersenen zonder hiervoor het weefsel te moeten versnijden of herpositioneren.

Aangezien alle kwabben van de hypofyse ongeveer dezelfde waarden hebben voor de proton densiteit (M_0), zal contrast vooral worden bepaald door locale relaxatieverschillen. Hoge resolutie T2-gewogen (sagittale en coronale) MR beelden, gemaakt zonder contrastmiddelen, laten duidelijk drie verschillende kwabben van de hypofyse van de rat zien, i.e. de posterior, de intermediaire en de anterior kwab. T2-gewogen beelden tonen duidelijk een beter contrast tussen de 3 lobben in vergelijking met PD-gewogen beelden. De verschillende signaalintensiteiten van de drie kwabben op T2-gewogen beelden worden veroorzaakt door een verschil in weefselorganisatie. Dit wordt weerspiegeld door de verschillende T2-relaxatietijden voor iedere kwab. T1-gewogen beelden in dit werk tonen geen verschil in signaalintensiteit tussen de posterior en intermediaire kwab. Dit wordt bevestigd door de bijna identieke T1-waardes van deze twee kwabben. De T1-waarde van de anterior kwab wijkt genoeg af van de andere twee lobben waardoor deze anterior kwab duidelijk onderscheiden kan worden. Hoewel de hypofyse zeer kleine afmetingen heeft en er bovendien ook veel weefselovergangen zijn tussen bot en hypofyseweefsel, werd de beeldkwaliteit toch niet verstoord door susceptibiliteitartefacten.

Men neemt aan dat de TR en TE waardes van het referentiekader goede startwaardes zijn voor *in vivo* MRI. Dit werd bevestigd in dit werk door T1- en T2-gewogen *in vivo* opnames van de hypofyse. De kwabben van de hypofyse tonen dezelfde signaalintensiteiten als bij *ex vivo* opnames, hoewel de TR en TE waardes een beetje werden aangepast om de *in vivo* opnametijd te verminderen. Dit alles maakt hoge veldsterkte MRI een krachtig instrument om morfologische afwijkingen en pathologische veranderingen van de hypofyse in beeld te brengen. Bovendien leidt deze studie tot nieuwe perspectieven voor de *in vivo* exploratie van hypofyse pathologieën in diermodellen van ratten.

Post-mortem hoge resolutie MR beelden van ruggenmergletsels. Een kwalitatieve correlatie met histologie en haar bijdrage voor morfometrische analyse van beschadigd ruggenmerg

Er wordt veel onderzoek gedaan naar diermodellen die een beter inzicht geven in het ontstaan van ruggenmergletsels en de mechanismen die kunnen bijdragen tot spontaan herstel van deze laesies. Daarnaast worden diermodellen ook gebruikt om nieuwe therapieën te evalueren die leiden tot een beter herstel of verbeterde levenskwaliteit. Veel van deze studies tonen aan dat het resterende intacte weefsel na een ruggenmerglaesie de mogelijkheid bezit om functioneel herstel te induceren. Nieuwe therapieën kun zich focussen op verschillende aspecten om het functioneel herstel te verbeteren na ruggenmergletsels. Om de efficiëntie van dit soort interventies te evalueren, is het noodzakelijk om de laesiegrootte of de hoeveelheid onbeschadigde witte of grijze stof te kunnen bepalen. Hiervoor blijkt de axiale topografie van de laesie de meest relevante kwantitatieve informatie te verstrekken omdat de verschillende motorische banen in specifieke gebieden van de witte stof in het ruggenmerg gelegen zijn.

In dit werk wordt er aangetoond dat *post-mortem* opgenomen MR beelden van ruggenmerglaesies in de rat waardevolle informatie geven over de ernst van de laesie en alsook over de veranderingen in de laesie in de tijd. De beelden tonen ook hoe gespaarde witte stof precies kan worden gevisualiseerd. Hiervoor werd een gedeeltelijke laesie aangebracht op een laag thoracaal ruggenmergniveau in de rat. De compressielaesie werd aangebracht door dilatatie van een subduraal geplaatste ballon. Het locomotorisch gedrag van de dieren werd wekelijks geëvalueerd. Na verschillende overlevingstijden, gaande van 1 dag tot 60 dagen na de operatie, werden dieren gedood en door middel van MRI onderzocht. MR beelden van het beschadigde ruggenmerg met hoog contrast en resolutie kunnen worden opgenomen in een korte tijdspanne. De laesiecomponenten worden op PD-gewogen beelden gevisualiseerd. Bloedingen zijn zichtbaar als hypo-intense gebieden. Oedeem en necrose/littekenvorming zijn hyper-intens, maar kunnen met de gebruikte beeldvormingssequentie niet van mekaar worden onderscheiden. IR-gewogen beelden met middelmatige resolutie bieden onmis-

bare ondersteuning aan de snel opgenomen PD-gewogen beelden wanneer intacte witte stof dient te worden gedetecteerd in de compressielaesie in het ruggenmerg. IR-gewogen beelden verhogen het contrast tussen de nu hypo-intense witte stof en zeer subtiele (hyper-intense) veranderingen in de witte stof, die bijna niet waarneembaar of moeilijk te interpreteren zijn op PD-gewogen beelden. Histologische beelden bevestigen dat IR-gewogen beelden de detectie van pathologische veranderingen verbetert. De ernst van de laesies verschilden duidelijk bij deze ratten. Hierdoor varieerde de herstelperiode van 2 tot 5 weken vooraleer normale locomotie werd geobserveerd. De kwantitatieve informatie, zijnde het bepalen van de intacte witte stof uit de IR ondersteunde PD beelden, maar ook van andere morfometrische parameters zoals laesiegrootte en atrofie, kwamen goed overeen met de locomotorische herstelpatronen: ratten met de kleinste hoeveelheid intacte witte stof vertoonden een minder goed herstel, en vice versa. Het belang van deze correlatie moet in de toekomst statistisch verder worden onderzocht evenals het transfereren van deze *ex vivo* methode naar een *in vivo* toepassing. Aangezien het in de nabije toekomst onwaarschijnlijk is dat *in vivo* MR beelden de kwaliteit van de huidige *ex vivo* MR beelden zullen benaderen, biedt deze *post-mortem* techniek vandaag de dag een enorme ondersteuning voor het onderzoek van ruggenmerglaesies.

Het aanwenden van de referentie MRI atlas om de kinetiek van infiltreren van SPIO gelabelde immuuncellen te bepalen in een EAE diermodel voor multiple sclerose

De referentiedatabank, bestaande uit hoge resolutie MR beelden van het centraal zenuwstelsel van de gezonde rat, werd gebruikt om de aanwezigheid en de ruimtelijke positie van contrast gelabelde cellen aan te tonen (Hoofdstuk 6). Het biedt niet alleen de mogelijkheid om veranderingen in signaalintensiteit op te sporen, maar levert ook nauwkeurige ruimtelijke informatie.

Post-mortem hoge resolutie T2-gewogen MR beelden van experimentele auto-immune encefalomyelitis (EAE) dieren, die werden geïnjecteerd met ultra small particles of iron oxide (USPIO) contrastdeeltjes op verschillende tijdstippen gedurende het ziekteproces, tonen aan dat monocyten worden gerekruteerd naar diverse inflammatoire gebieden in het CZS. Het achterhalen van de spatio-temporale verspreiding van deze cellen geeft een beter inzicht in het ziektemechanisme van EAE (en misschien zelfs ook van multiple sclerose). Verder ondersteunt deze studie ook dat MRI de mogelijkheid bezit om gelabelde myeline reactieve T-cellen te visualiseren bij ratten. Deze cellen worden na intraperitoneale injectie teruggevonden in het ruggenmerg en de hersenen van de rat. Verschillende infiltratiepatronen werden waargenomen in het CZS voor deze autoreactieve T-cellen al naargelang gebruik werd gemaakt van gezonde of EAE ratten. In T2-gewogen MRI beelden werden groepjes van SPIO gelabelde immuuncellen gevonden. Een TE waarde van 60 ms werd gebruikt in deze experimenten om de detectie van hypo-intense signalen, afkomstig van SPIO gelabelde cellen, te verbeteren. De aanwezigheid van SPIO gelabelde T-cellen werd histologisch bevestigd door een dubbelkleuring voor dextraan en CD3. The hypo-intense regio's, zichtbaar op de MR beelden, kwamen goed overeen met de histologische bevindingen. Deze kennis opent nieuwe perspectieven om de rol van de verschillende T-cel subtypes te ontrafelen alsook nieuwe therapieën voor EAE en multiple sclerose te evalueren door middel van MRI. Het labelen van cellen met SPIO deeltjes is dus een zeer informatieve cellulaire imaging methode die kennis verstrekt over de plaatsen waar specifieke cellen naar toe migreren na toediening. Controle moet echter ingebouwd worden m.b.t. specificiteit en selectiviteit om uit te sluiten dat de SPIO deeltjes niet vrijkomen uit de gelabelde cellen en opgenomen worden door andere naburige fagocyterende cellen zoals macrofagen.

De visualisatie van gelabelde mesenchymale stamcellen door middel van MRI

Het gebruik van mesenchymale stamcellen (MSCs) voor therapie hangt af van hun capaciteit om doelgericht naar specifieke weefsels te migreren en er langdurig te verblijven. Er wordt aangenomen dat beschadigde weefsels specifieke receptoren en stoffen tot expressie brengen waardoor MSCs gemakkelijker migreren, aanhechten en infiltreren in de aangetaste gebieden. Indien dit 'homing' mechanisme van MSCs kan worden achterhaald, kan dit leiden tot de ontwikkeling van nieuwe therapeutische strategieën die klinisch toepasbaar zijn. In hoofdstuk 6 werd aangetoond dat MRI uitermate geschikt is om de migratie en homing van gelabelde T-cellen te visualiseren. De haalbaarheid om MSCs van knaagdieren te labelen met commercieel beschikbare contrastdeeltjes (SPIO) werd in hoofdstuk 7 onderzocht alsook het toedienen van deze gelabelde MSCs langs intraveneuze weg.

Dit onderzoek geeft aan dat het mogelijk is om MSCs, afkomstig van muizen, efficiënt te labelen met commerciële (FDA goedgekeurde) ferumoxides (SPIO), gebruikmakend van PLL als transfectie-agentia. Wanneer MSCs gedurende 24 uur geïncubeerd worden met een mengsel van 25 µg SPIO/ml en 0.75 µg PLL/ml, worden gelabelde cellen verkregen waarin voldoende contrastdeeltjes zitten en waarvan de viabiliteit niet aangetast wordt. Om te achterhalen of de gelabelde MSCs naar beschadigde en ontstoken weefsels migreren en er ook infiltreren, werden deze gelabelde cellen intraveneus geïnjecteerd bij EAE muizen. Hoewel deze systemische toedieningmethode wordt beschreven door een aantal onderzoeksgroepen, kon de verspreiding van de gelabelde cellen niet worden gevolgd omdat de cellen in de longcirculatie bleven vastzitten waardoor de dieren niet overleefden.

De intracisternale (IC) injectie is een alternatieve methode om gelabelde MSCs in de nabijheid van inflammatoire gebieden in het zenuwweefsel te brengen. De voorlopige resultaten van ons onderzoek laten zien dat de gelabelde cellen, die in de subarachnoidale ruimte werden geïnjecteerd, mogelijks migreren naar de

hersenstam. Aangezien slechts een beperkt aantal gelabelde cellen werd gedetecteerd door middel van fluorescentie- en lichtmicroscopie, konden geen overeenkomstige hypo-intense spots worden gevonden op de MR beelden. MRI is niet gevoelig genoeg om individuele cellen te detecteren. Hierbij komt ook nog dat de gebieden waar de hypo-intensiteiten werden verwacht (gebaseerd op corresponderende histologische en fluorescentie beelden), overeenkwamen met gebieden waarin zich een bloeding had voorgedaan ten gevolge van de injectie, of die zeer dicht bij schedelbeenderen (die eveneens hypo-intens zijn op MR beelden) lagen.

Naar de toekomst toe kunnen deze IC injecties ook worden uitgevoerd op EAE dieren omdat de aanwezigheid van inflammatie kan leiden tot een toegenomen migratie van MSCs naar deze laesies in de hersenstam. Ook langere infiltratietijden (langer dan 24 uur) kunnen worden overwogen. Om het opsporen van geïnjecteerde cellen, gebruikmakende van MRI, nog te verbeteren, kunnen twee verschillende contrast labels in de MSCs worden aangebracht, zijnde gadolinium (Gd) en SPIO partikels. Op deze manier is het mogelijk om een onderscheid te maken tussen Gd gelabelde cellen (hyper-intens) en bloedingen (hypo-intens) op T1-gewogen beelden. De SPIO deeltjes kunnen worden gebruikt om de gelabelde cellen te volgen nà migratie uit de injectieplaats. Hoewel SPIO labeling een waardevolle cellulaire beeldvormingsmethode is, moet men toch aandachtig zijn betreffende selectiviteit en specificiteit. Wanneer bijvoorbeeld SPIO gelabelde cellen afsterven, kunnen de SPIO deeltjes door naburige macrofagen opgenomen worden en plaatsen aankleuren die niet het target vormden. Immunohistochemische controles worden dus best uitgevoerd. Een ander probleem wordt veroorzaakt door celdeling. Hierdoor wordt de SPIO concentratie verdeeld onder de dochtercellen waardoor de hoeveelheid contrastdeeltjes per cel gaat afnemen. SPIO deeltjes zouden ook kunnen afgebroken worden door de lysosomen van de gelabelde cel waardoor het hypo-intense signaal op het MR beeld verdwijnt.

Een ander alternatief om MSCs in de nabijheid van ontstoken CZS af te leveren, is een ruggenmerglaesie. In dit model is er één duidelijke targetplaats, zijnde de laesieplaats in het ruggenmerg. Dit welomschreven doelwit vergemakkelijkt het evalueren van de migratiecapaciteit van (dubbel) gelabelde cellen, die perilesionaal worden geïnjecteerd, door middel van MRI.

Toekomstige experimenten kunnen zich ook richten op de modificatie van de chemokinereceptor expressie op MSCs. Dit heeft als doel de migratiecapaciteit van de MSCs te verhogen omdat er wordt verondersteld dat de homing van MSCs wordt bepaald door wederzijdse interacties tussen chemokinereceptoren en de concentratie van chemoattractanten. Door het aantal MSCs te verhogen die selectief hun weg vinden naar hun doelwit in het CZS, kan enerzijds het klinische resultaat verbeterd worden. Anderzijds biedt dit ook de mogelijkheid om MSCs te gebruiken als transportmiddel om neurotrofe factoren of andere gunstige moleculen, die weefselherstel bevorderen, af te leveren.

Conclusies

Het werk in deze thesis omvat een grote diversiteit aan biomedische toepassingen die baat kunnen hebben bij het (complementair) gebruik van hoge resolutie MRI. Aangezien het aantal diermodellen dat wordt gebruikt in het neurowetenschappelijk onderzoek toeneemt, biedt hoge resolutie MRI zich aan als een uitstekende methode om het CZS op een niet-invasieve manier in beeld te brengen. Afhankelijk van de onderzoeksvraag, blijkt MRI zeer efficiënt te zijn wanneer de juiste beeldvormingcondities worden gekozen. Door doelgericht contrastdeeltjes in cellen te brengen, kunnen bovendien specifieke cellen gevisualiseerd en gevolgd worden door middel van MRI. Het niet-invasieve karakter en de overvloed aan informatie die wordt verkregen, bekrachtigen het belang van MRI in het biologisch en biomedisch onderzoek. Niet enkel hoge resolutie *in vivo* imaging van kleine dieren trekt veel aandacht, maar ook humane scanners met hoge veldsterkte (> 3T) worden steeds vaker in de kliniek gebruikt voor het maken van kwalitateitsvolle hoge resolutiebeelden. Er zijn

momenteel meer dan duizend 3T MRI scanners en ongeveer een dertigtal 7T scanners in gebruik wereldwijd, waarvan meer dan helft zich in Europa bevinden. Twee 9.4T humane MRI toestellen worden al gebruikt in Duitsland en in Frankrijk wordt er weldra een 11.7T systeem geïnstalleerd. het gebruik van magneten met een hogere veldsterkte zorgt voor een verbetering van de SNR, verhoging van de anatomische resolutie en vermindering van de opnametijd. Meer nog, zelfs zeer kleine laesies en biochemische reacties kunnen worden opgespoord. Kanker, dementheid, myocardinfarct, diabetes and andere ernstige aandoeningen zullen mogelijks in een vroeger stadium vastgesteld en behandeld kunnen worden, waardoor schade meer beperkt kan worden.

Curriculum Vitae

Theunissen Evi werd geboren op 17 oktober 1980 te Bilzen. In 1998 behaalde ze het diploma Algemeen Secundair Onderwijs (ASO) Latijn-Wiskunde (8 uur) aan het Heilig-Hart College te Lanaken. Datzelfde jaar vatte ze haar universitaire studies aan in de richting Biomedische Wetenschappen aan het Rijksuniversitair Centrum Antwerpen (RUCA). De licentiaatjaren volbracht ze in dezelfde richting aan de transnationale Universiteit Limburg (tUL) waar ze in 2003 haar diploma Licentiaat in de Biomedische Wetenschappen behaalde. Aan dezelfde instelling begon ze ook haar aggregaatsopleiding in 2002 en behaalde in 2004 het diploma Geaggregeerde voor het Secundair Onderwijs - groep 2 Biomedische Wetenschappen. In september 2003 startte ze als assistent morfologie aan de Universiteit Hasselt. Hier werkte ze gedurende 6 jaar aan haar doctoraat waarbij een uitgebreide samenwerking met het Instituut voor Materiaal Onderzoek (IMO) plaatsvond.

Bibliography

Scientific Articles:

Cauwenberghs S, Feijge MA, <u>Theunissen E</u>, Heemskerk JW, van Pampus EC, Curvers J. Novel methodology for assessment of prophylactic platelet transfusion therapy by measuring increased thrombus formation and thrombin generation. British journal of haematology. 2007;136(3):480-90.

Baeten K, Hendriks JJ, Hellings N, <u>Theunissen E</u>, Vanderlocht J, Ryck LD, Gelan J, Stinissen P, Adriaensens P. Visualisation of the kinetics of macrophage infiltration during experimental autoimmune encephalomyelitis by magnetic resonance imaging. Journal of neuroimmunology. 2008;195(1-2):1-6.

Scholtes F, Phan-Ba R, <u>Theunissen E</u>, Adriaensens P, Brook G, Franzen R, Bouhy D, Gelan J, Martin D, Schoenen J. Rapid post-mortem 9.4T MRI of SCI: correllation with histology and survival times. Journal of neuroscience methods. 2008;174:157-167.

<u>Theunissen E</u>, Baeten K, Vanormelingen L, Lambrichts I, Beuls E, Gelan J and Adriaensens P. Detailed visualization of the functional regions of the rat pituitary gland by high-resolution T2-weighted MRI. Anatomia histologia embroylogia. Published Online: Mar 11 2010 DOI: 10.1111/j.1439-0264.2010.00995.x.

Post-mortem assessment of rat spinal cord injury including white matter sparing with proton density based inversion recovery magnetic resonance imaging. Scholtes F, <u>Theunissen E</u>, Phan-Ba R , Adriaensens P, Brook G, Franssen R, Gelan J, Schoenen J, Martin D. Spinal cord. Under revision.

Oral Presentations:

Structure and white matter lesion appearance in Multiple Sclerosis by HR-MRI and immunohistochemistry.
One day symposium for Young Belgian magnetic resonance scientists (FWO)
Brussel – 26 november 2004

Cell therapy for multiple sclerosis
3de Young research club
Universiteit Antwerpen – 26 juni 2007

Immuno-suppressive capacity of hMSCs populations
2nd interuniversitary forum on stem cells
Universiteit Gent – 2 mei 2008

Poster Presentations:

Theunissen E, Adriaensens P, Baeten K, Gelan J, Lambrichts I, Vandenabeele F, Vandersteen M, Vanormelingen L and Beuls E.
High field MRI-study of the normal CNS of the Lewis rat.

- Workshop non-invasive 3D microscopy, Universiteit Antwerpen, 21 augustus 2004
- Cells at work III, MECC Maastricht, 15 november 2005
- French-Benelux meeting on magnetic resonance, Blankenberge, 19 / 22 maart 2006
- Dag van het onderzoek, Universiteit Hasselt, 23 november 2006

<u>Theunissen E</u>, Liang X, Martens W, Struys T, Vandersteen M, Lippens P, Adriaensens P, Gelan J , Jacobs R, Lambrichts I.

High-resolution MRI of rat masticatory system.

- 10th European congress of dentomaxillofacial radiology, Leuven, 1 -3 juni 2006

<u>Theunissen E</u>, Moreels M, Baeten K, Adriaensens P, Ponsaerts P, D'Haen J, Beuls E, Hellings N.

Morphological characterisation of eGFP electroporated hMSCs.

- Exploring materials, living systems & their interactions (BSM), Universiteit Luik, 16 november 2007

<u>Theunissen E</u>, Moreels M, Baeten K, Vanormelingen L, Ponsaerts P, Lambrichts I, Hellings N.

SPIO labeling capacity of hMSCs: application for SC tracking in EAE.

- MS-onderzoeksdagen, Hasselt, 15 - 16 november 2007
- 3rd ITERA workshop, Maastricht, 25 - 26 oktober 2007
- First Benelux in vivo MR methods symposium, Berg en Dal, 12 december 2007
- Spring meeting 2008 – the adult stem / progenitor cell niche (BVCOB), VUB Brussel, 13 - 15 maart 2008
- Knowlegde for growth, Gent, 6 juni 2008
- 2nd International Congress on Stem Cells and Tissue Formation, Dresden, 6 – 9 juli 2008

<u>Theunissen E</u>, Scholtes F, Baeten K, Phan-Ba R, Guedens W, Gelan J, Adriaensens P.

Relevance of IR-imaging at 9.4T in determining spared WM after SCI.

- Euromar 2008, Sint-Petersburg, 6 - 11 juli 2008

<u>Theunissen E</u>, Moreels M, Ponsaerts P, Lambrichts I, Bollen B, Adriaensens P, Hellings N.

Mesenchymal stromal cells derived from bone marrow and Wharton's Jelly as potential sources for cell-based therapies in multiple sclerosis.

- WCTRIMS, Montreal, 17 - 20 september 2008
- Knowlegde for growth, Gent, 7 mei 2009

Dankwoord

Het is bizar dat de meest gelezen pagina's van een proefschrift niet meetellen in de beoordeling van een promotie. En het is niet voor niets dat precies deze pagina's het dankwoord bevatten. Hoe kan je nu in een paar zinnen iedereen bedanken die een steentje heeft bijgedragen tot het voltooien van deze doctoraatsthesis? Op mijn weg ben ik tal van mensen tegengekomen die elk individueel een speciaal woordje van dank verdienen. Velen hebben ooit wel eens gevraagd: "Hoe is het nu? Vordert het een beetje?". En ook al was het niet altijd eenvoudig om uit te leggen hoe het nu werkelijk zat, deze blijk van interesse door velen, zorgde voor nieuwe brandstof om door te zetten!

Een eerste woord van dank gaat uit naar mijn promotoren, Prof. Dr. Peter Adriaensens en Prof. Dr. Sven Hendrix. Peter heeft me zes jaar lang bijgestaan in dit onderzoek. In de beginjaren heeft hij me vooral gestuurd en op de juiste weg gezet door me uitgebreid in te wijden in de theorie en praktijk van de MRI. Hierdoor kon ik uiteindelijk zelf 'de (vele) knoppen van het machine' bedienen. Je bent me altijd blijven steunen en aanmoedigen in het verder verloop van mijn thesis. Peter, ik heb een enorme bewondering voor jouw wetenschappelijke kennis, kalmte en gedrevenheid. Jouw bereidheid tot helpen - ondanks een overvolle agenda – waardeer ik enorm. Sven, jij bent pas veel later in het verhaal gestapt, maar hebt toch in die korte tijd een bijdrage geleverd aan de voltooiing van dit werk.

Mijn co-promotoren verdienen ook een woordje van dank. Prof. Dr. Beuls en Prof. Dr. Lambrichts, jullie adviezen, ondersteuning, discussies en suggesties hebben mee dit werk verrijkt.

Mijn dank gaat ook uit naar de overige leden van de jury voor hun grondige lezing van mijn doctoraatsthesis en de kritisch opmerkingen en waardevolle suggesties die zij geformuleerd hebben.

Prof. Dr. Jan Gelan verdient een woord van dank omdat hij mee aan de wieg stond van deze multi-disciplinaire samenwerking tussen de NMR groep en de afdeling morfologie. Hij stelde de NMR infrastructuur ter beschikking om dit doctoraat te kunnen realiseren. Hij kwam ook steeds geboeid mee volgen bij de MRI experimenten, maar ook enthousiast kon vertellen over welke mogelijkheden er nog allemaal in de pijplijn zaten.

I would also like to express my gratitude to Dr. Felix Scholtes. I had the pleasure to collaborate with him on the spinal cord experiments. Thanks for sharing your expertise and providing helpful suggestions for improvement.

Prof. Dr. Niels Hellings wil ik bedanken om me mee te nemen in het stamcelproject. Ik wilde graag mijn MRI kennis gebruiken in 'iets toegepast' en daar is het stamcelhoofdstuk het finale resultaat van. Jij hebt me ook in contact gebracht met andere boeiende onderzoekers zoals Prof. Dr. Peter Ponsaerts, die op zijn beurt steeds bereid was om me kennis bij te brengen of om me praktisch op weg te helpen. Dank-jullie-wel allemaal voor jullie inzet.

Verder wil ik de collega's van morfologie even toespreken die me in dit traject langs labo's en koffiekamers vergezeld hebben. Marjan en Linda wil ik danken voor de kans die ze me gegeven hebben om mijn doctoraat in hun anatomie afdeling te doen. Jullie hebben me de vrijheid gegeven om zelfstandig het wetenschappelijk pad te bewandelen. Ivo jouw deur stond altijd open om histologische experimenten te bespreken en te evalueren. Romain, Dennis en Oswald het was fijn om met jullie 'de zaal' in orde te brengen voor de practica. Dankjewel Liliane voor het steeds piekfijn reinigen van mijn dissectiemateriaal en de lekkere koffie. Bedankt Marc, Jeanine en Marie-Josée voor de vele kleuringen die jullie gedaan hebben. Hugo, jou kon ik altijd contacteren als er iets vakkundig moest worden gemaakt. Ook wil ik je bedanken om steeds naar me te luisteren als ik er weer eens allemaal genoeg van had. Marc en Magda bedankt voor jullie grafische bijdrages voor posters, presentaties of anatomische tekeningen. Josette, Kathleen, Agnes en Jean, voor jullie ook een applausje voor jullie uitmuntend administratief werk. En vooral even extra dank aan Kathleen.

Jij hebt de laatste tijd allerlei klusjes voor de thesis gedaan in mijn opdracht. Kortom jullie waren er steeds om me op wetenschappelijk vlak te helpen!

En dan zijn er ook de doctorandi waarmee ik zoveel beleefd heb in het labo, op congres of op feestjes. Tom, we zijn gelijktijdig begonnen aan deze uitdaging en daarom wens ik je veel succes met jouw doctoraat. Wendy jij was een leuke bureau-gezel. Je had altijd tijd om me te helpen, voor een babbeltje of een wedstrijdje bejeweled. Nog even en jij mag ook beginnen pennen aan jouw boekje. Ook de nieuw doctorandi wil ik bedanken voor de leuke maar korte tijd. En als laatste is er nog Marjanneke. Ons motto was 'equal minds think alike'. Dit is zo vaak gebleken en dit zowel binnen als buiten de werkmuren. Je bent een fijne ambitieuze dame. Bedankt voor zooooveeeel.

Ik wil ook de mensen van scheikunde bedanken voor hun bijdrage. Ivo Feytens (grote hulp en adviseur bij het spoelen van probes), Greet Cuyvers en Prof. Carleer (zorgden voor een snelle ijzerbepaling van mijn samples), Jos Kaelen (nauwkeurige producent van MRI buizen), Koen Vanvinkenroye (meester in het begrijpen en oplossen van rare foutmeldingen/bugs van het MRI toestel) en Raoul Mens (grommelpot en grappenmaker in één) nogmaals bedankt om me dikwijls bij te staan met raad en daad.

De fysiologie meisjes wil ik ook bedanken voor de heerlijke pizzahut middagpauzes, de milène of tupperware avonden en de disneytrip. Ook dank aan de immunologiegroep, en in het bijzonder Christel, Igna, Kim, Bieke en Kurt voor jullie hulp bij de stamcelexperimenten. Hier wil ik toch Kurt even nog een woordje toespelen. We zijn samen gestart met de kneepjes van de MRI onder de knie te krijgen en zijn daar behoorlijk in geslaagd. Als de ene een stap niet meer wist dan kon de andere altijd bijspringen. Jij hebt je vaardigheden ondertussen al uitgebreid en waagt je ook al op het spectroscopiedomein. Ik wens je veel succes in je verdere carrière. Wilfried verdient ook een grote dankjewel voor de frequente hulp bij de proefdieren.

Lieve vriendinnen, fijn dat ik altijd bij jullie terecht kon. Jullie hadden altijd interesse, hoewel ik nogal eens kon mopperen als het weer eens tegen zat. Bedankt voor alle afleiding, gezelligheid en voor alle steuntjes in de rug.

Tot slot wil ik mijn familie en schoonfamilie danken voor hun continue steun en interesse doorheen mijn gehele doctoraatsproject. Lieve David, ik wil je bedanken voor het begrip dat je opbracht als ik weer maar eens in het weekend moest werken of wanneer ik 's avonds nog eens moest terugkeren naar het werk en jij me dan altijd moest vergezellen. Het is mij ook niet ontgaan dat je de afgelopen tijd net iets meer huishoudelijke taken op jou hebt genomen opdat ik mijn schrijfwerk kon uitvoeren. Maar vooral bedankt voor de steun op die momenten dat ik het net iets minder goed zag zitten. Het is niet altijd even simpel geweest om de partner van een doctorandus te zijn denk ik zo, en jij hebt die rol met glans vervuld.

Aan het einde van een periode in je leven, is het altijd nodig om even je tijd te nemen, nog even terug te blikken op kleine successen en grote mislukkingen, om vast te stellen dat het mooi geweest is, alvorens met een tevreden gevoel een nieuwe start te nemen.